ABSTRACT

Title of Document: SPRAY FLAME AND EXHAUST JET CHARACTERISTICS OF A PRESSURIZED SWIRL COMBUSTOR

Martin Brendan Linck, Doctor of Philosophy, 2006

Directed By: Professor Ashwani K. Gupta
Department of Mechanical Engineering

This work describes an investigation of swirl-stabilized flames, created in a combustor featuring co-annular swirling airflows, under unenclosed, enclosed, and submerged conditions. A centrally-located fuel nozzle, which uses air-assist atomization, creates a methanol fuel spray. This approach provides great control over fuel spray properties in a compact geometry. Factors affecting the structure of the flames, including the effect of the central atomization air jet, are investigated using three-dimensional particle image velocimetry, direct imaging, and phase-Doppler particle analysis techniques. Exhaust jet temperatures are measured. The dynamic events affecting two-phase exhaust jets from the combustor under submerged conditions are examined using high-speed cinematography and sound spectrum analysis.

It is found that the structures of the flames examined, which feature low overall equivalence ratios, are closely linked to the features of the air flowfield in the combustor. Swirl numbers of flows emerging from twisted-vane swirl assemblies are characterized. The structure of the flow is affected by the swirl configuration, but does not depend heavily on the Reynolds number. The central atomization air jet (with or without fuel) reshapes the recirculation region in the swirling flow and has a significant, controllable effect on the structure of the airflow and flame. The effect is the same for nonreacting and reacting flows. In one unique case, the central atomization air interacts with the swirling flow to create two recirculation regions and a lifted flame. The lifted flame is more compact than similar non-lifted flames. The twin-fluid atomization approach is shown to provide effective atomization over a wide range of operating conditions. The two-phase interaction of the exhaust jet is found to depend on the pressure drop over the exhaust nozzle. The dynamic behavior of the exhaust jet is buoyancy-driven at low pressure drops, and is affected by complex instability mechanisms at high pressure drops. Strouhal numbers of large-scale unstable events occurring in the two-phase flow are two orders of magnitude smaller than those associated with instabilities in single-phase flows. Evidence is presented, indicating that acoustic pressure waves in the exhaust jet may be involved in the generation of bubbles surrounding exhaust jets at high pressure drops.

SPRAY FLAME AND EXHAUST JET CHARACTERISTICS OF A PRESSURIZED SWIRL COMBUSTOR

By

Martin Brendan Linck

Dissertation submitted to the Faculty of the Graduate School of the
University of Maryland, College Park, in partial fulfillment
of the requirements for the degree of
Doctor of Philosophy
2006

Advisory Committee:
Professor Ashwani K. Gupta, Chair
Dr. Mark Lewis, Professor, Dean's Representative
Dr. Keith Herold, Professor
Dr. Bao Yang, Associate Professor
Dr. Michael Zachariah, Professor

Dedication

To my uncles, Thomas Linck and Jim Hewitt

Acknowledgments

The work presented below is the product of four years of effort, which have brought me into contact with a great many amazing people. My family and friends have, of course, played a vital role in encouraging me and keeping me motivated. I'd like to thank my father, Ernst Linck, for his example and inspiration, and my mother, Jeannette Auman, for the love she has always shown me, and the confidence she has always had in me. Phoebe Ezidinma has always reminded me what all the work is for. My advisor, Dr. Ashwani K. Gupta, has opened my eyes to entirely new vistas of possibility, and steadfastly supported my efforts in every conceivable way. My brother Michael Linck made sure I got out of the lab every once in a while. Michael Knospe taught me how to shape iron and tame fire, Bruce MacMillan taught me what determination really means, Bernard LaFrance taught me what precision is, and Howard Grossenbacher showed me that it is possible to do excellent work without losing your sense of humor. Bill Griffin and Bob Woodworth always had the part I needed, or knew where to get it. Dr. Ken Kiger gave me valuable insights on optical diagnostic techniques and on proper experimental procedures, Dr. Greg Jackson provided me with insight into fundamental physical principles, and Dr. Michael Zachariah taught me how to develop real engineering judgment.

Special thanks go to Monsieur Guillaume Bourhis, who carried out my instructions carefully, precisely and with great good humor, and who wrote the bulk of the text in Appendix A of this work. Thanks also to Vivek Gautam, Michael Armani, Magnus Mörtberg, Sean Archer, Ahmed Abdelhafez and to my other compatriots in the Combustion Lab.

Finally, I wish to express my sincere gratitude to the Office of Naval Research (ONR) and special thanks to Dr. Gabriel Roy, Program Manager at ONR for financial support of the project as well as support provided for many of the advanced optical diagnostics used here.

Table of Contents

Nomenclature

S	Swirl number
G_θ	Tangential momentum
G_Z	Axial momentum
L	Characteristic length
R_i	Inner radius of swirler annulus
R_o	Outer radius of swirler annulus
ρ	Density
V	Mean axial velocity
W	Mean rotational (tangential) velocity
v'	Instantaneously varying component of axial velocity
w'	Instantaneously varying component of tang. velocity
r	Radius
p	Pressure
p_∞	Pressure of the ambient
D	Diameter of the inlet to the combustor
m	Mass flowrate
p_o	Pressure upstream of an orifice
A	Area of an orifice
T_o	Temperature upstream of an orifice
γ	Ratio of specific heats of a compressible fluid
R	Specific gas constant of a compressible fluid
$twist$	Twist of a swirler vane
θ_r	Rotation in degrees
t_Z	Axial translation in units of length
θ_B	Swirler vane angle
θ_o	Swirler outer vane angle
R_c	Central radius of swirl assembly
h	Height of swirl assembly
St	Strouhal number
f	Frequency
η_τ	Temporal Kolmogorov scale
ν	Viscosity
V_{max}	Maximum mean velocity in flow
η_X	Spatial Kolmogorov scale
τ_d	Droplet characteristic time
d_d	Droplet diameter
δ	Swirl annulus gap
Re	Reynolds number
δ_i	Annulus gap of inner swirler
δ_o	Annulus gap of outer swirler
θ_{jet}	Angle between turbulent jet and laser plane
Re_{o1}	Outer Annulus Reynolds number, Re Condition 1

Re_{o2}	Outer Annulus Reynolds number, Re Condition 2
Re_{i1}	Inner Annulus Reynolds number, Re Condition 1
Re_{i2}	Inner Annulus Reynolds number, Re Condition 2
Vmean	Local mean axial velocity
Wmean	Local mean tangential velocity
Umean	Local mean radial velocity
X	Radial location
Y	Axial location
D10	Droplet mean arithmetic diameter
D32	Droplet Sauter mean diameter
N_i	Number of droplets of a particular size
D_i	Diameter of droplets of a particular size
N	Total number of droplets in a sample
rate	Rate of a chemical reaction
k	Temperature-dependent reaction constant
$[A]$	Concentration of reactant A
$[B]$	Concentration of reactant B
D_E	Diameter of exhaust jet
P_C	Total pressure of combustor
3D PIV	Three-dimensional Particle Image Velocimetry
PDPA	Phase-Doppler particle analysis
PLIF	Planar laser-induced fluorescence
FMN	Flush-mounted nozzle
CPN	Conical projecting nozzle
CCDN	Corrugated converging-diverging nozzle
FFT	Fast Fourier transform
PMT	Photomultiplier tube
RSA	Real-time signal analyzer
KHI	Kelvin-Helmholtz instability
RMI	Richtmyer-Meshkov instability

1. Motivation

Future propulsion challenges associated with Navy vessels will increasingly deal with underwater propulsion. Underwater combustor systems, associated with torpedoes, missiles, or other types of submersible systems are an area of particular interest. Furthermore, there is a need for small, autonomous underwater vehicles (AUV's). As has been demonstrated by the airborne Predator program, autonomous vehicles, capable of monitoring or intervening in critical situations, are quite effective. A similar type of vehicle, designed for naval applications, could help monitor coastlines, eavesdrop on radio and other communications, and remain concealed in shallow waters. Vehicles of this kind might also be used to actively pursue and eliminate threats. Progress in this area has been limited, however, as development of propulsion systems for small submersible craft is quite challenging. Currently, the state of the art propulsion system for this type of craft is represented by battery-powered electric motors. Combustion-based propulsion systems offer much higher power densities, and can potentially be lighter. However, a detailed understanding of the combustor and exhaust jet behavior is crucial in designing a practical vehicle.

The work presented below examines issues of direct relevance to this area of propulsion. Combustors designed for future AUV applications, or for larger-scale underwater propulsion applications, must operate efficiently at small scales and over a range of pressures. At low to moderate combustor power settings, or at great depths, the pressure in the combustor may be only slightly higher than the pressure of the surroundings. The water does not directly interact with the flame in the combustor under these conditions, but parameters involved in control of the flame structure and combustion characteristics must be clearly understood if effective combustors are to be designed in an efficient way. The fundamental effect of pressure on flame structure is also important. More complex effects, such as changes in the exhaust jet behavior due to heat release in the combustor and the potential for linked interaction between the exhaust jet characteristics and dynamic combustor behavior, are also of interest. A test combustor has been constructed, and a series of studies has been carried out to address each of these issues.

2. Introduction

The present work describes a detailed investigation of swirl-stabilized, liquid-fuelled spray flames. Particular attention is paid to the effect of airflow parameters on the flow field and on the structure of the flame. In a practical, liquid-fuelled submerged combustor, air is not likely to be used as an oxidizer, but some form of gaseous oxidizer may be used. In the present study, the oxidizer used was air, for reasons of experimental simplicity. However, fundamental observations on flame characteristics will likely apply to swirl-stabilized flames using any combination of liquid fuel and gaseous oxidizer.

Swirl in the burner was generated by swirler vane assemblies. The features of the swirling air flowfield associated with each swirler were examined via a cutting-edge three-dimensional particle image velocimetry (PIV) technique. An efficient and flexible twin-fluid fuel atomization scheme was employed, and the effect of a central atomization air jet, emanating from the fuel nozzle, on the features of the flowfield in the combustor was examined in detail. The effects of operating parameters on the features of the fuel spray were examined. Scaling issues associated with swirl-stabilized flames were addressed. Several nonreacting submerged experiments were carried out, and features of the two-phase exhaust regime are presented for two combustor pressure conditions in which the exhaust jet was unchoked and choked. A pressurized, submerged flame, obtained under conditions where choking occurred in the exhaust nozzle, is also described.

3. Background

Swirl-stabilized flames have been found to possess extremely useful characteristics, such as large turndown ratios, rapid fuel vaporization, and efficient mixing, thus allowing the design of compact and stable combustion systems. The investigation described below deals with the behavior of a swirl-stabilized, methanol-fuelled combustor, which features a swirl-stabilization arrangement found in many compact, high-energy-density combustors, such as those in gas turbine engines. Specifically, the combustor has been examined under conditions relevant to underwater propulsion applications.

Essential observations on the nature and characteristics of swirling flows have been presented by Gupta, et al. (1984). In a swirling flow, the rotation of the fluid plays a significant role in determining the structure and behavior of the flow. As can be seen in Figure 1, the contours of axial, radial, and tangential (rotational) velocity display particular features in a flow of this type (Chigier and Beér, 1964). The centrifugal force created by the rotation of the fluid forces the flow toward the outer walls of the duct.

Distinct peaks in axial and rotational mean velocities occur near the wall, and the relative magnitudes of these peaks depend on the relative magnitude of the rotation of the flow.

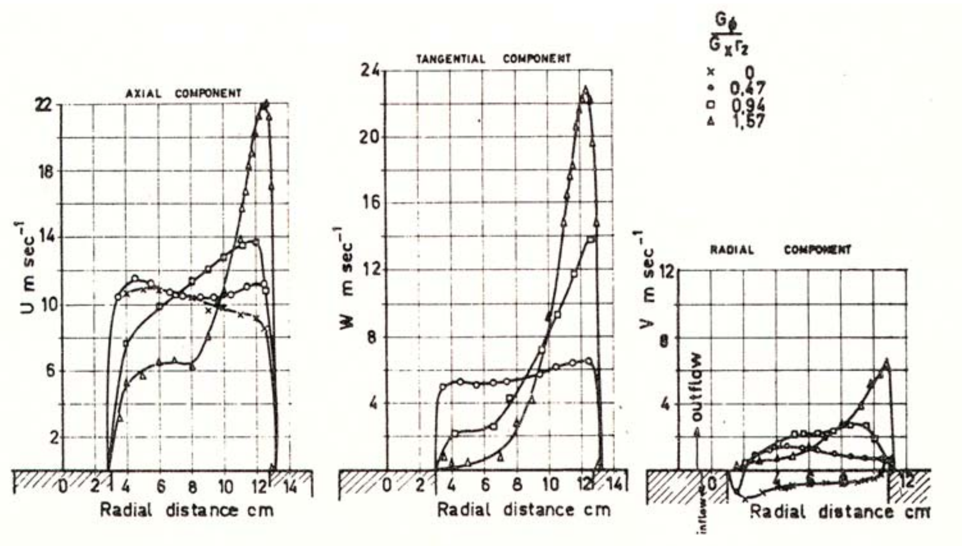

Figure 1. Axial, tangential and radial mean velocity curves, (from Chigier and Beér (1964))

The degree of rotation of a flow can be characterized by the swirl number, *S*, which is essentially a non-dimensionalized ratio between the mean axial momentum and mean rotational momentum of the flow.

$$S = \frac{G_\theta}{G_z * L} \tag{1}$$

Here, G_θ is the rotational momentum, G_Z is the axial momentum, and *L* is a characteristic length associated with the flow (usually the duct diameter). In a situation where the flow is annular, the inner and outer radii of the annulus are referred to as R_i and R_o, respectively. An approach by which the swirl number of a flow can be obtained is presented below (Gupta, et al., 1984).

$$S = \frac{G_\theta}{G_z * R_O} \tag{2}$$

$$G_\theta = \int_{Ri}^{Ro} (\rho * V * W + \rho * \overline{v' * w'}) * r^2 dr \qquad (3)$$

$$G_Z = \int_{Ri}^{Ro} (\rho * V^2 + \overline{\rho * v'^2} + (p - p_\infty)) dr \qquad (4)$$

In this approach, V and W represent the axial and radial components of the mean velocity, respectively. The fluctuating components of velocity in the axial and radial direction are represented by v' and w'. The local density is denoted by ρ, the local pressure is represented by p, and pressure of the ambient, surrounding the flow, is denoted by p_∞. The variable r indicates radial location. However, this expression contains several terms in (3) and (4) that can not generally be obtained experimentally. The local density is not usually available, and is generally assumed to be a constant. The pressure is assumed to be a constant as well. The turbulent shear stress term, which depends on the correlation between v' and w' in (3), is also difficult to measure experimentally. Thus, the pressure-dependent term and the term involving the shear stress must usually be omitted in the calculation of the swirl number, and an approximate swirl number can be obtained on the basis of mean axial and radial velocities as a function of radial location, as shown in (5), below.

$$S = \frac{\int_{Ri}^{Ro} V * W * r^2 dr}{Ro * \int_{Ri}^{Ro} V^2 * r dr} \qquad (5)$$

In theory, the swirl number of a flow is a conserved quantity, and should be invariant with axial location in the jet. In practice, however, the approximate swirl numbers calculated on the basis of available data are not generally conserved, and will vary somewhat, depending on the location in the jet at which they are obtained. Flows are generally compared in the literature on the basis of swirl numbers calculated at the exit plane of the duct from which the rotating flow emerges. The swirl numbers reported in the results presented below will be calculated using the traditional swirl number equation, in order to maintain consistency between the results reported here and those reported previously by other investigators.

Flows with high swirl numbers are found to display characteristics that have proven to be very useful in the field of combustion. If the swirl number of a simple flow, emerging from a round duct, is greater than 0.6, the flow displays vortex breakdown (see Figure (2), (from Lefebvre, 1983). In this situation, the pressure at the center of the flow is reduced dramatically by the rotation. Fluid from the downstream region, which has a lower velocity and therefore a higher pressure, is forced back upstream, forming a recirculation region in the flow. In a combustor, this feature is quite useful, since recirculation of hot product gases helps to ignite cool incoming material, and this makes it possible to stabilize combustion in the combustor at much higher fuel and air flowrates than would otherwise be possible. In cases where there is a central obstruction in the flow, such as a

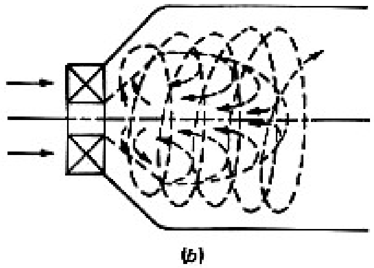

Figure 2. Schematic of flow in a gas turbine combustor (from Lefebvre (1983))

fuel nozzle or bluff-body flame stabilizer, some recirculation downstream of the obstruction would occur, even if the swirl number were zero. When rotation is imparted to the flow, this recirculation region downstream of the obstruction increases in size, and combustion is effectively stabilized. An example of this type of flow is shown in Figure 3, (from Chigier and Beer, 1964). The figure shows axial velocity contours in a recirculating flow downstream of an obstruction. The recirculation region in this case has a distinct tulip shape, and flames stabilized through this approach usually have the same shape.

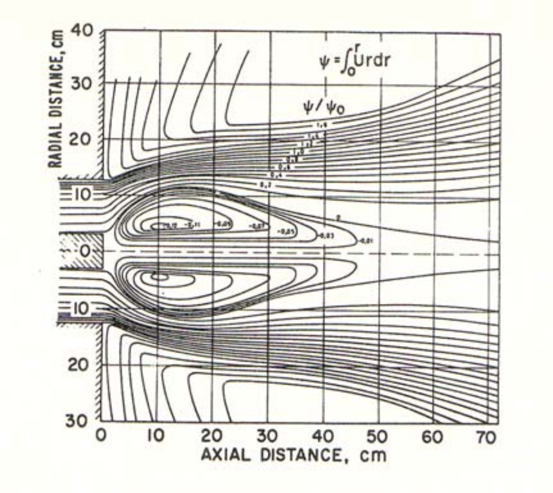

Figure 3. Contours of axial velocity in a recirculating flow with a central obstruction (from Chigier and Beér (1964))

The recirculating flow in the combustor is also quite turbulent, and this provides a useful degree of mixing. In non-premixed combustors, where the fuel and oxidizer are injected separately, rapid and complete mixing are desirable in order for high combustion efficiency to be achieved. A very effective strategy in combustion has been to inject gaseous or liquid fuel directly into the recirculation zone. If the fuel is injected as a liquid, the fuel droplets evaporate rapidly in the hot recirculating gas. This approach is often employed in gas turbine applications (Cohen, et al., 1996). However, since the recirculated material consists largely of product gases, the concentration of unreacted oxidizer in the recirculation region is low. Ignition of the fuel does not occur until the heated, vaporized fuel is brought into contact with unburned oxidizer at the boundary of the recirculation region. Turbulent distortions of the flow then mix the combusting material in order to promote rapid and complete combustion.

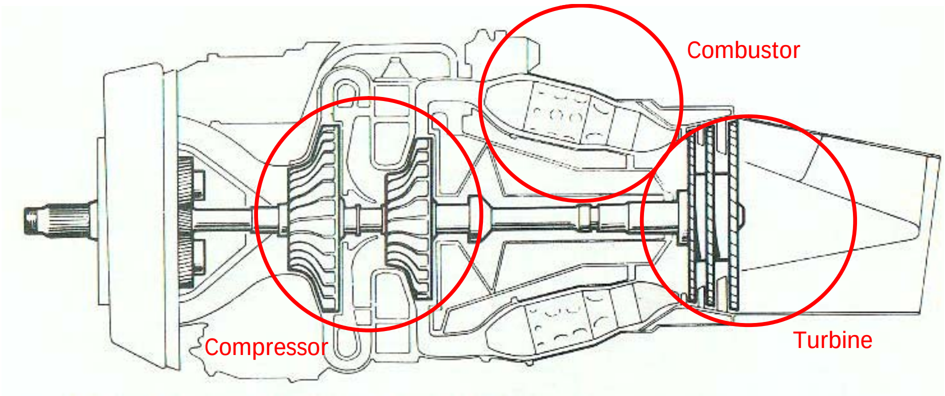

Figure 4. Components of a Rolls-Royce gas turbine engine (from Cohen, et al. (1996))

Due to their utility, swirl-stabilized combustors have been widely employed in industrial and propulsion applications. For example, Figure 4, (from Cohen et al., 1996) shows a schematic diagram of an aircraft gas turbine engine, with the relative locations of the compressor, combustor, and turbine sections. Air from the compressor is fed into a set of swirl-stabilized combustors, spaced evenly around the central shaft of the engine. Fuel injection, atomization, combustion and mixing must occur as efficiently as possible in a very compact geometry. Careful control of the outlet temperature from the combustor is also important, since the blades of the turbine cannot generally tolerate the flame temperature of the combustor. The combustor walls must also be cooled. For this reason, excess air is generally fed into the combustor, and controlled mixing of the excess air with the products of combustion ensures that each engine component remains at an acceptable temperature. It is important to note that the overall efficiency of the engine increases with combustor outlet temperature, so a careful balance must be struck between the maximum temperature that can be tolerated by the engine components and the thermal efficiency of the system. Swirl-stabilized combustors have been found to perform these functions quite well, creating conditions where every aspect of the combustion process can be effectively controlled.

Despite their widespread practical application, however, swirl-stabilized combustors are not clearly understood. Generally, practical combustors are developed on a cut-and-try basis (Lefebvre, 1983, Cohen et al., 1996). The conditions within the combustor are so extreme that they can be replicated in an experimental setting only at great expense and with great difficulty. The pressures involved in practical combustors are particularly problematic; in a gas turbine, a combustor may operate at up to 60 atmospheres (bar) of total pressure. In experimental investigations, swirl-stabilized systems have generally been examined only under atmospheric conditions. Analytical understanding and prediction of combustor behavior are currently impossible, due to the complexity of the flow and the number of factors influencing the performance of the combustor. Even numerical modeling of the flow is generally quite difficult. Particularly in liquid-fuelled non-premixed systems the presence of two phases, the processes of fuel evaporation and mixing, and the turbulent characteristics of the system pose great challenges in the development of models. Models using the Reynolds-Averaged Navier Stokes (RANS) approach are particularly problematic, since they generally assume the turbulence in a flow is isotropic in order to obtain closure of the turbulence model. In fact, the turbulence in swirling flows is quite anisotropic, and the features of the flowfield are further affected by the processes of combustion, in ways that are very difficult to incorporate into a model (Bernard and Wallace, 2002). Simplified RANS models, that capture relevant features of the flow behavior even in dynamic, time-variant flows can be created (Sengupta and Mashayek, 2005). However, these models generally need to be tuned to a particular experimental case, and are not likely to produce good results in other cases.

Advanced large eddy simulation (LES) models have been shown to give better results than RANS models, but only at the expense of vastly increased computational complexity. Menon et al. (2004) have shown that experimental observations of practical combustors can be used to validate LES-based numerical models, but development and execution of the model is so time-consuming that the models do not, at this point, present an effective method for design of practical systems.

Experimental efforts have been made in order to better understand the behavior of practical, liquid-fuelled, non-premixed combustors. Davis and Samuelsen (1996) present observations on swirl-stabilized combustion in an atmospheric-pressure combustor, designed to incorporate components found in practical systems. The objective of their work was to optimize the performance of the combustor across a range of power settings and flowrates, providing stable and complete combustion under various conditions.

Li and Acharya (2001) present work carried out using an optically-accessible swirl-stabilized combustor. The combustor was actively controlled in order to reduce the effect of combustion instability in the system, and the features of the flame front could be examined. Unstable combustion is a problem in certain combustion systems, particularly under lean premixed conditions, and develops when the Rayleigh criterion is met (Rayleigh, 1945). The Rayleigh criterion predicts that unstable combustion, characterized by oscillatory fluctuations in combustor pressure and heat release, will be driven when some heat release mechanism is synchronized with an acoustic mode of the system. If the heat release signature of the system is in phase with the acoustic mode, then maximum heat release occurs when the pressure in the system is at its maximum, and the instability will be amplified until the system breaks down or factors limiting further growth of the instability are encountered. Sivasegaram and Whitelaw (1987) report that, in a bluff-body-stabilized premixed combustor, the amplitude of the pressure signal associated with unstable combustion reached 160 dB under certain conditions. Unstable combustion conditions, and resulting fluctuations in combustor pressure, are generally linked to the development of turbulent structures in the flow, whose mixing action influences the rate of heat release in the system (Gaydon and Wolfhard, 1979). If the cyclical development of these large, vortical structures is influenced by the unsteady pressure in the combustor, these events occur in phase with the unsteady pressure signal, and the Rayleigh criterion is met.

Unstable combustion can be controlled through two general approaches. In one approach, referred to as active control, the instability in the combustor is modulated by a control signal, which alters the conditions in the combustor on the same timescale as the instability. For example, the burner investigated by Li and Acharya (2001) featured several fuel streams, introduced through several nozzles. Some of the fuel was introduced as a modulated stream, whose flowrate could be actively controlled in response to an unstable combustion condition in the system. A variety of control algorithms were applied, and were shown to control the instability with varying degrees of success. In practical systems, however, an active-control strategy is generally not desirable, since the control hardware may be difficult and expensive to install.

The other approach to control of unstable combustion is passive control, and implies careful combustor design, which eliminates the development of large-scale turbulent structures. One such approach, involving passive control of unstable combustion in a swirl-stabilized, liquid-fuelled burner featuring two co-annular swirling air inlets, is described by Conrad, et al. (2003). Conrad, et al., found that the amplitude and frequency of the instability can be controlled through changes in the swirl and airflow distribution in the combustor. Studies of this type have contributed to an improved understanding of swirl-stabilized, liquid-fueled systems, but, as mentioned above, no comprehensive theory of swirl-stabilized combustion has emerged. A great variety of combustor geometries and fuel atomization schemes occurs in the literature, and each system appears to have its own unique features. Different combustors must be examined and characterized individually, and models developed on the basis of data gathered from a particular system are not likely to have general applicability to other systems.

The situation is complicated further by the variety of fuel atomization strategies employed in the development and operation of liquid-fuelled combustors. The most common approaches involve pressure-swirl atomization, in which a fuel spray is forced at high pressure though a nozzle, in which some rotation is imparted to the fuel stream. The fuel emerges as an unstable rotating sheet of liquid, which rapidly undergoes ligamentation. During ligamentation, the liquid fuel sheet breaks down into long string-like structures, which quickly break apart into small spheres (Nasr, et al., 2002). It is possible to create fine sprays through this approach, but the mean diameters associated with the fuel spray depend on the pressure drop across the nozzle, and are thus linked to the fuel flowrate. It is not generally possible to obtain equally effective atomization across all fuel flowrates with this approach. Another strategy involves the use of airblast atomization (Davis and Samuelsen, 1996). In this approach, at least two co-annular air ducts are used to feed air into the burner. Swirl may be imparted to one or both of the air streams, and the fuel spray is injected into the inner air stream through a pressure swirl atomizer, in such a way that small droplets are entrained, but larger droplets impact the outer wall of the inner air duct. The droplets form a liquid sheet along the wall, and the sheet moves downstream, to the lip of the inner air annulus. At the lip, the inner and outer airflows interact, and the liquid sheet is destabilized, forming ligaments entrained in the airflow. The ligaments are then destabilized further, and atomization of the fuel droplets is achieved. This approach allows the fuel flowrate to be adjusted over a wide range, since the most important atomization processes occur where the inner and outer combustion air streams meet. The atomization can be affected by changes in the swirl characteristics and flowrates of the inner and outer combustion air streams.

A further refinement of this approach is represented by twin-fluid atomizing nozzles. Airblast atomization provides greater flexibility than pressure-swirl atomization, but the effectiveness of the atomization is still linked to the flowrates of combustion air fed to the burner. Effective atomization across all desired operating conditions cannot be guaranteed, particularly if the air flowrates are too low to destabilize the fuel sheet at the lip of the inner air duct. In a twin-fluid atomizing nozzle, the fuel stream is brought into contact with a rotating stream of atomizing air, whose flowrate can be adjusted independently (Nasr, et al., 2002, Delavan, 1998). The atomization air flowrate will generally represent less than 1% of the total air fed to the burner, but is the only important parameter in determining the atomization characteristics of the nozzle. (Delavan, 1998). The dimensions of twin-fluid atomizing nozzles are similar to those of pressure-swirl nozzles, and can be quite compact. Nozzles of this type are commercially available, and are rated to produce liquid sprays with droplet mean diameters on the order of 30 to 50 microns. This approach allows effective atomization of the fuel across a wide range of operating conditions, and in a very compact geometry. Since this investigation deals with propulsion challenges relevant to underwater propulsion, and twin-fluid atomization has characteristics that are desirable in a future underwater propulsion system, this type of atomization is be investigated experimentally in the present work.

However, it must be noted that twin-fluid atomization requires that an atomizing air jet be present. The effect of this type of jet, interacting with a recirculating flow, has not previously been investigated or described. This investigation therefore provides fundamental insight into characteristics of a swirling, recirculating flow where a centrally located air jet affects the structure of the airflow and flame in the combustor.

The method by which swirl is introduced into a flow is also important. Two general strategies have been described. Tangential-entry systems generate swirling flows via the interaction of axial and tangential flows, which mix in an upstream mixing duct. These flows have been examined experimentally, and can be characterized relatively easily (Gupta, et al. 1984). Contours of mean velocity are smooth and radially-symmetric in flows of this type, which allows swirl numbers to be calculated on the basis of relatively small amounts of experimental data. This feature was quite important in early investigations, where flow velocities had to be measured in time-consuming experiments using hotwire probes. Unfortunately, tangential-entry systems are impractical, since they generally require more space than is available in practical applications.

Production combustion systems usually employ swirler assemblies, which consist of solid angled vanes, placed in the flow. The flow emerging from a swirler is more complex than that from a tangential-entry system, but this approach allows rotation to be imparted to the flow in a much more compact geometry than is possible with tangential-entry systems. The open spaces between the vanes behave as separate ducts, and the flow emerging from each space interacts and mixes with the adjacent flows. Flows of this kind have been quite difficult to examine experimentally. However, new optical measurement techniques, particularly three-dimensional particle image velocimetry (3-D PIV), make it possible to examine complex rotational flows in an experimental context (Alkislar, et al., 2003).

The investigation of combustors that are optically accessible is increasingly important. Optical techniques such as phase-Doppler particle analysis, or PDPA (Bachalo and Hauser, 1984) and particle image velocimetry (Raffel, et al., 1998) make it possible to examine the phase behavior of complex, two-phase reacting systems. Optical access also allows flame imaging, which makes it possible to examine the flame structure and regions of heat release in the flame. These techniques will be discussed in greater detail in the chapter on diagnostics below. Optical access to the combustor is necessary, however, for the advanced optical techniques to be applied, and for understanding of these very complex combustion systems to be advanced.

Optical access in a pressurized system is particularly problematic. Optical access is obtained through the use of windows made of quartz glass (also called silica glass) (Widmann and Presser, 2002). Quartz glass can tolerate high temperature gradients, and is strong enough to support considerable pressures. However, the thermal and mechanical stresses encountered in a pressurized combustor present great challenges. Despite the obstacles, some work in systems of this type has been carried out. Locke, et al. (2001), describe results obtained through the use of optical diagnostics in an experimental combustor operating under conditions commonly encountered in gas turbine engines. They applied elastic laser sheet scattering, Rayleigh scattering and planar laser-induced fluorescence (PLIF) imaging techniques in order to examine a combustor operating at 3400 °F, at a pressure of 900 psi. The construction and operation of a system of this type is extremely expensive, but certain effects, such as the complex interaction between pressure, local combustion reaction rates, and the structure of the flow, cannot be studied without a pressurizeable system. For the type of application of interest in this study, it is not necessary for extremely high pressures to be examined directly. Since submerged combustors are likely to operate at a variety of pressures, and since the effects of submersion are very poorly understood, moderate combustor pressures will be examined. In submerged combustor studies, moderate pressurization experiments are also most interesting, since the effects of combustor submersion on the flame are likely to be most pronounced under conditions where the combustor pressure is only slightly higher than the ambient pressure. In a situation where the combustor is at a much higher pressure than the surrounding fluid, the combustor behavior will likely be effectively decoupled from the conditions in the surroundings.

Some work on liquid-fuelled, swirl-stabilized flames, featuring co-annular swirl inlets and a twin-fluid atomization arrangement, has been carried out. Linck and Gupta (2002) present an investigation of the effect of combustion and swirl configuration on the geometry of unconfined kerosene spray flames. The work describes the first application of 3-D PIV within highly luminous kerosene spray flames. Gao, et al. (2002) present a RANS-based model of kerosene droplet evaporation in a nonreacting, swirling air flow.

The model was validated using data presented by Linck and Gupta (2002).

Linck, et al. (2003) describe the effect of swirl configuration and airflow parameters on the exhaust gas composition of swirl-stabilized spray flames. Gupta and Linck (2003) explore the use of swirl configuration as a technique for passive control of combustion instability. This technique is explored in further detail by Linck, et al. (January, 2004), who show that swirl configuration and airflow parameters are shown to control a forced instability in a swirl-stabilized combustor. Droplet motion within the flame and exhaust gas characteristics associated with the flame in a forced, unstable situation is considered in further detail by Linck, et al. (March, 2004).

A study on the effect of fuel type on flame structure, in enclosed and unenclosed flames, is presented by Linck, et al., (August, 2004). Methanol and Kerosene flames are considered, and the flame structure is found to depend primarily on the airflow parameters and thermal load of the flame. Both Kerosene and Methanol flames are found to have very similar geometries when fired at the same thermal load, with the same airflow parameters.

Observations on the use of the 3-D PIV technique in luminous, swirl-stabilized spray flames, are presented by Gupta, et al. (2004).

Linck and Gupta (2005) describe experimental studies of the exhaust jet produced by a pressurized, swirl-stabilized combustor. A PIV technique is employed to examine the structure of a supersonic exhaust jet, featuring fluid velocities on the order of 400 m/s. The exhaust jet in this study is vented into quiescent ambient air.

Linck et al. (2006) examine the dynamics of a submerged exhaust jet, issuing from a flame in a pressurized combustor into a water-filled mixing chamber.

Experimental procedures and observations on the fundamental characteristics of the jet are described.

The use of swirl configuration and airflow parameters as a means of passive control in swirl-stabilized spray flames is again considered, in greater depth, by Linck and Gupta (2006). The effectiveness of the technique in modulating the unstable behavior of a forced flame is clearly demonstrated.

The use of airflow parameters to control the general structure of spray flames, so that the length, width, and shape of the reaction zone can be specified, is considered by Gupta, et al. (2006). The effect of shear regions in swirling flows on fuel droplet behavior is also described.

The investigation described in the present work contributes significantly to the development and understanding of compact, swirl-stabilized combustion systems, for application in submerged environments. The combustor had many features that are directly relevant to the development of a practical system. Air fed to the combustor entered through two co-annular ducts, which allowed the structure of the airflow to be controlled through changes in the relative air flowrates fed through the inner and outer annulus. Liquid fuel was introduced into the combustor through an air-assisted, twin-fluid atomizing nozzle. Swirl associated with the inner and outer airflows could be controlled independently via the installation of different swirler assemblies in the inner and outer ducts. The system was optically accessible, and could be pressurized to several atmospheres of total pressure. The air flowfield and fuel spray associated with experimental flames was examined using advanced optical techniques. Finally, the effect of combustor submersion was examined directly, as the exhaust jet was vented into a downstream chamber filled with water. The dynamic behavior and structure of the two-phase exhaust jet interaction were examined and described, and novel observations on the nature of the instabilities associated with the exhaust jet are presented.

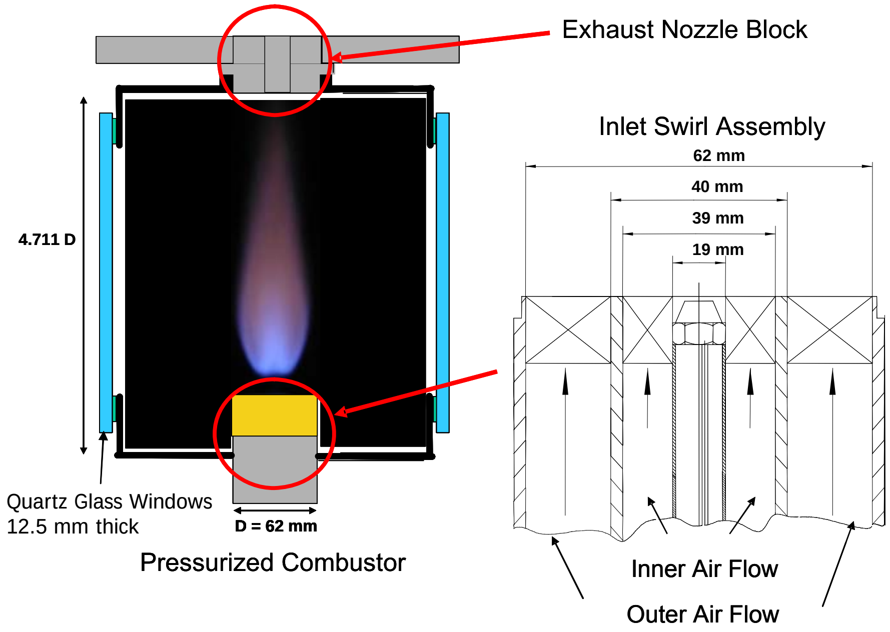

Figure 5. Pressurizeable, Optically-accessible combustor

4. Experimental Setup

4.1 Optically-Accessible Pressurizeable Combustor

4.1.1 Combustor Description

The combustor used to carry out the present investigations is shown schematically in Figure 5. An injector assembly, containing inner and outer air annuli and a centrally-positioned twin fluid atomizing nozzle, were used to feed fuel and air into the system. The outer diameter, D, of the larger air annulus in the injector was 62 mm. Swirlers were installed at the exits of the air annuli, through which the combustion air was fed. Atomization air and fuel streams were injected into the combustor through the atomizing nozzle. The rectangular enclosure fitted over the injector featured a square horizontal cross-section, and was constructed of 2.5 mm-thick sections of type 304 stainless steel. The sections were welded together to form the frame of the enclosure. Four large apertures, one on each vertical side, provided optical and physical access to the interior of the enclosure. Windows could be bolted over the apertures where optical access was desired, or steel plates could be used to cover apertures where no optical access was necessary. Dimensions were as given in the figure; the tolerances were held to approximately 250 μm. The external faces of the apertures were milled flat to within 25 microns, so that quartz windows could be installed and pressed tightly against the frame without shattering. The quartz windows that were used in the present investigation were 12.5 mm thick, and had a nominal total burst pressure of approximately 10 bars. The system was successfully tested, in a nonreacting situation, up to a total pressure of 2.7 bars. Higher pressures than this were not employed in order to maintain an appropriate safety factor.

Steel-reinforced graphite gaskets, rated to temperatures of 2000 °F and pressures of approximately 50 bar, were used to seal the gaps between the windows and the frame of the combustor. Each plate or window was held in place by an outer frame, and secured with 12 bolts. The bolts had to be tightened with great care, and in a star pattern. No single bolt could ever be under significantly more torque than its neighbors, and the maximum torque on the bolts could not exceed 7 inch-pounds when a window was being installed. If all windows and plates were properly installed, the enclosure was airtight. For the investigation described here, three windows and one special metal plate were installed. The plate was fitted with ports for igniter and pressure measurement hardware, and will be described in greater detail below.

The exhaust flow from the combustor exited through an aluminum nozzle block at the top of the combustion enclosure. The nozzle block held a specially-contoured nozzle, made of type 304 stainless steel, which determined the geometry of the exhaust jet. Several nozzle geometries were examined; these will be described in greater detail below.

In situations where a mixing chamber, containing water, was installed downstream of the exhaust nozzle, an aluminum baseplate was bolted onto the downstream face of the nozzle block. This baseplate formed the support for the mixing chamber. The mixing chamber will also be described in greater detail below.

4.2 Positioning System

In order to ensure that optical diagnostics could be applied in studies of the combustor, the entire system had to move in three dimensions, relative to the optical diagnostics. Despite the size and weight of the combustor (which was over two meters tall when the mixing chamber was attached, and weighed in excess of 100 kg), it was found to be much easier to position the combustor relative to the diagnostic equipment, than to move the diagnostic equipment relative to the combustor. Thus, the entire combustor system was built on a three-dimensional positioning stage. The stage consisted of a heavy aluminum plate, 2.5 cm thick, that could be raised or lowered by means of four screw jacks, positioned at the corners. The screw jacks were operated by a linked transmission, so that all four jacks turned at the same time and at the same speed. The transmission was controlled by a high-precision stepper motor, and the Y-position (vertical height) of the combustor could thus be controlled with great precision, on the order of one micron. The total travel in the vertical direction was approximately 60 cm.

This arrangement is shown schematically in Figure 6. Only the injector section of the burner is shown in the diagram; the enclosure and mixing chamber are omitted.

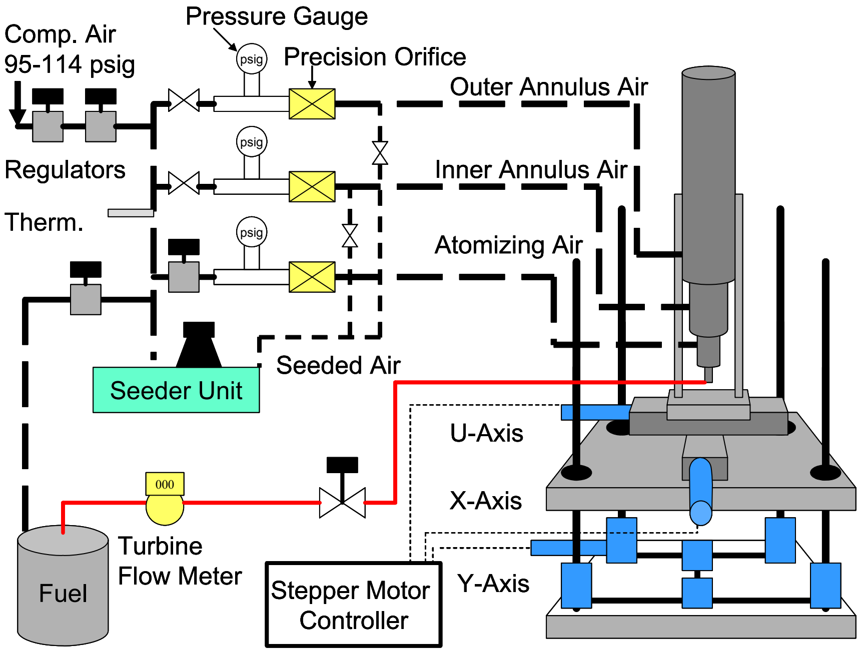

Figure 6. Schematic of Experimental Equipment

Translation in two horizontal directions, referred to as the X and Z axes, was accomplished by building the combustor on a smaller platform on top of two linear positioning tracks, also controlled by stepper motors. These motors were geared differently than the one controlling the Y-position of the burner, and were used to position the system with a precision on the order of 2.5 microns.

The axes of motion of the burner were aligned with the axes of the optical diagnostic systems used in the experiments. The diagnostic systems will be described in detail below. The precision of the alignment was such that the burner could be translated 30 cm along the path of one of the lasers, with a lateral displacement away from the laser path of less than 100 microns.

All three stepper motors were actuated by a single controller unit. The unit used (Aerotech Unidex 11) was programmable. A series of motions could be programmed into the memory of the machine, and executed in response to a user command.

4.3 Igniter System

Ignition of the combustor under enclosed and pressurized conditions was accomplished via an electrical ignition system. The system is shown schematically in Figure 7. Two leads, one grounded to the combustor frame and the other insulated, were connected to an external coil, powered by a 9 V battery (150 kV self-defense stun gun; Street Wise Security Products SW-150). The leads were inserted through the specially modified metal plate mentioned earlier; the same plate was fitted with pressure taps so that the combustor pressure could be monitored. The leads were held in slip fittings that could be loosened to push the leads in or out of the combustor, or tightened to fix them in one position. Prior to ignition, both leads were pushed into the combustor, until the tips of both leads were near the centerline of the combustor. An arming pin was inserted into the coil unit, and the arc was produced inside the combustor. Fuel and air flowrates were then increased until a stable flame was achieved. The arming pin was then withdrawn from the coil unit, which halted the arcing. The slip fittings were loosened and the leads withdrawn to the combustor wall. The slip fittings were then re-tightened, to hold the leads in place during combustor operation.

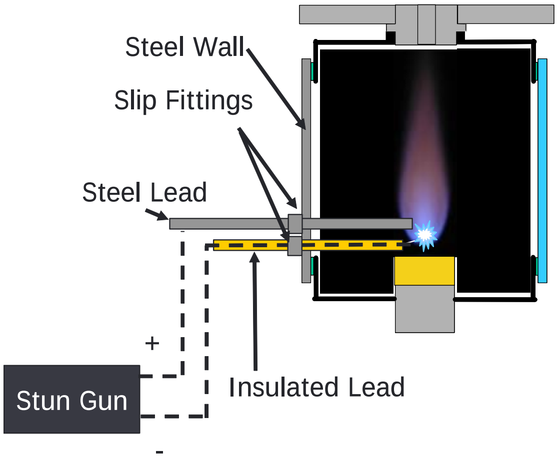

Figure 7. The ignition system

4.4 Air Handling System

Compressed air from a 75 kW Ingersoll-Rand screwdrive compressor was routed into the laboratory through copper pipe rated for pressures up to 8.5 bar. The compressor was positioned in an exterior bay, and was controlled in order to provide a system pressure of between 95 and 110 psig. The compressor was run unloaded until the system pressure dropped below 95 psig, at which point the compressor supplied a short burst of high-pressure air. Once the system pressure exceeded 110 psig, the combustor returned to unloaded operation. This effect produced a cyclical variation in the supply pressure, and the air had to be regulated in two stages in order to control variation in the air flowrates to within less than 1% of their total value. The air handling system used to supply air to the burner is also shown in Figure 6. Air from the compressor was passed through two regulators, and was fed, at 85 psig, to a set of choked-orifice flow measurement devices. As a general rule, choking occurs in a compressible flow when the total pressure upstream of an orifice is more than double that downstream of the orifice. A sonic condition develops in the nozzle, and this has the effect of decoupling the flow conditions downstream of the orifice from those upstream of the orifice (Anderson, 2003). The mass flowrate, m, of gas through the orifice can be found using the choking equation below, if the upstream pressure, p_o, orifice area, A, upstream temperature, T_o, ratio of specific heats, γ, and specific gas constant, R, of the gas are known.

$$m = \frac{p_o A}{\sqrt{T_o}} \sqrt{\frac{\gamma}{R} \left(\frac{2}{\gamma + 1} \right)^{(\gamma+1)/(\gamma-1)}} \qquad (6)$$

The mass flowrate of fluid through the orifice also becomes linear with respect to the pressure upstream of the orifice when choking occurs. If a precise and accurate pressure gauge is placed upstream of the orifice, and if the temperature and composition of the flow is known, the mass flowrate can be tightly controlled. The cross-sectional area of the orifice and the range of the pressure gauge determine the range of flowrates that can be obtained.

The inner combustion air, outer combustion air, and atomization air streams were controlled and measured separately before being fed to the burner. Orifices made by O-Keefe Controls (type E-125) were installed in each line to produce the necessary choking conditions. The manufacturer-supplied orifice calibration was used to determine the flowrates. The pressure upstream of each orifice was measured using battery-powered, digital pressure gauges (type DPG1000B-100G) manufactured by Omega Engineering. A NIST-validated calibration was supplied for the pressure gauges, and the rated precision of the gauges was 0.25% of full scale. The rated range of each pressure gauge was 0-100 psig. The temperature of the air entering from the compressor was measured using a battery-powered, thermistor-type thermometer installed in the air line near the orifices. The airline temperature was found to be quite stable, and was always nearly 22 °C, to within the 0.5 °C of precision provided by the thermometer. By addition of all the uncertainties and fluctuations in the system, it was found that the air flowrates were thus controlled to within 1% of the total flowrate fed at each condition.

Further modifications were made in order to introduce seeding material into the inner and outer combustion air streams. For non-intrusive optical fluid dynamic studies, it is necessary to introduce marker particles into the flow so that the motions of the flow can be tracked. In this case, a six-jet atomizer (TSI Model 9306) was used to introduce small droplets of propylene glycol into the combustion air flows. Compressed air was fed to the atomizer, and passed through up to six orifices in the atomizer. Since the flow through each atomizer orifice was also choked, the amount of seeded air passing through the atomizer was known, and this figure was added to the primary air flow in each stream to obtain the corrected air flowrate for each experimental case. The seeded air stream emerging from the seeder could be fed into one or both of the combustion air streams, and this distribution was controlled via valves on the seed air lines connected to each air stream. The seeding process and the properties of the droplets are discussed further in the diagnostics section, below.

4.5 Fuel System

The fuel supplied to the burner was stored in a pressurizeable stainless-steel vessel. The capacity of the vessel was 32 L. Special fittings were machined to allow the vessel to be pressurized. The fuel was then passed through a turbine flowmeter (MacMillan Model G112), calibrated for water. The fuel in this case was methanol, and the calibration was checked by direct flowrate measurements using a graduated cylinder and a stopwatch. It was found that volumetric flowrate reported by the unit was exactly the same for methanol as for water, to within the precision of the calibrating instruments used. The turbine flowmeter could thus be used to measure the flowrate of methanol to within 0.1 ml/min. A needle valve (from Swagelok), downstream of the flowmeter, was used to control the flowrate. It was found that the fuel tank pressure should be no more than 5 psig higher than the pressure at the atomizing nozzle. If there was a higher pressure drop across the needle valve used to regulate the fuel flow, outgassing of the fuel occurred, and vapor bubbles formed in the fuel line. This effect destabilized the flame, interrupted the atomization, and interfered with the experiment. At lower fuel pressures, however, the fuel did not outgas, and the fuel flowrate could be tightly controlled, to within approximately 1% of the measured flowrate.

4.6 Swirlers

The swirlers used to impart rotation to the airflows were of particular importance. In order to obtain a symmetrical flow, swirlers must be machined to within very tight tolerances. Swirl vanes may be flat, or they may be curved in a variety of ways (Gupta, et al., 1984). No matter what the type of swirler used, however, it is essential to machine the assembly very precisely. The types of machining operations available to produce swirlers are somewhat limited, and, if the swirlers are assembled from separate part, the difficulty of assembling them correctly increases dramatically. For this investigation, twisted-vane swirlers were employed, as these are compact, can be inserted directly into an air duct, and can be machined from a single piece of stock, without any further assembly steps.

In order to machine twisted-vane swirlers, aluminum blanks were first turned down to the precise diameters required. The blanks were initially simple cylinders, with sections cut to two diameters: one that let them fit tightly into sleeve for the next step in the machining process, and one that matched the required final diameter of the swirler. The centers of the blanks were then bored out to the required inner diameter necessary for each swirler. A special rotating assembly, attached to a precision stepper motor, was then attached to a vertical milling machine. Each blank was then secured in the rotating assembly, and the actual milling of the swirl vanes began.

The degree of twist associated with twisted-vane swirlers can be represented by some amount of rotation, θ_r, in degrees, per some lateral translation, t_Z, in units of length. Twist can thus be defined.

$$\boldsymbol{twist} = \frac{\boldsymbol{\theta_r}}{\boldsymbol{t_z}} \tag{7}$$

The swirlers were created as the blank was rotated a given number of degrees at each step, and the milling tool was advanced forward into the metal following the rotation. By repeating the process several thousand times, each vane was carved out of the metal. The details of the process are described in Appendix A. The tolerance associated with every step of the process was 25 microns, since this was the limit of precision of the machine tools employed. Once the vanes of each swirler assembly were formed, the part was cut off and trimmed to the correct length. An assistant, Guillaume Bourhis, carried out this series of operations over the course of several months, under the guidance of the author and Mr. Howard Grossenbacher (in the College of Engineering). Processes like this can certainly be automated, but a specially equipped machine shop and trained machinists are necessary to implement this automated approach. Due to time constraints and the costs involved, and the extremely unhelpful responses of some of the machinists consulted, it was found to be more practical to carry out the operations manually.

The process resulted in a set of inner and outer swirlers designed to be installed in the inner and outer air annuli of the burner. Each swirler had twelve vanes, and the vane thickness was approximately 1 mm in each case. The vane thickness varied slightly from swirler to swirler, due to the different degrees of twist, but, within an assembly, each vane was exactly the same thickness. The swirlers then needed to be characterized. Twisted-vane swirl assemblies can be described on the basis of their twist, but this parameter is not very helpful. The most important characteristic of any swirler is actually the outer blade angle, for the simple reason that centrifugal effects force rotating flows outward, and the swirl properties imparted to most of the air will depend on the properties of the swirl vanes near the outer wall of the duct. In a flat-vane swirl assembly, the local blade angle is a constant, and does not vary with radial location. In a twisted-vane assembly, the local blade angle, defined as the angle between the plane of the blade and the central axis of the assembly, varies with radial location, *r*, due to the twisted geometry. An expression for the local blade angle, θ_B, in a twisted-vane assembly is given below. Blade angle refers to the angle between the blade surface and the axial direction of the assembly. In the swirl assemblies used in this investigation, this is also the angle from the vertical direction.

$$\boldsymbol{\theta_B(r) = tan^{-1}\left(\frac{\theta_r * r}{t_z}\right)} \qquad (8)$$

or

$$\boldsymbol{\theta_B(r) = tan^{-1}(twist * r)} \qquad (9)$$

The outer blade angle, θ_o, of a twisted swirl assembly can be found if the dimensions and the twist of the vanes are known.

$$\boldsymbol{\theta_o = \theta_B(R_o) = tan^{-1}\left(\frac{\theta_r * R_o}{t_z}\right)} \qquad (10)$$

The important dimensions of a twisted-vane swirler are illustrated in Figure 8. They are the central radius, *Rc*, the inner radius, *Ri*, the outer radius, *Ro*, and the height, *h*. The swirl number of the flow through the assembly can then be approximated, as described by Gupta, et al. (1984):

$$S \approx tan(\theta_o) \qquad (11)$$

The main advantage of this approach is that the same approximation, based on the outer blade angle, applies to every kind of swirler, no matter the vane geometry. However, in practical flows, this approximation is found to be quite poor. The flow within each vane space and the interaction of the flows is too complex for a simple relation like this to really describe the flows. The effect of Reynolds number is also not taken into account by the approximation. In the present work, the swirl number of each swirler was therefore calculated on the basis of 3-D PIV observations of the flow emerging from the assembly. These observations are described in the chapter on results, below.

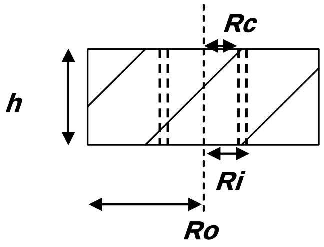

Figure 8. Swirler dimensions

For purposes of comparison, each swirler was classified according to its outer vane angle, and according to type (the two types being inner and outer). For example, a swirler designed to be inserted in the inner air duct, and featuring an outer vane angle of 45 degrees, is referred to as swirler 45-i. A swirler designed to be inserted into the outer air annulus, and featuring an outer vane angle of 42 degrees, is referred to as swirler 42-o.

Four inner and four outer swirlers were used in the course of the experiments described below. They are shown in Figure 9. The inner swirlers featured outer vane angles of 0, 30, 45 and 60 degrees (from the vertical axis). The outer swirlers featured swirl angles of 0, 42, 70, and –70 degrees (counter-swirl). Swirlers with a positive outer vane angle imparted counter-clockwise rotation to the air (seen from the top into the burner), while the one outer swirler with a negative outer vane angle caused the air to rotate in a clockwise direction. This unique swirler was created so that the effect of counter-rotation on the structure of the flame could be examined. In a counter-rotating arrangement, the air streams in the inner and outer annuli rotate in opposite directions. Swirler assemblies with a 0 degree swirl angle are essentially flow straighteners, and are referred to as null swirlers. The Null-o swirler, shown in the second row in Figure 9, is not made from aluminum, but is an older type, manufactured from brass. It shares the same dimensions as the new aluminum assemblies. The dimensions and properties of the swirlers used in the current investigation are given in Table 1.

One important consideration with regard to swirlers is pressure drop. An attempt was made to measure the pressure drop across each swirler under conditions similar to those used in the experiments described below. A special duct was created, which allowed air to be forced through each swirler individually. The static pressure upstream of the swirler was measured with an inclined manometer. Approximately 10 g/s of air

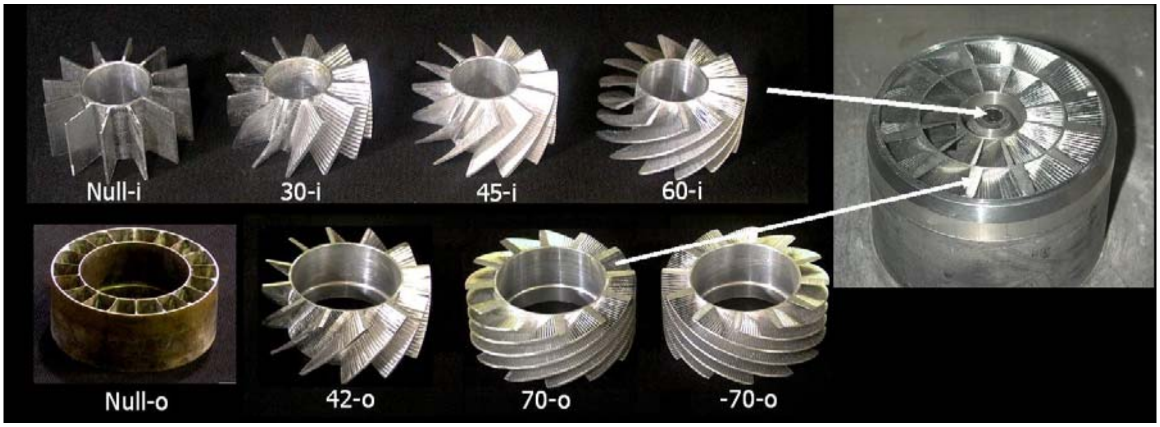

Figure 9. Swirlers used in the swirl-stabilized spray burner

were fed through each swirler. Unfortunately, the pressure drops were almost uniformly too low to be measured. Even with the manometer inclined to 80 degrees from vertical, pressure drops no larger than a few cm of water were observed, and these could not be measured accurately with the manometer. The 60-i swirler, which produced the largest pressure drop due to its dimensions and steep swirl vane angle, produced a pressure drop of only 2 cm of water. The uncertainty associated with the measurement was nearly as large as the measurement itself. What is clear, however, is that swirl can be imparted very efficiently to a flow, at very small pressure drops, if these swirlers are employed.

Swirler	*Type*	*Ri (mm)*	*Ro (mm)*	*Rc (mm)*	*Height (mm)*	*Material*	*twist (°/mm)*	*θ_o (in degrees)*
Null-i	inner	9.53	19.82	8.71	18.71	Alum.	0.00	0.00
30-i	inner	9.53	19.82	8.71	18.71	Alum.	1.69	30.30
45-i	inner	9.53	19.82	8.71	18.71	Alum.	2.83	44.50
60-i	inner	9.53	19.82	8.71	18.71	Alum.	5.06	60.30
Null-o	outer	20.70	30.99	19.86	25.40	Brass	0.00	0.00
42-o	outer	20.70	30.99	19.86	25.40	Alum.	1.69	42.40
70-o	outer	20.70	30.99	19.86	25.40	Alum.	5.06	70.00
-70-o	outer	20.70	30.99	19.86	25.40	Alum.	-5.06	-70.00

Table 1. Properties of Swirlers

4.7 Fuel Atomization Nozzle

The twin-fluid fuel atomization nozzle, and its location relative to the swirl assemblies, is shown in Figure 10. The nozzle was positioned on the centerline of the injector assembly, and brought a non-rotating stream of fuel into contact with a stream of swirling atomization air. The type 30610-1 nozzle,

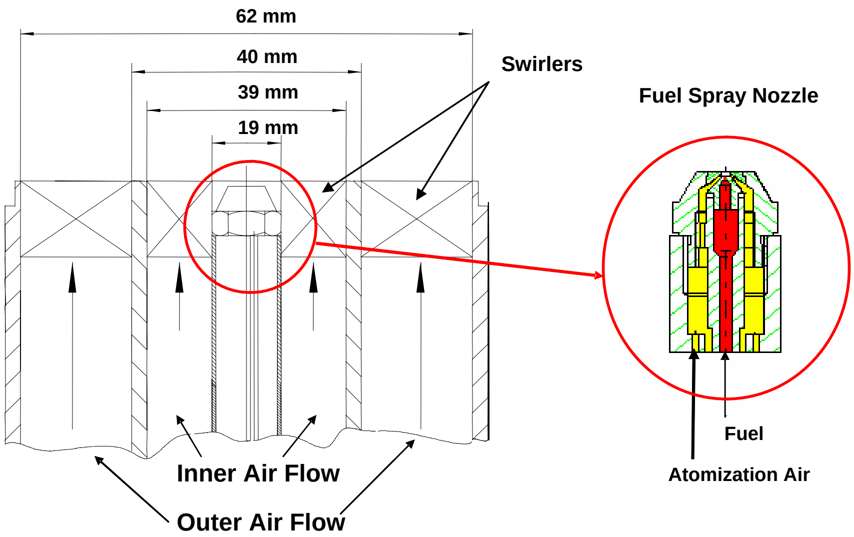

Figure 10. Schematic of injector, showing swirlers and fuel nozzle

produced by Delavan Spray Technologies, was commercially available. It was rated by the manufacturer to atomize 1.9 L per hour of water, using an air pressure drop of 0.68 bar and an atomization air flowrate of 22.6 standard L/m (Delavan, 1998). The nozzle produced a solid-cone spray, with a mean droplet diameter of approximately 30 to 50 µm.

4.8 Mixing Chamber

The mixing chamber, installed on top of the combustor, is shown schematically in Figure 11. The base of the chamber was an aluminum baseplate, 1" thick, equipped with slots into which the walls could be set. The walls were made of transparent plastic, and were screwed together so that the walls supported themselves with no support frame. A nylon lid, also 2.54 cm and slotted, enclosed the top of the chamber. Four exhaust ports, equipped with stainless steel trap stacks, were cut through the lid, in order for the exhaust gases to escape. The horizontal cross-section of the chamber was square, and the dimensions of the chamber are shown in Figure 12.

The exhaust jet tended to entrain water, and to expel this water from the top of the tank. The jet also violently agitated the water, and this caused large-scale sloshing of water in the chamber. This sloshing was quite problematic, in that it caused the entire experimental facility to rock violently back and forth if it remained uncontrolled. In addition, high-velocity exhaust jets, with average velocities on the order of hundreds of m/s, were found to produce very small bubbles, with diameters on the order of 10-100 microns. These bubbles recirculated in the water, completely obscuring the exhaust jet and making optical examination of the jet impossible. In order to examine jets with average velocities on the order of at least 400 m/s, it was necessary to control the large-scale motion of the fluid in the mixing chamber, as well as these small bubbles, without compromising optical access, and without interfering in the development of unstable interactions between the exhaust jet and water near the exhaust port.

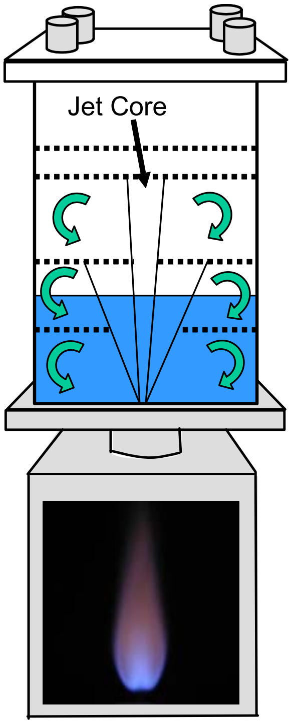

Figure 11. Submerged combustor arrangement

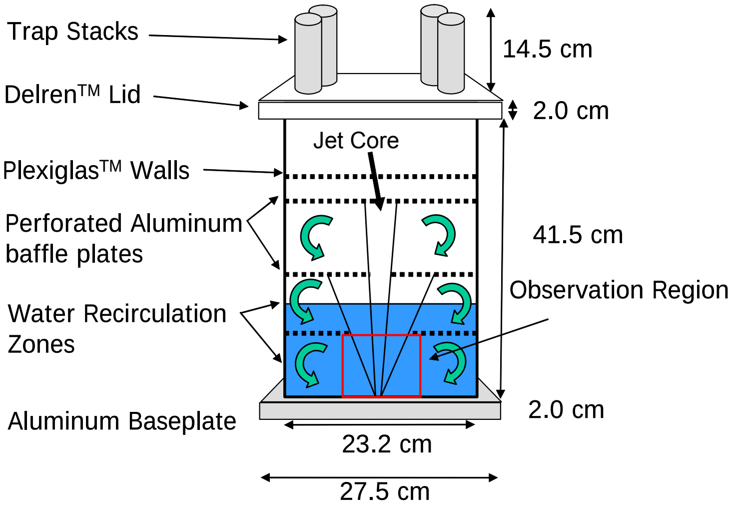

Figure 12. Mixing chamber components and dimensions

To this end, a four-stage baffle cartridge was developed. No particular theory was applied during the design, but the approach was similar to that employed in fuel tanks for liquid-fuelled rockets. Designs were tested iteratively until a satisfactory arrangement was obtained. It was found that the four-stage approach separated the chamber into four separate recirculation zones, in which the vapor was effectively separated from the liquid.

The resulting baffle cartridge is shown in Figure 13. The baffles were made of perforated aluminum, with a 33% porosity ratio, and were attached to the lid via aluminum struts. A wide hole was cut through the lowest baffle plate to allow the exhaust jet to pass through with very little interference. The purpose of this plate was to interfere with very small bubbles, which tended to travel down along the walls. This plate caught the bubbles and prevented them from traveling all the way down the walls, where they would interfere with observation of the exhaust jet.

The second plate had a smaller hole cut through the center. The purpose of this hole was to allow the vapor core of the exhaust jet to pass, while restricting the passage of entrained liquid at the edges of the jet. Finally, the last two baffle plates were designed to trap any remaining entrained liquid.

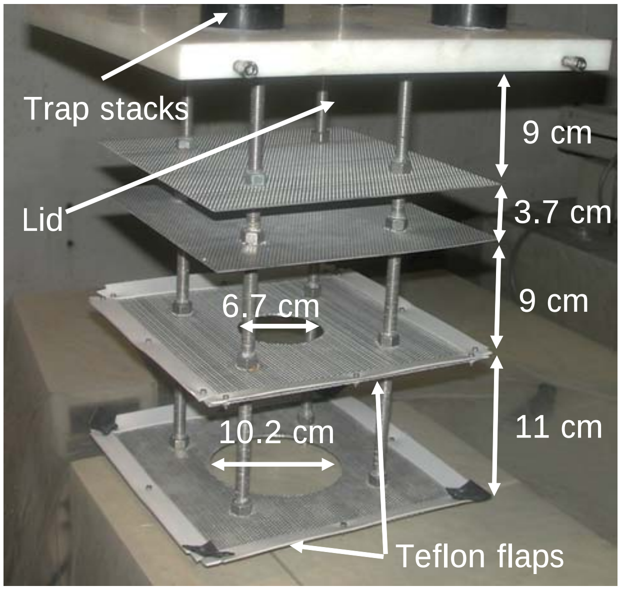

Figure 13. Baffle cartridge for mixing chamber

The trap stacks on top of the lid were also fitted with internal wire screens, which effectively trapped mist and fine droplets. It was found that, once the proper baffle design had been developed, fast moving exhaust jets could be effectively observed in the mixing chamber. The trap system was so effective that the amount of liquid escaping from the mixing chamber dropped to nothing; only the finest mist, entrained in the exhaust stream from the trap stacks, was observed.

4.9 Exhaust Nozzles

Considerable work has been done on the development of turbulent interactions between jets and surrounding fluid in single-phase situations. The interface between the fast-moving jet and the stationary ambient fluid has been found to develop Kelvin-Helmholtz instabilities (KHI), and the resulting turbulent structures have been found to display certain characteristic Strouhal numbers (Schadow and Gutmark, 1992). The Strouhal number, *St*, of an instability is given by:

$$St \equiv \frac{f * L}{V} \tag{12}$$

The Strouhal number nondimensionalizes the frequency, *f*, of an event occurring in the flow, using the characteristic length, *L*, and the mean flow velocity, *V*. In single-phase systems, it has been found that the geometry of the exhaust nozzle may have a significant effect on the unstable behavior of these flows. Changes in the radius of curvature along the nozzle wall, which produce turbulent structures of different length scales at the interface, have been shown to assist in mixing between the fluid in the jet and the surrounding material (Gutmark and Grinstein, 1999). These changes in nozzle geometry can change the Strouhal number of turbulent structures developed at the jet boundary, which affects mixing and noise emission associated with these flows.

Very little is known about jet interaction in a two-phase environment. The presence of a two-phase interface, and the incompressibility of a liquid phase, as well as the presence of significant buoyant forces, make the behavior of the interaction much more difficult to predict or characterize. In high-speed flows, where a sonic condition may be present in the nozzle, shockwave interactions at the interface may also play a role.

In order to shed some light on these issues, three exhaust nozzles were developed. Each was cut from type 304 stainless steel, and was fitted with an o-ring to provide an effective seal. The nozzles are shown in Figure 14.

4.9.1 Flush-Mounted Nozzle (FMN)

The first nozzle was a simple flush-mounted design. The dimensions of the nozzle are shown in the schematic in Figure 15. In this nozzle, the flow is constricted in the throat, and the downstream lip of the nozzle is mounted flush with the face of the mixing chamber baseplate. No attempt was made, in this design, to modify the behavior of the jet or two-phase interface in any particular way.

4.9.2 Conical Projecting Nozzle (CPN)

The second nozzle projected 40.64 mm above the level of the baseplate, and tapered in a conical fashion to the final jet diameter of 8.71 mm. The nozzle is shown schematically in Figure 16. The objective, in this case, was to compare the projecting nozzle with the flush-mounted nozzle, and to observe any changes in the behavior of the interface caused by the changed geometry.

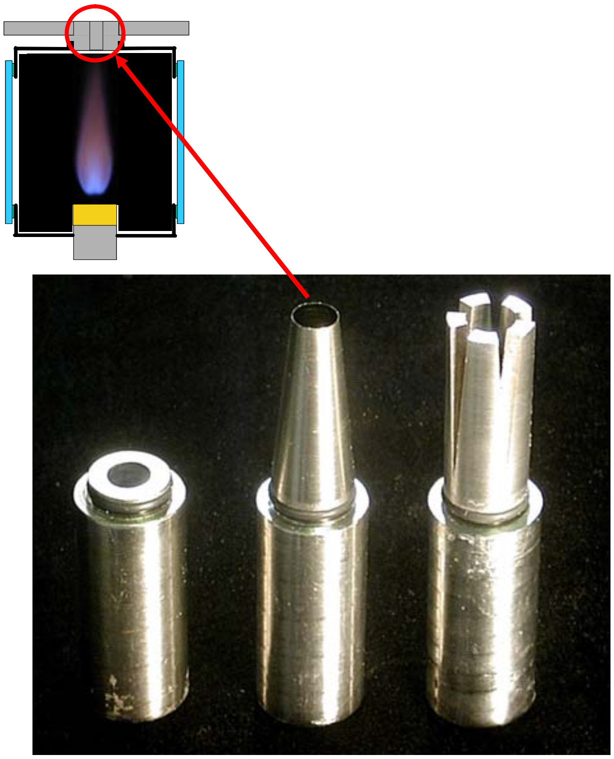

Figure 14. Flush-Mounted (left), Conical Projecting (center), and Corrugated Converging-Diverging (left) exhaust nozzles

4.9.3 Corrugated Converging-diverging Nozzle (CCDN)

The final nozzle examined was a converging-diverging nozzle, design to produce a fully-expanded or over-expanded jet for any throat Mach number conditions up to Mach 1.5. Shown schematically in Figure 17, the nozzle projected 40.64 mm above the baseplate, as in the case of the conical projecting nozzle. The flow was constricted, just as in the case of the other two nozzles, but, in this case, the duct area was then expanded by 20%. The projecting walls of the nozzle were also shaped in order to apply some of the more advanced techniques for control of jet instabilities described by other authors (Gutmark and Grinstein, 1999, Hu, et al., 2000). Five

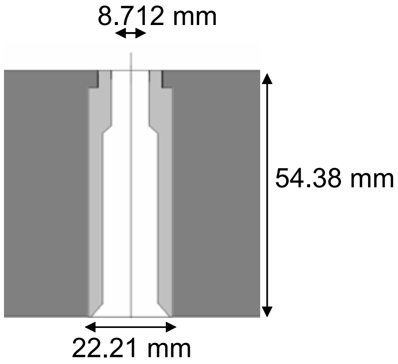

Figure 15. Flush-mounted nozzle

corrugated, tapering slots were cut into the walls of the nozzle. These can be seen in detail in Figure 18. The corrugations were cut in such a way that the wall of the combustor was perforated; this allowed the jet to interact with the liquid at a number of points, and along an interface with many local radii of curvature. In single-phase systems, this approach has been shown to change the length scales of mixing interaction between the fast moving jet and the surrounding fluid; and the objective of the CCDN design was to examine the effect of these nozzle features in a two-phase interaction situation.

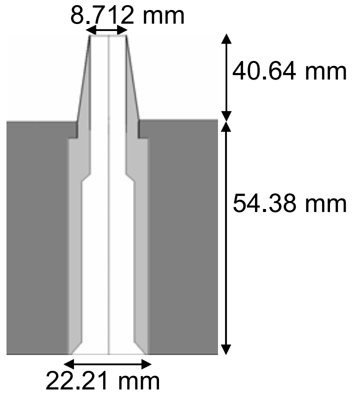

Figure 16. Conical projecting nozzle schematic

Experiments were undertaken under three conditions, shown schematically in Figure 19. In the unenclosed condition, the combustor enclosure and mixing chamber were absent. In the enclosed, un-pressurized condition, the combustor enclosure was installed, but the exhaust nozzle and mixing chamber were not present. In the enclosed, submerged condition, the exhaust nozzles and mixing chamber were present, and the combustor pressure depended on the mass flowrate of the material entering the combustor, and on the heat released by a flame, when a flame was present.

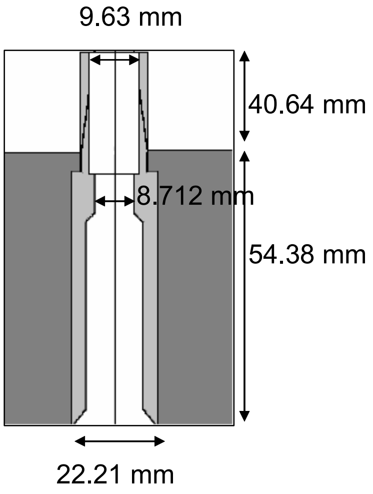

Figure 17. Corrugated converging-diverging nozzle schematic

5. Diagnostics

This section will deal with the diagnostic equipment used in the course of the experiments. Details regarding the type and accuracy of each instrument will be given, along with a consideration of the uncertainty associated with each diagnostic technique.

Figure 18. Detail of corrugated converging-diverging nozzle, showing corrugations and perforations through nozzle wall

5.1 Chamber Pressure Gauge

The pressure in the combustor chamber was measured using a battery-powered digital pressure gauge. The gauge was type DPG1000B-100G, manufactured by Omega Engineering. The range of the gauge was 0-100 psig, with a rated accuracy of ±0.25 psig. The unit was calibrated to a NIST standard by the manufacturer, and was compared, on arrival, with several similar gauges. In every case, the reading was found to meet the standard of accuracy stated by the manufacturer. This was the same type of pressure gauge used to measure the flowrates of air to the injector.

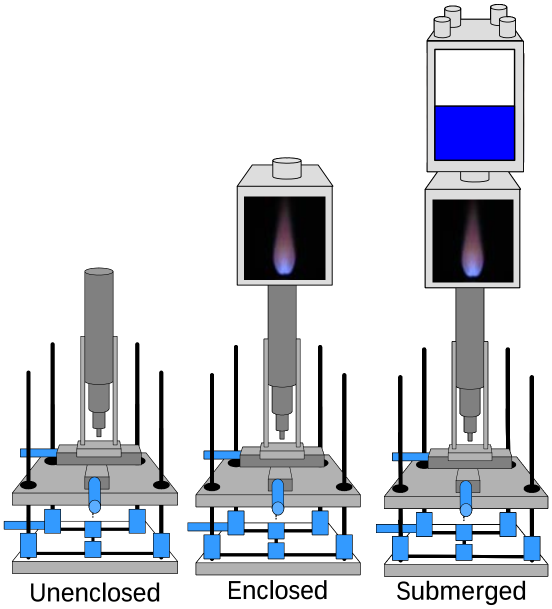

Figure 19. Schematic representation of combustor experimental conditions

5.2 Exhaust Temperature Thermocouple

The temperature of the exhaust gases was measured in two cases where the combustor was enclosed and operated at approximately 1.07 bar total pressure. The mixing chamber was not installed in this set of experiments, so that the mean centerline exhaust temperature could be measured conveniently. A type-K thermocouple, with a 1.5 mm bead diameter, was used, and a Cole-Parmer Model 8534-75 digital thermocouple readout was used to display the temperature. The system was calibrated by the manufacturer, and the calibration was checked in the temperature range 0 ºC to 100 ºC in the laboratory using an ice bath and boiling water. The thermocouple was found to be accurate in this range to within 0.2 ºC. The combustor centerline temperature exceeded this range, however, and was seen to fluctuate considerably. The highest centerline temperature measured was on the order of 700 K. Radiation losses from the thermocouple junction were negligible at this temperature, and were not considered. However, due to the fluctuations in the temperature measured, there was a ± 23 K confidence interval associated with the centerline temperatures measured and reported below.

5.3 Sound Spectrum Analysis:

A sound spectrum analyzer was used in order to gain insight into the dynamic behavior of the two-phase exhaust jet regime in the mixing chamber. Manufactured by TerraSonde, the analyzer was connected to a piezoelectric microphone, which was attached to the baseplate of the mixing chamber. The analyzer recorded the signal from the microphone, and performed a fast-Fourier transform (FFT) on the signal. The analyzer was capable of examining frequencies between 10 Hz and 21,000 Hz. In the experiments reported below, however, the unit was operated in low range mode, which increased the sensitivity of the instrument in the 10 Hz to 332 Hz range. Thus, only sound pressure levels associated with frequencies in this range were monitored. A variety of options were available to customize the spectrum obtained; the most important of these was the averaging time. In the experiments described below, the sound spectrum was averaged over 30 seconds. The sound pressure level associated with each frequency in the spectrum was found to stabilize to within 0.5 decibels when this procedure was followed. The unit was calibrated by the manufacturer, and no convenient test for the calibration was available. However, the values reported by the unit for certain test cases, such as a quiet room, were found to be reasonable. The spectra obtained were always repeatable for identical experimental conditions. Since the main purpose of the tests involving the sound spectra involved comparison of spectra obtained under various conditions, the instrument was found to be quite well suited to this set of investigations. Data files containing the sound spectra were transferred to a PC through an RS232 connection, and imported into an Excel^{TM} spreadsheet.

5.4 Global Flame Imaging

The global features of flames associated with the combustor were examined and recorded with a full-color digital camera. The camera in question was a Nikon CoolPix 990 with a 3.3 megapixel detector. Aperture, exposure times and focal length could all be controlled manually or automatically. Manual control was employed, in order to optimize the images obtained. In the experiments described below, a 0.5 second exposure time was used to image the flame. The long exposure time was necessary for two reasons. First, methanol produces a dim flame, with limited luminosity. Second, the flames were quite turbulent, and it was found that a 0.5 second integration interval helped produce repeatable flame features from one image to the next. Flame luminosity is generally an indicator of heat release, and, since the methanol flame front produced sufficient observable radiation in the visible spectrum, the images obtained show the averaged regions of heat release associated with the flame. The images were scaled with the aid of reference exposures, wherein grids of known dimensions were photographed. These grids could then be overlaid onto the flame images. The main limitation was the number of pixels in the images. All dimensions associated with the flame images are accurate to the nearest millimeter.

5.5 High-Speed Imaging

Due to the limited diagnostic techniques available for unstable two-phase flows, the two-phase interaction in the mixing chamber was imaged with a high-speed camera. The camera used was a Photron Ultima 1024, capable of producing monochrome images with 1024X1024 resolution at low frame rates (up to 500 frames per second) and with decreased resolution at higher frame rates. The camera was capable of acquiring images at up to 10,000 frames per second (fps), with very limited resolution at the maximum frame rate. The camera had an internal memory buffer with 512 Mb of capacity. The number of images that could be stored in the buffer depended on resolution. In the present work, the images obtained were acquired using 500X500 pixels of resolution, at 500 fps. This mode of operation was found to provide an optimal tradeoff between framerate, number of images, and available memory. Dimensions of structures in each frame were scaled using the nozzle dimensions as a reference. This approach helped account for distortions in each image introduced by the unstable two-phase environment.

The ultimate limitation in precision was the resolution of the image. The size of any feature in each image could be determined to the nearest 0.1 mm.

5.6 Fuel Spray Characterization

The fuel spray produced by the twin-fluid atomizing nozzle was characterized with a phase-Doppler particle analyzer (PDPA) manufactured by Aerometrics (Aerometrics, 1998). The type of system used provided two components of droplet motion, as well as droplet size information about each droplet measured. The PDPA technique involves the projection of four laser beams toward a single point in space. The junction is shown in Figure 20. The laser beams were obtained from a single continuously-emitting argon-ion laser, with a maximum rated output of 300 mW. The laser emitted at several frequencies; the most useful of these were at 488 nm and 514.5 nm. The 488 nm wavelength was blue in color, while the 514.5 nm wavelength was green. The radiation from the laser was passed into an Aerometrics Fiber Drive unit, where the light was conditioned in order to make the PDPA technique possible. The fiber drive contained a prism, reflectors, and a Bragg cell, which split the initial beam into colors, and then split each color into two beams of equal intensity. In each beam pair, one beam was frequency-shifted by 40 MHz. The beams were linearly polarized, with the blue beams having a vertical polarization and the green beams a horizontal polarization. The beams were fed through fiber-optic transmission lines to the emitter, where they were passed through a lens with a 500 mm focal length.

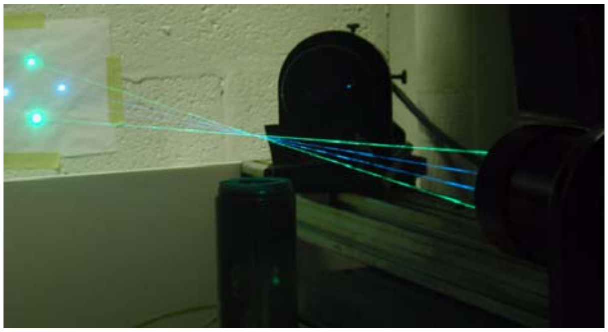

Figure 20. Set-up for phase Doppler particle analysis system

Thus, the beams were caused to intersect at a point 500 mm from the center plane of the emitter lens. When they intersected, the polarized, frequency-shifted beams formed a measurement junction, in which the green and blue lasers formed interference patterns. The interference pattern of the green beams was horizontally-oriented, while the pattern of the blue beams was vertically-oriented. A droplet or particle passing through the junction scattered light, and the shape of the scattering signal depended on the droplet's size and velocity. Since the droplets were in the 1 micron to 200 micron range, the type of scattering observed was generally Mie scattering, though geometric optics played a role in the scattering characteristics of the largest droplets.

The scattering signal generated by each particle was captured by an optical receiver unit. The receiver featured a lens with a focal length of 500 mm, and was positioned 30 degrees off the forward axis of the transmitter. The receiver was focused so that the image of the measurement junction fell on a mask, which was specially patterned to transmit the scattered light to three detectors positioned in the body of the receiver unit. Two of the detectors featured narrow-band-pass filters that transmitted only the green light, and were separated by a known distance. The third detector was positioned behind a filter that transmitted only the blue laser light. The two green laser receivers were necessary, so that the size of each droplet could be measured. The frequency of the scattering signal depended on the droplet velocity. However, when two detectors were used, the signals arriving at the detectors were phase-shifted. By analyzing the frequency of the green and blue signals, the droplet velocity in the axial and radial directions could be obtained. The size of each droplet could be obtained by analyzing the phase shift of the two green scattering signals.

The light captured by the receiver was transmitted through fiber-optic lines to three photomultiplier tubes (PMT). Each tube responded to light from a particular detector. When a voltage was applied to each tube, the incoming optical signal produced an electrical signal. The electrical signals were fed to a pair of real-time signal analyzer (RSA) units. One unit analyzed the signals from the green laser detectors, the other handled the signal from the blue detector. Since the signals were transmitted through electronic channels, the data was split out by channel. The information from the green laser arrived on Channels 1A and 1B, and the information relating to the blue laser arrived on Channel 2. Thus, axial velocity and size information were associated with Channel 1, and radial velocity information arrived on Channel 2. Information was then sent to a data acquisition board, built into a commercially available PC. A Dataview^{TM} application on the PC received and processed the signals from the RSAs, and displayed system settings and output to the user. The user also controlled the RSAs, including the PMT tube settings, using the Dataview^{TM} application.

The maximum data acquisition rate for the unit was quite high, and tens of thousands of droplets could be characterized per second. It was important to ensure that data obtained from each channel was matched up for each droplet, so that axial velocity and radial velocity information could be displayed on a droplet-by-droplet basis. Data acquired during a run had to be validated, since it was desired that all information be matched to a particular droplet. A gate time was specified for any incoming signal, so that the two velocity signals arrived within a particular interval. If the delay between the signals fell within the gate time, the droplet information was considered to be verified.

Further verification was necessary to ensure that the droplet was spherical. This was ascertained by examining the features of the phase-shifted signals captured by the Channel 1 detectors. Correlations have been developed by the manufacturer for particular droplet sizes, droplet indices of refraction, and equipment geometries. If the received signals do not fall within the bounds established by the correlations, the droplets are either too large, too small, non-spherical, or some combination of these. Verified droplets must therefore meet the criteria associated with the correlations.

Sprays are generally characterized in terms of droplet components of velocity, droplet size distribution, and the spray density (frequency of arrival in the measurement volume). If a verified data set can be obtained, and the dataset is of sufficient size, sprays can be characterized in great detail. It has been found that it is necessary to measure at least 10,000 droplets at each location, or, in the interests of efficient data acquisition, to let the instrument acquire data for up to two minutes (Avedisian, et al., 1994).

Specific procedures were followed in order to ensure that the spray was characterized accurately. The laser power supplied had to be great enough to produce measurable scattering signals when the smallest droplets of interest passed through the measurement volume. The voltage supplied to the photomultiplier tubes also had to be increased to improve low-end sensitivity. However, there was a limitation. If larger droplets were present in the spray, and the low-end sensitivity of the unit was too high, the signals from the largest droplets flooded the channels, meaning that the voltage of the electrical signal from the PMT tube exceeded the upper range of the RSA. When these events occurred, warning lights flashed on the front of the RSA, indicating that the channel was flooded. In a polydisperse spray, the laser power and PMT voltage had to be optimized so that each channel was flooded less than 1% of the time at the point in the spray where flooding of the channel was most likely to occur. Data could then be acquired throughout the spray, using these settings. This meant that some of the smallest droplets were not measurable, since their signal was lost in the background noise associated with the system. However, it has generally been found that, when the correct procedure is followed, the vast majority of droplets present in the spray can be measured effectively. Measurements carried out by the manufacturer indicate that results obtained using the approach outlined above compare extremely well with those provided by other optical measurement techniques, such as ensemble-scattering-based Fraunhofer diffraction.

Each channel also had to be calibrated using a calibration diode. First, the correct laser power and PMT tube voltage were established. Then, the receiver was covered, and the calibration diode was activated. The diode produced a signal with known characteristics, which was introduced directly into the PMT tubes. A special calibration screen was then accessed in the Dataview^{TM} application. The accuracy of the droplet size measurement technique depends on the phase information associated with the droplet scattering signals. This phase information will change whenever the PMT voltage is changed, since each PMT has a particular delay time between the point when an optical signal is received, and the point when the electrical signal is produced. In order to accurately calibrate the unit, the known signal from the calibration diode was fed into the PMTs, and calibration parameters in the software were adjusted until the phase information in the acquired signal matched that produced by the calibration diode.

It is also necessary to condition the laser beams properly in order to obtain good results. For the experiments described below, the laser power of each beam pair was matched using a power-of-extinction technique. The beam intensities were controlled using adjustment knobs on the fiber drive couplings, and were matched in such a way that both beams became undetectable to the eye at the same minimum power setting. The targeting of the beams was checked using a microscope objective placed at the measurement junction. All four beams were found to intersect at the same point, with nearly-total overlap. The polarization of each beam was checked with a linearly-polarized filter, and the polarization adjusted until all four beams had the correct polarization. The emission power of the argon-ion laser was set to 250 mW.

The fuel spray was then found to produce the maximum allowable channel flooding when the PMT voltage was 600 V. A calibration was applied. Since the burner could be translated with great precision in three dimensions, data was taken at a series of radial locations above the fuel nozzle. At each location, data was taken until 10,000 droplets had been detected, or until 120 seconds had elapsed. Peak droplet acquisition rates were on the order of 4000 Hz. 97% to 99% of detected droplets could be successfully verified. Verified data was recorded for the droplets at each location. Statistics of the droplet population were then developed by the Dataview^{TM} application provided by the manufacturer, and transferred into a spreadsheet for further analysis. Droplets were found to display diameters in the 1.5 to 200 micron range, with arithmetic mean values in the 30-40 micron range. Values were found to be very repeatable, particularly in regions where the frequency of droplet acquisition was greater than 50 Hz. Mean diameters were found to vary by approximately 0.5 microns from one run to the next, and mean velocities varied by less than 1% between successive runs at a single location.

It should, at this point, be obvious that the PDPA technique requires patience and expertise in order to ensure accuracy. When properly applied, however, the technique is quite powerful, providing droplet-specific information not available from other diagnostic techniques.

5.7 Air Flowfield Characterization via 3-D PIV

5.7.1 Seeding

The swirling air flow associated with the burner was characterized under nonreacting conditions, and in the absence of a fuel spray, using a 3-D particle image velocimetry system developed by Integrated Design Technologies (IDT). In order to apply this technique, the airflow was seeded with propylene glycol droplets. Effective PIV depends on effective seeding. Seed particles or droplets in the flow must be small enough to follow the motion of the flow, but must be large enough to be imaged effectively by a camera. In order to address the accuracy of the PIV technique, the properties of the seeding droplets must be discussed.

Swirling airflows in practical applications are generally turbulent. The smallest features of a turbulent flow depend on the length scales of the turbulent structures present. The smallest length scale is referred to as the Kolmogorov scale of the flow, and represents the spatial and temporal scale on which kinetic energy in the form of fluid motion is reduced to thermal energy by viscous effects (Bernard and Wallace, 2002). In order to follow the motions of a turbulent flow effectively, a particle in the flow must be able to follow these motions of the flow with high fidelity.

The spatial Kolmogorov scale, η_χ, of a flow can be estimated if the properties of the flow are known. The calculation involves the viscosity, ν, characteristic length, L, and maximum mean velocity associated with the flow, V_{max}.

$$\eta_{\chi} \approx \sqrt[4]{\left(\frac{v^{3} * D}{V_{max}{}^{3}}\right)} \tag{13}$$

The equation above allows the spatial Kolmogorov scale to be estimated. The maximum mean velocity associated with the flow, V_{max}, can then be used to convert the spatial Kolmogorov scale into a temporal scale. The temporal Kolmogorov scale, η_{τ}, determines the smallest temporal scale in the flow.

$$\eta_{\tau} \approx \frac{\eta_{\chi}}{V_{max}} \tag{14}$$

The ability of a particle or droplet to follow the motion of a flow depends on its characteristic relaxation time, τ_d. The characteristic relaxation time can be estimated on the basis of the Stokes drag, which assumes the object is spherical and that the flow over the surface is a creeping flow at very low Reynolds number (Raffel, 1998, Mörtberg, 2005). An estimate of τ_d can be found using the droplet diameter, d_d, droplet density, ρ_d, and dynamic viscosity of the flow, μ.

$$\tau_{d} = d_{d}{}^{2} * \frac{\rho_{d}}{18 * \mu} \tag{15}$$

It is not usually necessary for the droplet characteristic time to be equal to the temporal Kolmogorov scale. Hot wire probes, which have been used extensively in studies of turbulence, are not usually small enough to allow the Kolmogorov scale to be resolved. Mean properties of the flow, such as mean velocities, can be obtained very effectively if the smallest measured scale in the flow is an order of magnitude greater than the Kolmogorov scale. Most important turbulent behavior of the flow, including dissipation of turbulence, can be examined effectively if the smallest measured scale in the flow is 5-10 times the Kolmogorov scale (Wallace, 2005). Mean velocities can be very accurately obtained even if the smallest measured scale is more than an order of magnitude larger than the Kolmogorov scale of the flow.

In order to examine the behavior of the flows described below, the combustion air flows were seeded with polydisperse propylene glycol droplets with mean diameters in the 4-5 micron range. The droplets were produced using a TSI Model 9306 six-jet atomizer, as described above. HPLC-grade propylene glycol was found to be a very effective seeding agent. Liquid droplets (as opposed to solid particles) are generally preferred for nonreacting flows, since solid particles will tend to deposit on surfaces, enter optical equipment, and change tolerances on machined components. Solid particles small enough to be used in studies of turbulent flows can be dispersed only with difficulty, and may form agglomerates, depending on the dispersion strategy employed. Liquid droplets, however, must have a very low vapor pressure in order to be effective. Water is generally ineffective, due to the short lifetime of water droplets. Oil droplets have useful lifetimes, but tend to deposit on sensitive experimental equipment. Olive oil, which has been employed by some authors, is extremely problematic, since it contains a variety of compounds which form a resilient, sticky residue on every surface in the vicinity of the experiment (Raffel, 1998). The residues associated with olive oil will also destroy tolerances in the seeder equipment, making effective seeding impossible.

After some investigation, it was found that HPLC-grade propylene glycol can be atomized effectively, forms droplets with useful lifetimes in the flows of interest, and evaporates completely and relatively quickly from surfaces with which it comes into contact. The volumetric flowrate of seeded air obtained from the atomizer depends simply on the flowrate of air fed to the atomizer. The droplet size distribution and droplet density in the flow of seeding air from the atomizer are insensitive to seeding air flowrate. The seeding air flowrate must be added to the combustion air flowrate in order to obtain the total flowrate of the seeded airflow. However, it was found that, in order for effective seeding to be obtained, the seeding air flowrate need only form ~5% of the total air flowrate. As will become clear in the results presented below, this additional airflow is not large enough to significantly affect the flow properties.

As described above, the Kolmogorov scale associated with the flow, based on the properties of air and the length scale and mean velocities associated with the flow, can be obtained. For the flows examined in this work, η_τ was estimated to be $2*10^{-6}$ s. Since the properties of the propylene glycol droplet population are known, the characteristic relaxation time of the droplets, τ_d, can be estimated, and was found to be approximately $6*10^{-5}$ s.

It is clear, then, that the characteristic time of the droplets represented approximately 30 Kolmogorov scales. It can therefore be concluded that properties of the flows examined here, such as mean velocities, can be effectively examined through use of the seeding scheme described above.

5.7.2 Laser Illumination for PIV

In order for PIV to be carried out, the droplets seeding the flow must be illuminated with a laser sheet. In the present investigations, the laser sheet was obtained from a New Wave Research Gemini PIV Laser system. The 532-nm pulse laser system consisted of two Nd:YAG laser cavities with separate power supplies and forced-convection water cooling. The laser cavities were controlled separately by a timing hub. The pulses emitted by the cavities were passed through a series of reflectors, which focused both beams through a single emission aperture. The laser pulse from each cavity initially had a top-hat intensity profile, and the diameter of each pulse was approximately 5 mm. The pulses were then passed through a focusing lens with a focal length of 500 mm. The final lens in the optical train was a cylindrical lens, which caused the round beam to spread out into a two-dimensional sheet. The beam power was greatest near the center of the sheet, and decreased toward either edge. The light rapidly lost its top-hat intensity distribution as it is passed through the lenses, resulting in an approximately-Gaussian intensity distribution on either side of the laser sheet centerline. The result was a triangular sheet of laser light with an included angle of approximately 30 degrees. The thickness of the sheet decreased with increasing distance from the cylindrical lens, and reached a minimum thickness of approximately 1 mm at a distance of approximately 500 mm from the cylindrical lens.

For the purposes of the current investigation, the sheet was oriented vertically, as was the experimental flow. The lower half of the laser sheet was blocked by an aluminum trim plate, which could be moved up or down with great precision. Secondary reflections of laser light can make PIV extremely difficult, so the trim plate was positioned very carefully to prevent reflections from the combustor hardware. A beam stop, painted matte black, was positioned behind the combustor to absorb as much as possible of the stray light from the laser.

Accurate PIV depends on careful laser pulse conditioning. The flashlamp power for each cavity was tuned in order to ensure that each cavity emitted the same pulse energy during operation. The energy of each pulse was controlled by adjustment of a global Q-switch setting, which determined the period of time during each pulse when the cavities could effectively emit. The cavities produced pulse energies between 50 to 200 mJ. The duration of each pulse was approximately 3-5 ns. The exact duration of the pulse depended on the Q-switch setting, but the pulse was, in any case, sufficiently short to allow droplets to be imaged at a particular location in space without noticeable streaking.

Beams emerging from both laser cavities were carefully aligned, so that each cavity illuminated the same section of the flow. In order to check and adjust the alignment, a pinhole, 0.5 mm in diameter, was positioned at the beam waist created by the focusing lens. The cylindrical lens was removed, so that the round beam could emerge from the emitter cavity, and the internal reflectors in the head were adjusted until pulses from both cavities fell through the pinhole. The cylindrical lens was then reinstalled, and the laser sheets obtained from each cavity were found to coincide extremely well.

The laser head was pumped and fired at 5 Hz, meaning that each cavity fired at 5 Hz, and one cavity fired in close succession to the other. The time interval between pulses is an important PIV parameter, and must be carefully adjusted for the particular flow being examined. In general, useful pulse intervals were found to be between 2.5 and 13 microseconds. Faster-moving flows must be imaged with a smaller pulse interval, while slower-moving flows must be imaged with a longer one. The illumination provided by the laser cavities was found to be extremely stable and repeatable.

5.7.3 Camera Setup

In PIV, the best location of cameras used to image droplets in the flow depends heavily on the scattering properties of the seeding droplets and the properties of the cameras. The cameras used were monochrome type IDT 1400de, featuring a resolution of 1360 X 1036 pixels (1.4 megapixel). The pixel size on each detector was 4.7 microns. Images were transferred from each camera to a desktop PC via a IEEE 1394 connection, and images were stored on a special data acquisition board until they could be written to a hard drive. Up to five image pairs per second were acquired by each camera. Each camera was equipped with 60 mm Nikon lenses, and the lenses were installed on Scheimpflug mounts. The mounts allowed the detector of the camera to be positioned in three dimensions relative to the lens. This allowed the detector to be positioned in the image plane produced by the lens even when the normal vector of the laser plane and the centerline of the lens were not aligned. This feature was essential for effective imaging of the droplets in the laser plane; without Scheimpflug mounts it is impossible to correctly focus the image on the detector.

Since 5-micron droplets scatter light in a Mie-scattering regime, the local intensity of the scattered light depends heavily on the direction of the incident light and on the scattering direction. Mie-scattering is an extremely complex phenomenon, and will not be discussed in detail here. However, online scattering codes are available, and the scattering behavior of a particular droplet can be readily estimated using this type of tool (Prahl, 2001). The scattering properties of a 5 micron droplet, composed of propylene glycol, and scattering 532 nm light, were investigated. The index of refraction of propylene glycol is 1.43, and the droplet is assumed to be totally transparent. There is therefore assumed to be no imaginary component to the index of refraction. In fact, this is an excellent approximation, since propylene glycol is very nearly transparent, and the imaginary component of the index of refraction is extremely small.

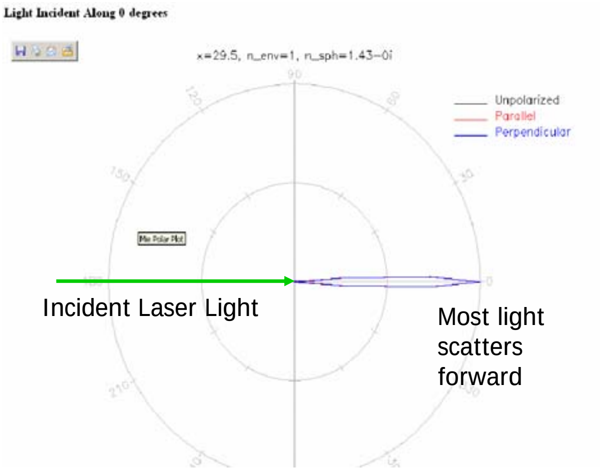

Figure 21. Polar plot of 532 nm light scattered by 5 micron droplet, developed using online application by Prahl (2001)

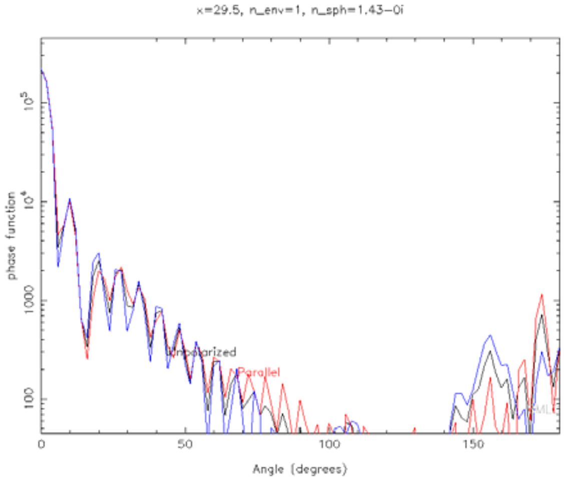

Figure 22. Log plot of scattering intensity, also generated using online tool by Prahl (2001)

The scattering contours of each droplet are shown in Figures 21 and 22. As can be seen from the figures, most of the scattered light is transmitted forward, away from the laser emitter. Local peaks in the scattering intensity occur near 30 degrees from the forward direction (the forward direction is referred to as the 0 degree direction in the figures). It is therefore reasonable to install cameras on either side of the laser sheet, positioned so that this forward-scattered light is imaged effectively. However, the Scheimpflug mounts described above are essential for this type of setup, so that the detector and lens can be positioned in such a way that the image plane is focused correctly on the detector.

3-D PIV depends on analysis of images from two cameras, so that the full three-dimensional data associated with the flow can be obtained. In essence, each camera produces a two-dimensional vector field, and then each set of 2-D vector fields is analyzed in order to reconstruct the full 3-D vector field.

Successful 3-D PIV can be extremely challenging, particularly if the cameras are not set up correctly, or if the algorithm used to obtain the vector fields is not calibrated effectively. Some guidelines have been developed that allow an initial setup to be attempted, and refined iteratively until a successful setup and calibration are obtained, and these guidelines will be covered in the next sections.

5.7.4 Camera Distance from Laser Sheet

In order to provide effective 3-D PIV conditions, the burner was positioned in a region where the laser sheet was approximately 2.5 mm thick.

The distance at which each camera must be positioned from the laser sheet depends on the camera resolution and on the optics used to focus the image. Essentially, the cameras should be positioned far enough from the laser sheet so that each droplet produces a useable image on the detector. Some investigators have recommended that each droplet should produce an image on the detector occupying nine pixels. In the current case, this would have required that an area of the flow no larger than 3 mm on a side be imaged. In fact, this constraint was not found to be necessary; very effective PIV was carried out with an examination region approximately 30 mm on a side. The reason is that that the focal depth of the lens was limited, and the laser sheet thickness was actually somewhat thicker than the focal depth of the lens. Some droplets that were slightly out-of-focus were detected in every exposure, and the images of these slightly out-of-focus droplets were much larger than they would have been if they had been in perfect focus. The signal-to-noise ratio of these images was decreased slightly, but the benefits, in terms of increased examination region, were dramatic. Since the PIV setup had to be validated in any case, it was reasonable to examine the largest region possible, and then check the results obtained for accuracy. A method to validate the setup is described in greater detail below.

5.7.5 Angles Between Cameras and Laser Sheet

The positions of cameras in a forward-scattering arrangement are shown in Figure 23. For 3-D PIV, it is generally best if both cameras lie in exactly the same plane. If they do not, there are ways to calibrate the system to compensate, but the calibration is time-consuming and likely to fail. Once the cameras are positioned in the same plane, they should be arranged as shown in Figure 23. It is not necessary for angle A to equal angle B or angle D to equal angle C. However, for successful 3-D PIV, it is necessary that angles B and C add up to approximately 90 degrees, so that images acquired from each camera contain substantially different viewpoints of the seeded flow. There is considerable room for adjustment; in fact, angles B and C may add

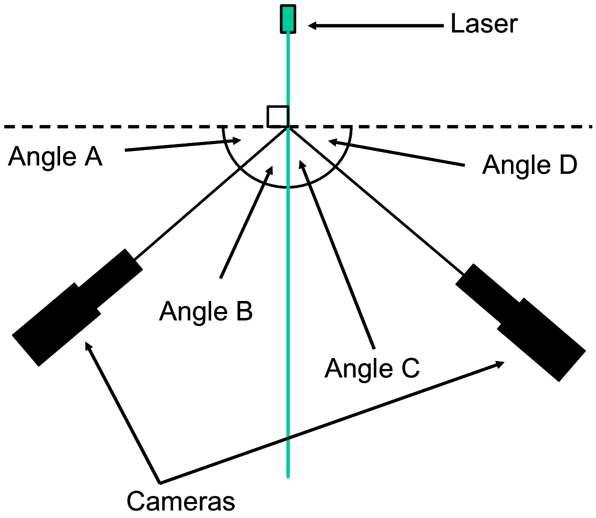

Figure 23. Camera and laser arrangement in a forward-scattering PIV setup

up to as little as 60 or as many as 120 degrees, but setup and calibration are generally easiest if the sum of included angles is nearer to 90 degrees.

5.7.6 Filters and Shutters

When digital cameras are used for PIV, the second image in an image pair is more difficult to acquire than the first. The camera systems are equipped with a buffer system that can store the first image from the detector in approximately 100 nanoseconds. However, the second image must be stored on the detector itself until the first image has been read out from the buffer. This process takes up to 200 microseconds, and is the main limitation on the frequency with which image pairs can be acquired. During the time interval when the second image is held on the detector, the detector remains sensitive to incoming radiation, and overexposure of the image is quite likely. Several measures have been taken to ensure that overexposure of the second image is avoided.

Each camera was equipped with narrow-band-pass filters that allowed only 532 nm light to pass through to the detector. Broad-spectrum sources of radiation still caused overexposure of the second image, however. This was particularly true of luminous reacting flows, like flames, but even overhead lights in a room or sunlight coming in through a window significantly decreased the signal-to-noise ratio in the second image and made PIV impossible.

In order to further improve the signal-to-noise ratio in the second image, the cameras were also equipped with mechanical shutters. The shutters took several microseconds to close, and were controlled by the same timing hub used to trigger the PIV lasers. The shutter began to close as soon as the first laser pulse in a pair of pulses was fired, but, since the closing of the shutter was relatively slow, the second laser pulse fired well before the shutter actually closed. The first image was stored in the buffer, and the second image was stored on the detector, and the shutter closed a few microseconds later. The shutter remained closed for the next few hundred microseconds, as both images were sent to the image acquisition card in the PC. The shutter opened again just before the next laser pulse was fired.

This technique has been found to make PIV possible even in highly-luminous kerosene spray flames, where the background radiation from the flame would ordinarily flood the detector completely during acquisition of the second image (Linck and Gupta, 2003, Gupta et al., 2004).

5.7.7 Calibration

In order for the 3-D PIV technique to be implemented, the entire system must be calibrated. Essentially, the purpose of the calibration is to store constants in the PIV software which relate objects and displacements in the images to locations in physical space. This process is carried out by placing a calibration target with known dimensions in the laser plane. Each PIV system has specific calibration procedures; details of the procedure outlined here apply to systems manufactured by Integrated Design Technologies.

Before the calibration process could be initiated, a seeded flow was introduced into the examination region, and correct laser illumination was provided. At this stage, the level of seeding, laser power, and, most importantly, camera focus, were adjusted. The object was to obtain clear, well-focused images from both cameras, and to focus both cameras on very nearly the same region of the flow. The images should have the highest contrast possible, reflections or other sources of illumination in the image should be absent, and the seeding density should be high enough to make the seeded regions of the flow appear a dark, coarse gray in the image, but not so high that individual droplets cannot be recognized in the image. Regions in the image where no seed is present should appear totally black. Unfortunately, some expertise on the part of the user was required in order to obtain images that would provide effective PIV conditions; and this expertise came only after a long period of experience and experimentation. Many parameters can be adjusted to improve or alter the image quality, including the f-stop setting and focus adjustment on the camera lenses, and the positioning micrometers of the Scheimpflug mounts. Extensive experience was required in order to carry out these adjustments quickly and efficiently.

Once the cameras were correctly positioned, aimed, and focused, calibration target images had to be acquired. For 3-D PIV, with a forward-scattering camera arrangement, the target was placed in the laser plane. The target had to be as thin as possible, so that both sides of the target lay within the focal plane of each camera. Machinist's paper, which has precise graphs aligned on both sides of the page, works well for this purpose. The target surface has to be absolutely flat; if paper is used as the target, it must be supported on a precisely machined frame. The frame should be adjustable, so that the target can be aligned and positioned freely.

In the present investigations, the target was supported on a frame cut from aluminum jig plate. Jig plate is machined to extremely tight tolerances and thus provides a very flat, stable support. The paper was stretched tightly on the frame, and the frame was set on the burner. Since the burner could be positioned in three dimensions with great precision, it was possible to align the target with the laser plane to within 100 microns.

The laser was then shut off, and the target had to be illuminated on both sides, so that both cameras acquired calibration images simultaneously. It was important that a bright, broad-spectrum source of illumination be used, since enough radiation had to be emitted at 532 nm to allow the cameras' detectors to image the target even when the narrow-band-pass filters were in place. The software was then used to acquire and store the calibration image for a particular setup. IDT provided two calibration types, referred to as generic and distorted calibrations. In theory, the distorted calibration approach can be used to calibrate the system if the cameras do not lie in the same plane. In practice, however, the distorted calibration rarely gave good, reliable results; a bias was often introduced, which affected the calculated velocities when a PIV experiment was attempted. It was generally much easier to place both cameras in the same plane, focus them on the same part of the target (albeit on opposite sides), and use the generic calibration. The target must have identical features on both sides, and should have vertical and horizontal lines, at precisely-known intervals. The cameras were aligned correctly when the vertical lines on the target were also perfectly vertical in the image from each camera. If this condition is not met, or cannot be met, a distorted calibration must be attempted.

Since the distorted calibration was not used in these investigations, it will not be discussed further here. In order to complete the generic calibration, a calibration panel was opened in the software, and relevant parameters were entered. A colored grid was generated by the software, and was positioned by the investigator over the same target features in the target images from each camera (see Figure 24). The camera focal length and grid feature sizes were entered, as was the target thickness (which, in this case, was

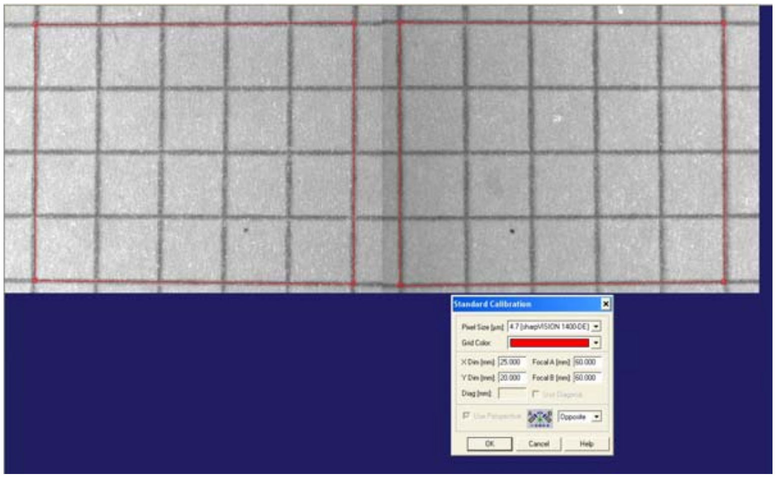

Pixel Size [µm] 4.7 [sharpVISION 1400 DE]

X Dim [mm] 25.000

Focal A [mm] 60.000

Y Dim [mm] 20.000

Focal B [mm] 60.000

Diag [mm]

Opposite

Figure 24. Calibration images for 3-D PIV, showing image of target acquired by each camera and calibration field

specified as 0 mm) and the camera arrangement (cameras on opposite sides of the laser plane). The software stored the relevant parameters and generated a set of calibration constants. For the current setup, this calibration and its associated information then had to be loaded for each PIV session. If the setup was changed in any way, for example if a camera was bumped out of position, the system had to be recalibrated. The process of calibration could take minutes if carried out correctly, or months if attempted by an inexperienced investigator without adequate technical support.

5.7.8 Image Acquisition

PIV images are acquired in sessions, and sessions of 20 or more image sets, containing image pairs from both cameras, are necessary to obtain accurate, well-converged average values of velocities in a particular flow. Each session must be associated with a calibration in order for 3-D flowfields to be obtained. Due to the number of images, and the size of each image, considerable memory is required to acquire and process a session, and considerable hard disk space is necessary to store the images from each session. If 200 image sets are obtained in a particular session, that session will occupy approximately 1.3 gigabytes of hard drive space.

Assuming that good image sets have been obtained, the first step toward generating a 3-D vector field is to examine the image pairs from each camera to obtain 2-D vector fields. In order to carry out this process, a mesh is laid over the image. The mesh is attuned to the calibration parameters associated with the session, and will appear to exist in the image plane. The number of nodes and dimensions of the mesh are adjusted until the image is populated with the required number of nodes in any desired arrangement. The algorithm will then divide the image into interrogation regions, with the center of each interrogation region located at one of the nodes in the mesh. This process is carried out for both images in the image pair. A cross-correlation algorithm is then used to calculate the 2-D components of velocity in the interrogation region.

5.7.9 2-D and 3-D Particle Image Velocimetry

The cross-correlation algorithm used here is one of several types of algorithm developed for particle image velocimetry. Auto-correlation algorithms, which can be applied to images where both laser pulses are captures in the same image, as opposed to successive images, are also common. However, cross-correlation algorithms are useful, because there is no directional uncertainty. It is always clear in which direction the flow is moving in a particular interrogation region (Raffel, et al, 1998).

One process by which a cross-correlation algorithm may be implemented is shown in Figure 25. The figure shows the implementation of a cross-correlation algorithm employed by Vincont, et. al., (2000). The image is divided into interrogation regions, and the interrogation regions from the second image are positioned at a variety of locations over the same regions in the first image. The total brightness of the resulting overlaid image will be greatest when the second image has been shifted in such a way that the droplet images in the first and second images match up. This is referred to as the peak value in the correlation, and the displacement in pixels necessary to obtain this peak provides the spatial displacement, in two dimensions, of the fluid in the given region between the first and second laser pulses. The precision of this technique can be increased by use of a Gaussian sub-pixel interpolation. Since the images have to be shifted relative to each other in increments of pixels, the precision of the technique would normally be limited, since the local displacement could only be obtained in whole-pixel increments. However, if a Gaussian curve is fitted to the distribution of correlation values on either side of the peak correlation, a good estimate of the true local displacement can be obtained (Raffel, 1998).

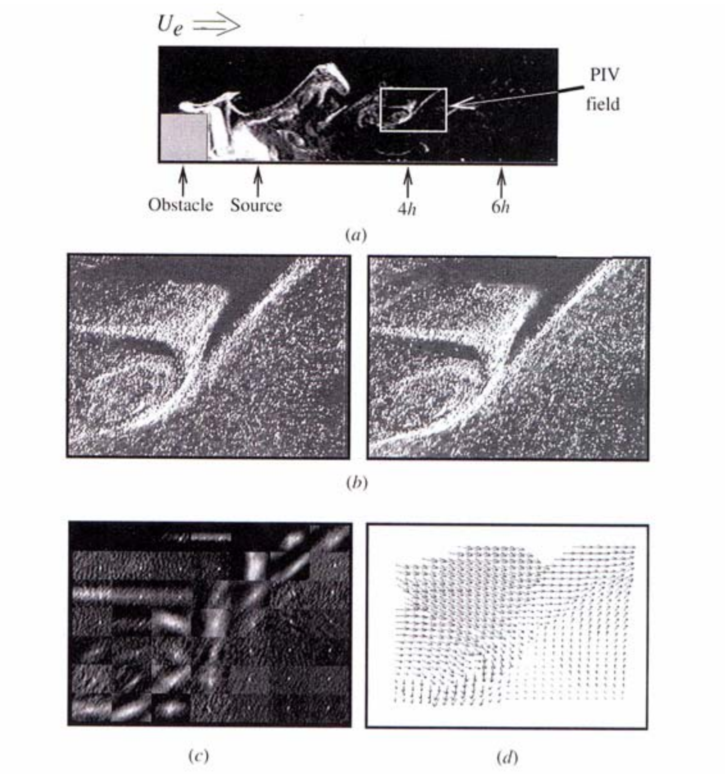

Figure 25. Implementation of image-shifting cross-correlation algorithm by Vincont, et al. (2000). a) Original image b) Image pair in examination region c) Local correlation values in interrogation regions d) 2-D vector field

Once 2-D vector fields have been obtained for each image pair from each camera, the 2-D fields can be combined into a 3-D vector field using the same principles of parallax vision employed by the human eye. Essentially, if one were to see an arrow, hanging in space, from two different angles, one would be able to describe with ease the

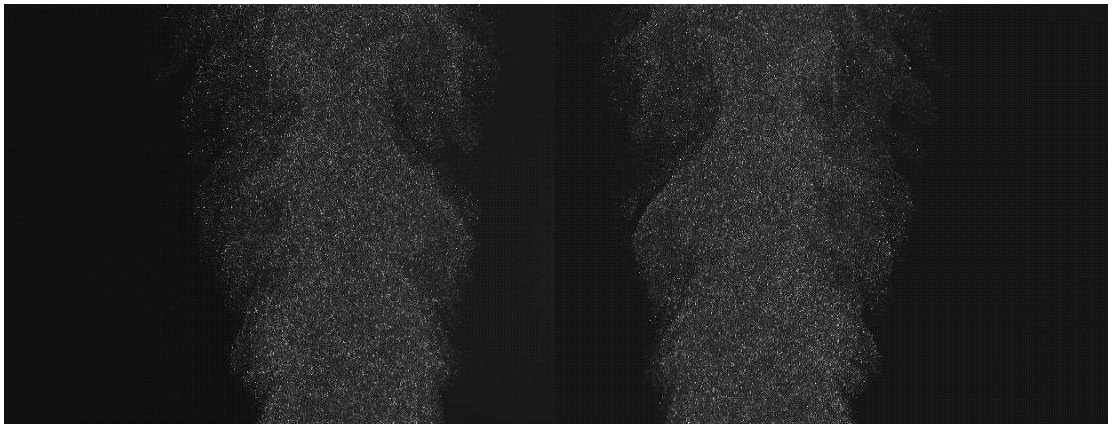

Figure 26. Initial 3-D PIV image set, showing image pairs from both cameras

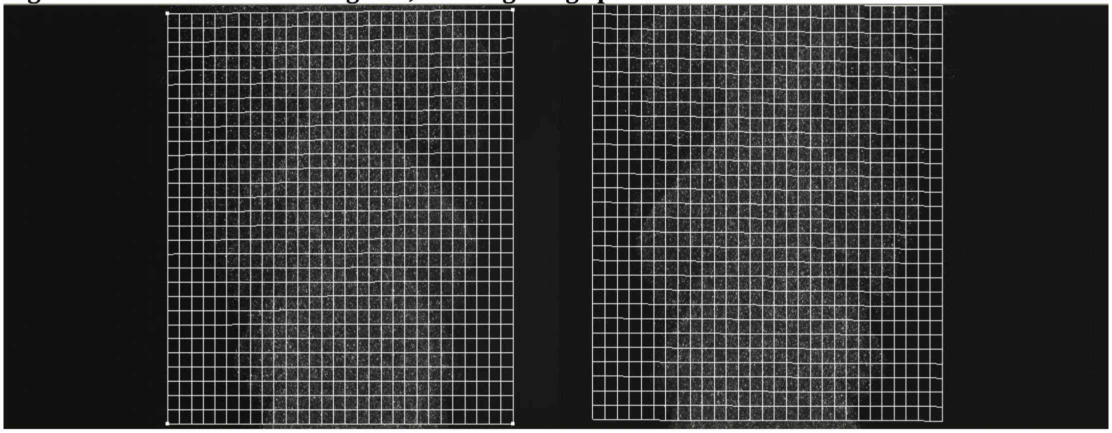

Figure 27. A mesh is laid over the image

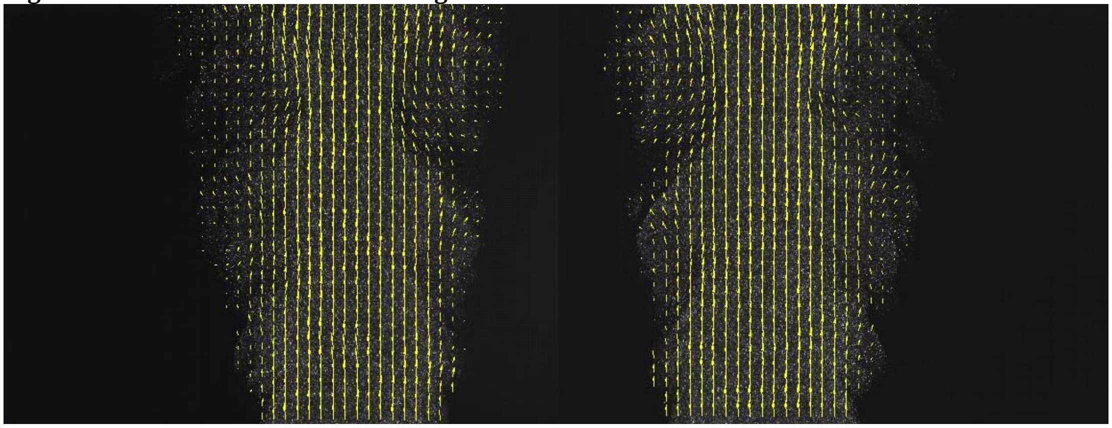

Figure 28. 2-D vector fields are obtained, with one vector located at each mesh node

magnitude, location, and direction of the arrow. The same principle is applied by the 3-D algorithm developed by IDT. The process by which vector fields are generated is shown in Figures 26 – 30. A vertically-oriented seeded turbulent air jet, with a Reynolds number of $6.9*10^3$, is shown. The jet is shown emerging into stagnant, unseeded air. As is shown in the figures, a mesh is laid over the images. The 2-D stage of the algorithm develops vector fields in each image. The combined 3-D vector field, developed from the 2-D fields, is exported into a Tecplot^{TM} application, and displayed. Vectors in the 3-D flowfield are color-coded according to the magnitude of their out-of-plane velocity component. In a radial geometry, this out-of-plane velocity represents the tangential or rotational component of the velocity. If vector values from multiple image sets are averaged, then contours of mean velocity of the jet can be obtained, as shown in Figure 30.

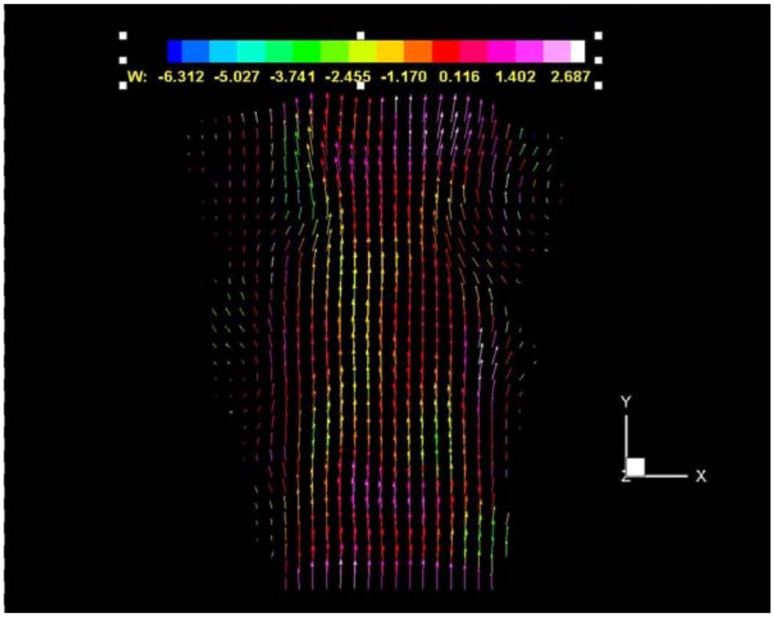

Figure 29. Three-dimensional vector field

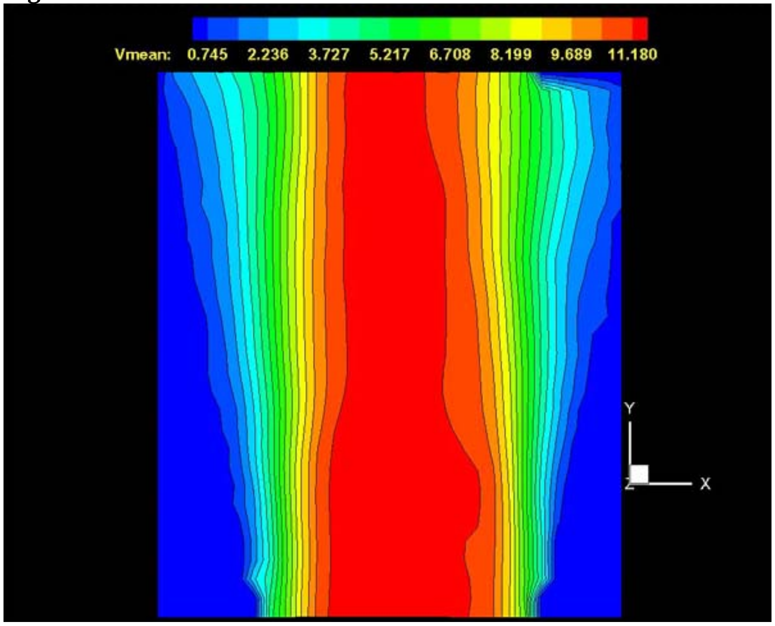

Figure 30. Mean axial velocity contours, developed from multiple vector fields

Unfortunately, the details of the IDT algorithm are quite confidential. No information is available from the manufacturer about the process by which 2-D and 3-D vector fields are obtained. It is also impossible to obtain the correlation values or correlation value distributions for individual interrogation regions. The software is essentially a black box; images are fed in, and vector fields are obtained, but the investigator is not able to monitor the action of the algorithm in any detail.

The IDT algorithm probably does not incorporate an image-shifting technique of the type employed by Vincont, et al. (2000). Image-shifting algorithms tend to run quite slowly, even on powerful computers. It is more likely that each interrogation region is converted into a Fourier transform, and that the correlation for the interrogation region is obtained on the basis of these transforms. Algorithms of this type can run much more rapidly, and the performance of the IDT algorithm indicates that this type of technique may be in use.

5.7.10 PIV Algorithm Validation Using Turbulent Jets

Given the uncertainties associated with the algorithm, a method must be employed to validate the PIV results. One approach is to translate the calibration target by known increments across the examination region, obtain images at a series of locations, and then implement the PIV algorithm. For each image set, the algorithm should obtain the correct values of target displacement. This approach is not entirely satisfactory, however, because images of a well-defined target that is illuminated from each side are fundamentally different from droplet images generated by laser-sheet illumination. Contrast and brightness levels will be different, and the chaotic and unpredictable qualities of a turbulent flow are also missing.

To validate the results obtained by the PIV algorithm, specialized hardware was developed that allowed a precisely-controlled, seeded, turbulent air jet to be projected across the laser plane. The jet projector was machined out of a solid block of plastic, and featured angled receptor ports, each cut at a known jet angle θ_{jet}. A plastic tube could be fitted into each port (see Figure 31). The angle of projection of the tube depended on the port into which the tube was inserted. Depending on the port used, the jet could cross the laser plane at angles of 0, 30, 45, 60 and 90 degrees from the vertical direction. The projector block fit tightly into the swirler hardware developed for the burner, and the angle and position of the jet could thus be controlled with great precision. The flowrate and level of seeding of the jet were adjusted by changing the number of active atomization jets and the feed pressure of the atomizer.

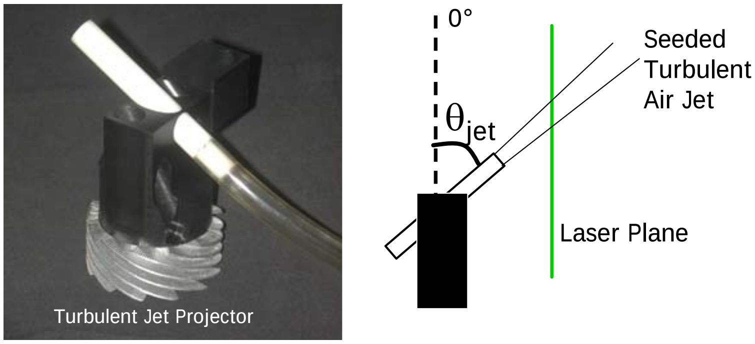

Figure 31. 3-D PIV setup validation using turbulent jets

The PIV results could then be validated by comparing the jet velocity components provided by the technique with those known to be associated with the jet. The calculated jet angle is of particular importance; if there is any bias or inaccuracy in the calibration, the calculated jet angle will not compare well with the known jet angle. For each angle, average velocity values were developed on the basis of 50 image sets. When the PIV conditions were correct, the velocity contours converged quickly to their average values, and general convergence was observed even if averages were developed on the basis of as little as 20 image sets. Thus, average values based on 50 image pairs give good results to within less than one percent. There is very little observable difference between average values calculated on the basis of 49 image sets and 50 image sets. For the actual experiments described in the results presented below, 200 image sets were obtained for each experiment. The result of the turbulent-jet validation shows that the 3-D PIV technique is extremely effective, and provides the correct velocities and jet characteristics. The data obtained during validation will also be discussed in more detail in the results section below.

6. Results

6.1 Overview of Results

6.1.1 Unenclosed Experiments

Several questions were considered in the course of the present investigation, and results presented here will address each of them in turn. First, the accuracy of data obtained from 3-D PIV will be discussed. Data obtained to validate the setup and calibration process will be presented. Then, the flowfield and swirl number of combustion air from individual swirlers is described, using the 3-D PIV technique. Air was fed through each swirler at two flowrates resulting in two Reynolds number conditions. This step was necessary, so that the swirl condition of air from each swirler in subsequent experiments could be specified and discussed.

Flames obtained at one air flow Reynolds number condition, and a single fuel flowrate (and resultant thermal load), are then discussed. Twelve cases, involving different swirl conditions in each case, were examined, so that the effect of swirl condition on flame structure can be described. A particular swirl condition, which produced the most compact flame region, was identified. This swirl condition, featuring the 45-i and Null-o swirlers, was then examined in further detail. This swirl configuration will be referred to as the 45-i/Null-o configuration in the rest of this document.

The features of the nonreacting air flow field in the combustor, and the structure of the flame, are of particular interest (Linck, 2006). It has been shown that the structure of the nonreacting airflow closely resembles that of the flame, and that important aspects of the flame structure can be examined and analyzed on the basis of the nonreacting airflow. However, the effect of a central atomization air jet, emanating from the fuel nozzle, on the air flow field has not previously been examined. Therefore, results will be presented below which identify the effect of this jet on the swirling airflow field in the 45-i/Null-o configuration. Two Reynolds number conditions were considered. The airflow field was then compared with the structure of the associated flame, and a clear connection was established.

The effect of thermal load on flame structure was also examined. Two thermal loads and two Reynolds number conditions were examined, again using the 45-i/Null-o configuration.

The effect of airflow distribution on the structure of the 45-i/Null-o flame was then considered. Three cases were compared, in which the same overall air flowrate was maintained, but in which the proportion of air fed through the inner and outer swirlers was varied.

The atomization of the fuel spray associated with several experimental conditions was examined and characterized, so that the effectiveness of the atomization at a variety of operating conditions could be understood. The PDPA technique was used to characterize the fuel spray at two thermal loads, and to examine the relationship between the fuel spray properties and the atomization air flowrate at a single fuel flowrate.

6.1.2 Enclosed Experiments

The exhaust jet produced by a reacting flow was also examined. In order to carry out this portion of the experiment, the combustor enclosure was installed, and information obtained about the structure and behavior of unconfined flames was used to create a flame in the combustor. Initially, the flame was examined under enclosed conditions near atmospheric pressure. Later, the flame was examined under enclosed and pressurized conditions. The features of the enclosed flame, obtained at atmospheric pressure, with the mixing chamber and exhaust nozzle removed, closely resembled the features of the corresponding unenclosed flame, and the exhaust temperature produced by the flame at two power settings was measured. This was done so that an estimate of the exhaust jet temperature could be obtained for other enclosed cases.

Results obtained under enclosed and pressurized conditions are then presented. The combustor enclosure was installed, and the mixing chamber attached. The 45-i/Null-o swirl configuration was installed in the injector to the combustor, and the mixing chamber filled with water. Nonreacting airflows, without fuel, were fed into the combustor, and the features of the exhaust jet were examined. Optical examinations of the exhaust jet behavior were carried out. Two combustor pressure conditions were initially examined. In the first case, the combustor pressure was 1 psig (1.07 bar total pressure). In the second case, the total combustor pressure was 2.02 bar, which produced a choked jet in the exhaust nozzle. All three available exhaust nozzles were examined at the lower combustor pressure. Only the Conical Projecting Nozzle (CPN) and the Corrugated Converging-Diverging Nozzle (CCDN) were examined at the higher pressure. Only the CPN and CCDN nozzles could be observed at the higher combustor pressure; the Flush-Mounted Nozzle (FMN) produced conditions in the mixing chamber under which the jet could not be observed directly, due to the presence of recirculating bubbles. Certain features of the interaction, which indicate unique mechanisms of instability in the two-phase flow, were observed, and will be discussed in greater depth in the sections below.

A pressurized flame was then created, and the exhaust jet forced through the exhaust nozzle and into the mixing chamber. The effect of combustion in the combustor on the features of the exhaust jet, emanating from the CPN and CCDN, was examined.

Sound spectrum analysis was also applied to several cases of interest. The effect of combustor pressure, exhaust nozzle geometry and combustion on the sound spectrum associated with the system is presented below.

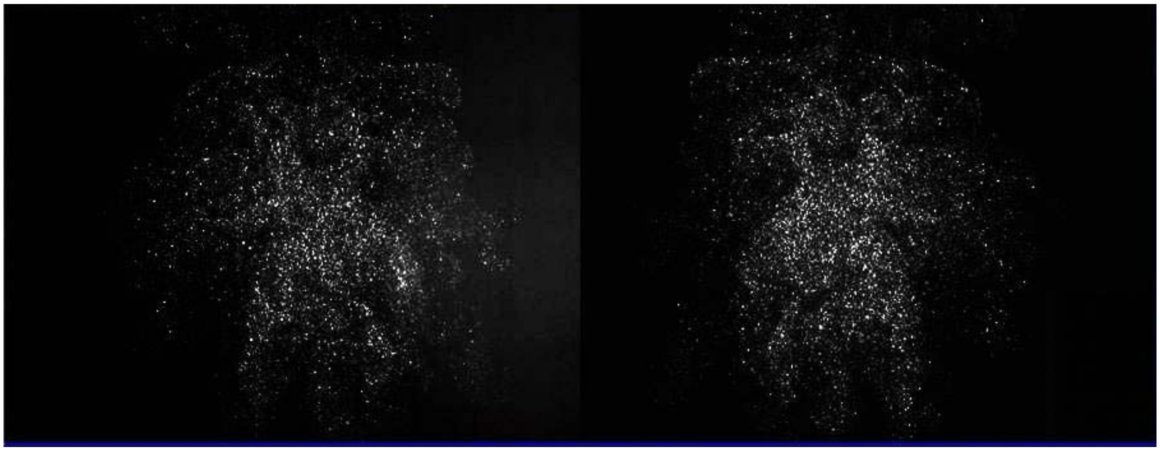

Figure 32. Sample image set, showing turbulent jet crossing laser plane at 45 degree angle

6.2 Validation of PIV Setup

As discussed above, a special apparatus was developed in order to project a turbulent, seeded air jet across the laser plane at a series of known angles. Two cameras were used to image the illuminated droplets, and 50 image sets, comprised of image pairs recorded by each camera, were obtained for each test. The initial average velocity of the jet was 11 m/s, and the initial diameter was 9.53 mm, producing a Reynolds number of $6.9*10^3$. A sample image set, obtained with the jet at an angle of 45 degrees from the laser plane, is shown in Figure 32. The velocities of greatest interest are the local mean axial and local mean tangential (out of plane) velocities. These are referred to in the figures as *Vmean* and *Wmean*. Contours of *Vmean* and *Wmean* associated with the 45 degree jet are shown in Figure 33. The calculated jet angle is 44.8 degrees. Other jet angles were also investigated. Jets oriented at angles of 0, 30, 60 and 90 degrees were found to have calculated jet angles of 0.2, 61.7, and 89.6 degrees. The magnitudes of the velocities were consistent with the known velocity of the jet. It is thus shown that the data obtained by the 3-D PIV setup used in this set of experiments provided valid results. Even a jet oriented at a right angle to the laser plane was characterized effectively. The same setup and calibration were used for all subsequent PIV investigations.

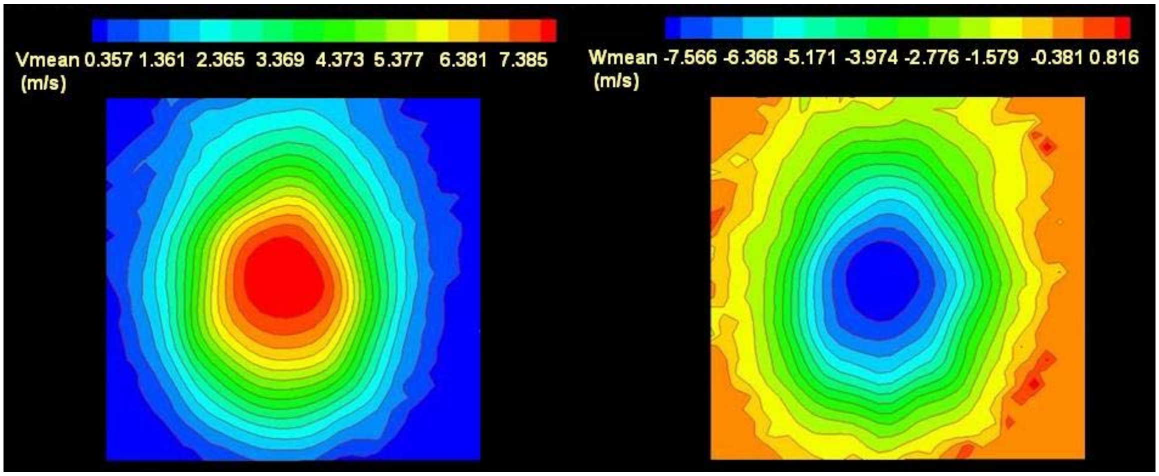

Figure 33. Average contours of axial and tangential mean velocity; turbulent jet crossing laser plane at 45 degree angle

6.3 Swirl Number Calculations

In order to compare this research with that of others in the field, it was necessary to measure the swirl condition associated with the flow from each individual swirler. More complex flows, in which air issued from both inner and outer swirlers, as well as the atomization nozzle, will be described in another section below. The swirl number is calculated using the simplified expression given in equation (5). This expression makes use of only the axial and tangential mean velocities. However, the tangential velocity in the flow can only be measured effectively via 3-D PIV, so all three components of velocity were obtained experimentally, and the axial and tangential mean velocities were integrated across the flow.

Two Reynolds number conditions were examined. The Reynolds number of the flow through each swirler depended on the volumetric flowrate of the air moving through the swirler. In fact, only the mass flowrates of air were measured directly, due to the metering systems used. Since all the experiments were conducted at atmospheric pressure, the volumetric flowrate was calculated on the basis of the temperature and pressure conditions in each case.

For the first Reynolds number condition (Reynolds Number Condition 1), 5.47 g/s of air were fed through each swirler. For the second Reynolds number condition (Reynolds Number Condition 2), 9.3 g/s of air were fed through each swirler. The Reynolds number of interest is the one occurring at the swirler inlet. The relevant length scale in the calculation was δ, where δ was the width of the annulus. The Reynolds number, *Re*, at the swirler inlet was calculated using the mean axial velocity, density, characteristic length and dynamic viscosity of the flow.

$$Re = \frac{V * \rho * \delta}{\mu} \qquad (16)$$

In the combustor, δ_i and δ_o were the width of the inner and outer annuli, respectively. The resulting swirler inlet Reynolds numbers in Reynolds Number Condition 1 were found to be $3.2*10^3$ and $1.8*10^3$ in the inner and outer swirlers, respectively. The Reynolds number of the outer swirler was smaller, since the cross-sectional area of the outer swirler was larger than that of the inner swirler.

Reynolds Number Condition 2 featured 9.3 g/s of air passing through each swirler. The Reynolds numbers of the flows were $5.5*10^3$ and $3.1*10^3$, respectively. The relevant parameters of these experimental conditions are given in Table 2.

Reynolds Number Condition	***Condition 1***	***Condition 2***
Inner Annulus Mass Flowrate	5.47 g/s	9.3 g/s
Inner Annulus Average Velocity	4.8 m/s	8.1 m/s
Inner Annulus Volumetric Flowrate at 1 bar, 21 °C	4.5 L/s	7.7 L/s
Inner Annulus Reynolds numbers	$Re_{i1} = 3.23*10^3$	$Re_{i2} = 5.5*10^3$
Outer Annulus Mass Flowrate	5.47 g/s	9.3 g/s
Outer Annulus Average Velocity	2.7 m/s	4.6 m/s
Outer Annulus Volumetric Flowrate at 1 bar, 21 °C	4.5 L/s	7.7 L/s
Outer Annulus Reynolds numbers	$Re_{o1} = 1.8*10^3$	$Re_{o2} = 3.1*10^3$

Table 2. Parameters of Reynolds Number Conditions

The actual Reynolds number of each flow varied somewhat from experiment to experiment, due to the presence of seeding air. The flowrate of seeding air necessary to obtain good PIV data varied from case to case, and had to be adjusted. Fortunately, the flowrate of seeding air added could be calculated based on the number of seeder jets, and the seeder inlet pressure used in each experiment. It was found that the seeding air necessary to provide good PIV conditions comprised an additional 5-7% of the main air stream fed into each annulus through the measuring orifices. As will become clear, this is too small an amount to significantly alter the features of the flow. The corrected Reynolds number, which includes the seeding air stream, associated with each case will be noted in the figures in which relevant data is presented.

The general features of the swirling airflow are well represented by the mean axial velocity contours shown in Figure 34. The figure shows the axial velocity contours of the swirling flow emerging from the 45-i swirler, at Reynolds Number Conditions 1 and 2. The contours represent averages, obtained from 200 image sets, and the examination region in this case extends between 8 mm and 36 mm from the burner centerline. The location of the examination region was set in order to optimize observation of the swirling flow. A region from 1 mm to 22 mm above the burner exit plane was examined. The flows were nearly identical; only the color scales of the figures changed dramatically from one Reynolds number condition to the other. The flowrate was nearly doubled, and yet all the major features were quite similar. The slight differences in contours caused by the change in Reynolds number were due to changes in the thickness of boundary layers within the swirler.

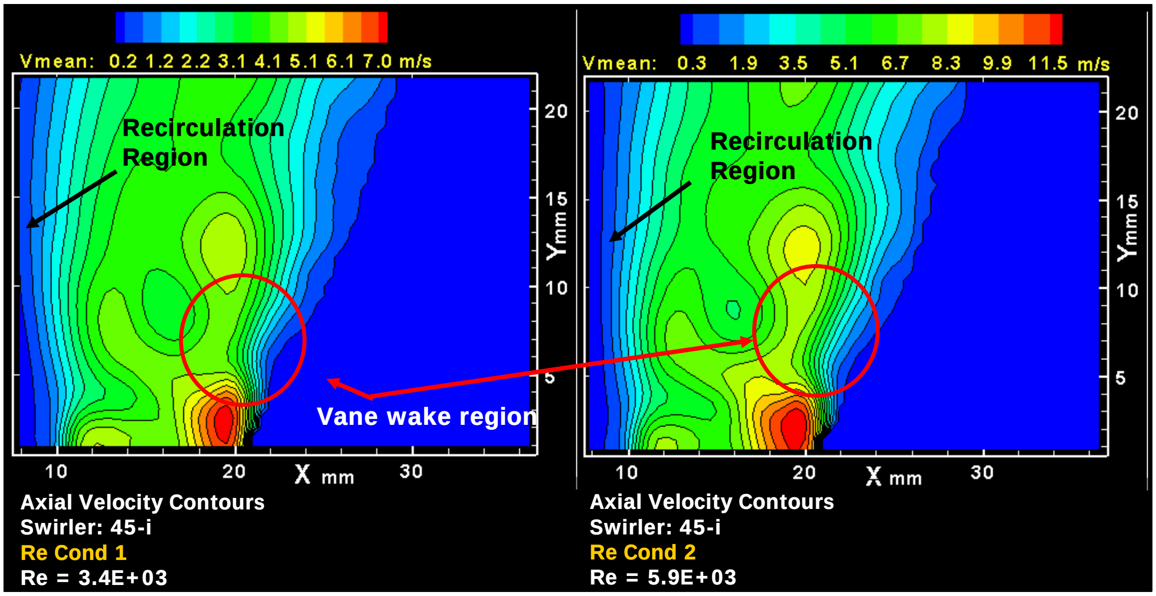

Figure 34. Mean axial velocity contours of flow emerging from 45-i swirler at two Reynolds number conditions

In Figure 34, regions of high axial velocity were observed near the swirler exit plane. The distribution of axial velocity was uneven, indicating that this flow was actually composed of a series of distinct jets, emanating from the vane spaces of the swirler. The adjacent jets were separated by wake regions, where the mean velocity was low. These wake regions occurred where a vane divided the flow, and were mixed away as the adjacent jets merged into a single rotating flow. A recirculation region was observed near the center of the flow, as would be expected in this case. The boundary of this internal recirculation region was nearly vertical.

The similarity in flow structure between flows at different Reynolds conditions is further demonstrated in Figure 35. The figure shows a comparison of mean velocity contours of all three components of velocity. Axial (*Vmean*), radial (*Umean*), and tangential (*Wmean*) mean velocity contours are seen to be largely unaffected by changes in the flowrate.

The structure of the flow produced by other swirlers was also unaffected by Reynolds number, as shown in Figure 36. In this figure, mean axial velocity contours, at both Reynolds number conditions, of the flow from the 60-i swirler are compared. Again, the increase in flowrate made very little difference. The structure of the flow depended primarily on the swirler geometry. The recirculation region of this flow was larger than was the case with the 45-i swirler, as one would expect, given the increase in swirl. Again, the flow was composed of a series of swirling, merging jets, emanating from the

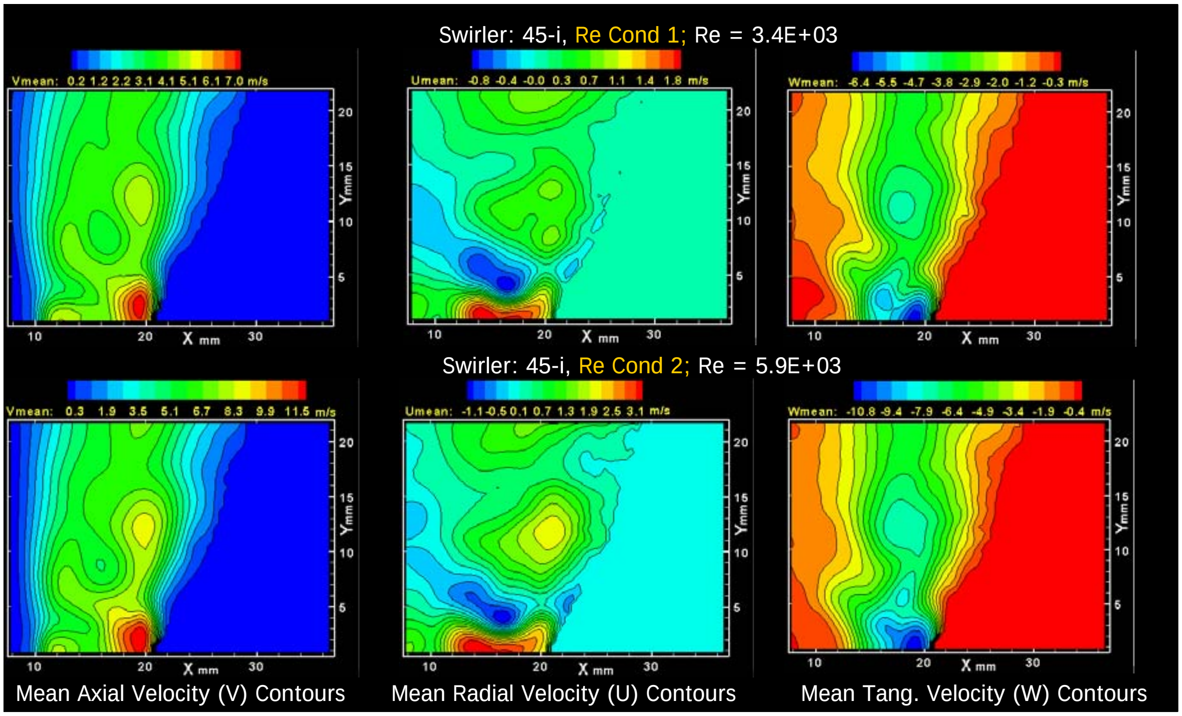

Figure 35. Mean axial, radial, and tangential, velocity contours of flow emerging from 45-i swirler a Reynolds number conditions one and 2

swirl assembly.

Since the structure of the swirling flow was apparently insensitive to Reynolds number, the effect of swirl angle on the flow structure was examined at a single Reynolds number condition. Figure 37 shows a comparison of mean axial velocity contours, produced by the 30-i, 45-i, and 60-i swirlers at Reynolds Number Condition 2. The recirculation region was seen to increase dramatically in size as the vane angle of the swirler was increased. This sort of observation is crucial in determining the correct swirl conditions for a swirl-stabilized system.

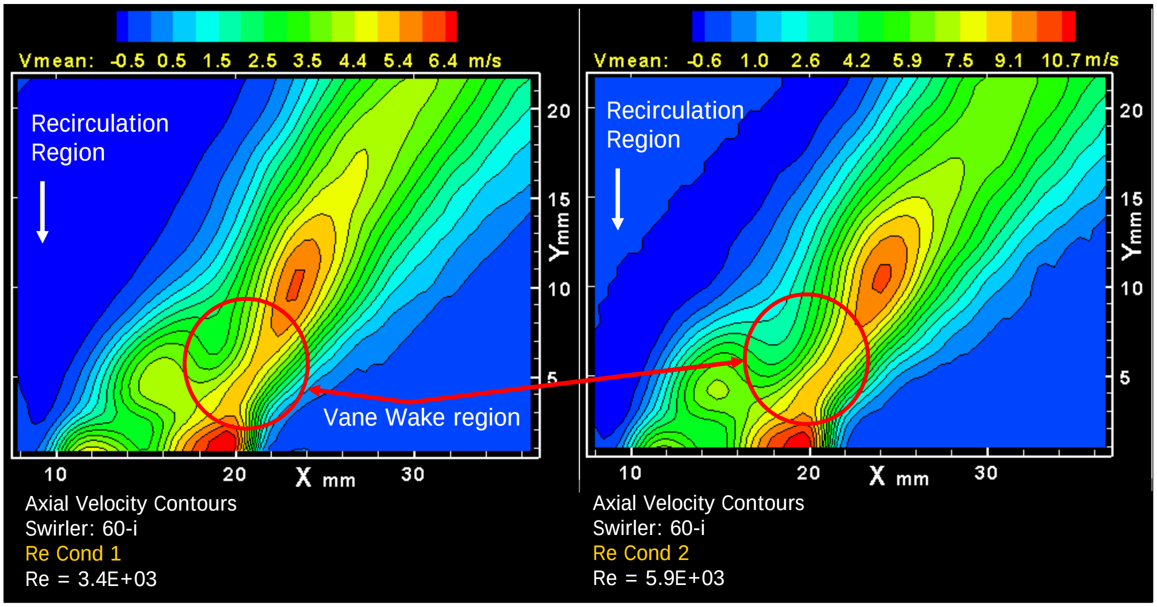

Figure 36. Mean axial velocity contours of flow emerging from 60-i swirler at Reynolds number conditions one and 2

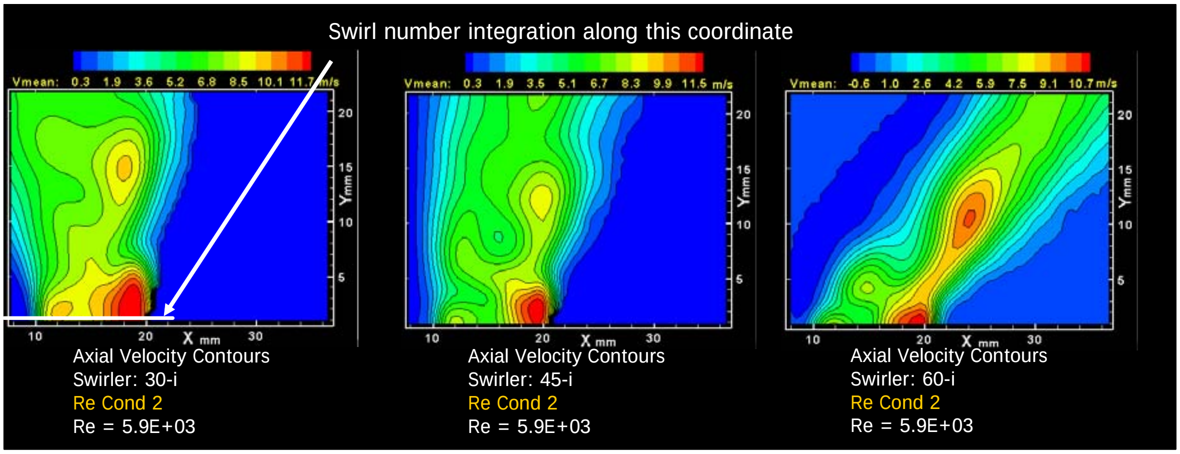

Figure 37. Effect of swirl angle on contours of mean axial velocity, compared at a single flowrate

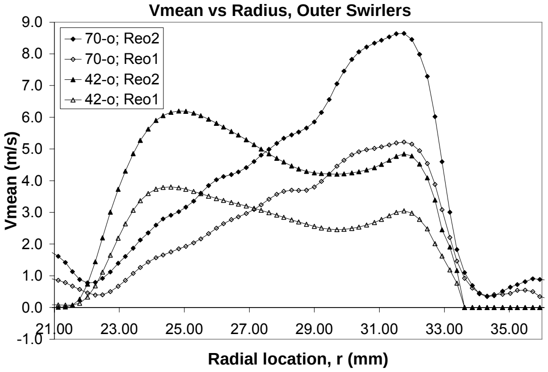

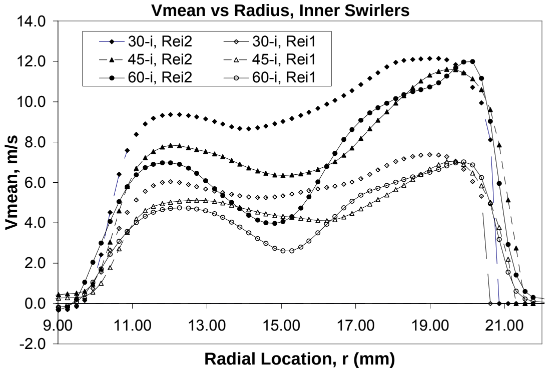

Figure 38. Mean axial velocity curves of flow from outer swirlers, at swirler outlet

Figure 39. Mean axial velocity curves of flow from inner swirlers, at swirler outlet

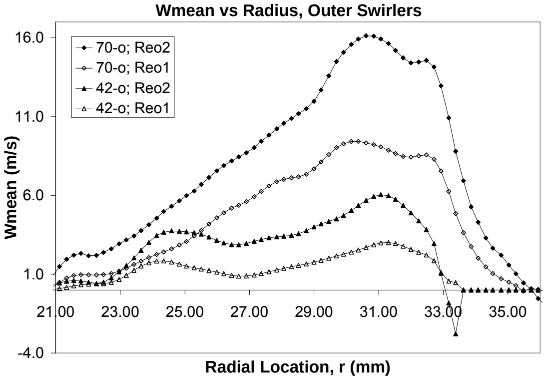

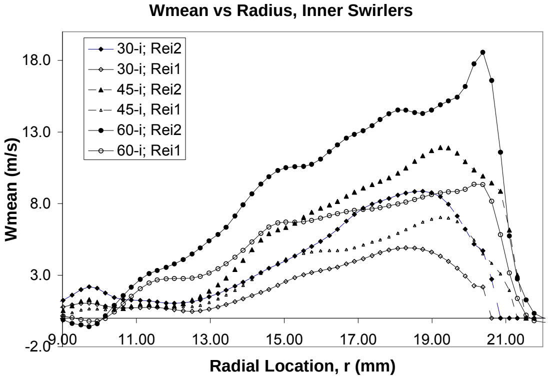

Figure 40. Mean radial velocity curves of flow from outer swirlers, at swirler outlet

Figure 41. Mean radial velocity curves of flow from inner swirlers, at swirler outlet

The same trends were observed for the other swirlers, though detailed data will not be presented here due to time and space constraints. Instead, the focus will now shift to the swirl number calculation. In order to obtain swirl numbers for each swirler geometry at each Reynolds number condition, the axial and tangential velocity components, at an elevation of 1 mm above the swirler outlet, were recorded. Plots of *V*, the mean axial velocity, as a function of *r*, the radial location for all the outer swirlers are presented in Figure 38. The same information for the inner swirlers is shown in Figure 39. Both Reynolds number conditions are represented on each plot. The overall velocities were seen to scale with Reynolds number, so as the flowrate was increased, the values on each curve were increased. However, the shape of the curve did not change significantly with Reynolds number. Only the swirler geometry seems to be important in determining the shape of the curve. This effect is demonstrated further in Appendix C, where plots of the mean axial and tangential velocities are non-dimensionalized by the mean swirler inlet velocity, and the resulting curves plotted.

Plots of tangential velocity, *W*, are presented in Figures 40 and 41. Again, the same trends were observed. Increases in swirl vane angle, at the same air flowrate, produced increases in tangential velocity, and corresponding decreases in axial velocity.

Swirler	***S***	
Outer	$Re = Re_{o1}$	$Re = Re_{o2}$
42-o	0.5	0.6
70-o	1.6	1.7
Inner	$Re = Re_{i1}$	$Re = Re_{i2}$
30-i	0.4	0.4
45-i	0.7	0.8
60-i	1.1	1.2

Table 3. Swirl Numbers from experimental data, swirl angles are from the vertical direction. Reynolds numbers calculated on the basis of combustion air annulus width, air flowrates and physical properties of air, as listed in Table 2.

The data necessary to carry out the swirl number calculation for each curve was now ready. Swirl numbers at both Reynolds conditions for each swirler are presented in Table 3. As is clear from the obtained values, the true swirl numbers were lower than would be predicted by the rough estimate described in Equation (11). Reynolds number was seen to have a small but measurable effect on the swirl number obtained, although, as was noted above, the actual effect of this change on the structure of the flow is very minor. The turbulence-related terms in the complete swirl number expression (Equations (3) and (4)) were omitted from these calculations, as described above in the chapter on background. They are potentially available from the PIV data; however, since the PIV data was acquired using only 200 image sets per session, and since the droplets were too large to fully follow the Kolmogorov scales in the flow, the accuracy of the calculations would be limited. In any case, the local-pressure-related terms in the formal Swirl number equation are still unavailable, so the result would still be approximate, even if the turbulence-related terms were included. The pressure-related and turbulence-related terms also make only a very slight contribution to the overall swirl number calculation. This is demonstrated in detail in Appendix D, where sample turbulence-related terms, calculated from the available PIV data, are shown to be much smaller than the terms related to local mean velocities. The turbulence-related terms are shown to contribute only 2-4% to the value of each integral in Equations (3) and (4), and, since both integrals tend to increase in size simultaneously when the turbulence-related terms are included, the overall swirl number is only very slightly affected. The increase in swirl number, caused by an increase in Reynolds number, is due to changes in the thickness of boundary layers within the swirler, which alter the mean velocity contours.

6.4 Effect of Swirl Configuration on Flame Structure

The swirl configuration in the injector had a very important effect on flame structure, and, due to the complexity of the flows involved, the structure of the flame could not be predicted a priori, but had, instead, to be examined directly. In order to identify flow conditions with features desirable in a submerged combustion system, the full array of available flame geometries had to be documented. Accordingly, to investigate the effect of swirl condition on flame structure, twelve swirl configurations were created, at a single atomization air flowrate, Reynolds number condition, and fuel flowrate. The flames associated with each swirl condition were photographed, using a half-second exposure duration and an f-stop setting of 3.8. The flame was not enclosed.

The airflows were set so that Reynolds Number Condition 2 was achieved. No seeding air was present during this set of experiments. The fuel nozzle was supplied with 0.14 g/s of atomizing air, in order to provide effective atomization of 31 ml/min of methanol. Assuming complete combustion, the thermal load of the flame was therefore 8.2 kW.

Swirl conditions were categorized according to the inner and outer swirler employed. The flames are shown in Figure 42. They are grouped according to the outer

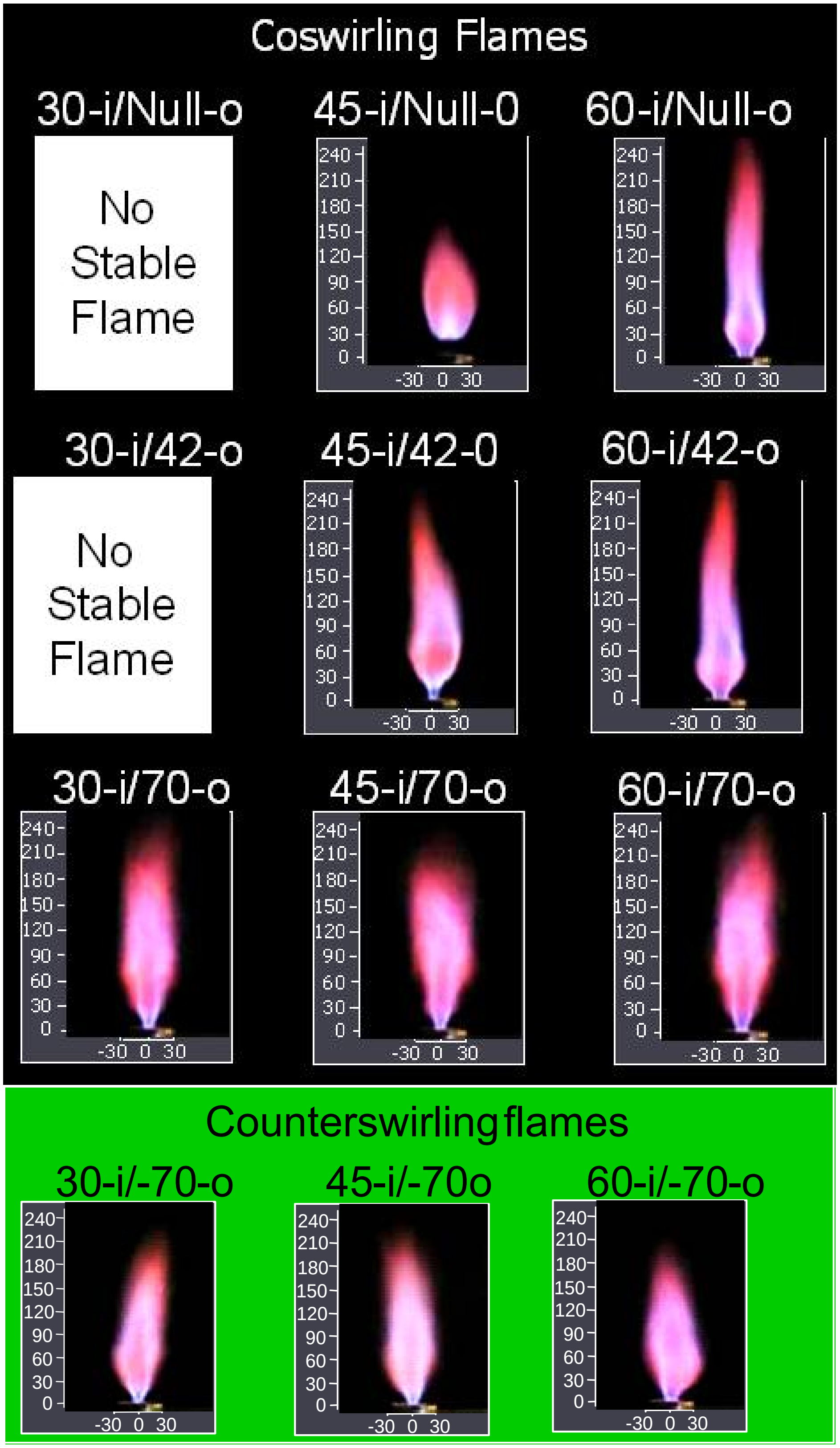

Figure 42. Effect of swirl configuration on spray flames; dimensions are in mm

swirler employed in each configuration. All four outer swirlers were employed. However, of the inner swirlers, only the 30-i, 45-i, and 60-i swirlers were utilized. It was found that, if the Null-i swirler was used, no stable flame could be obtained at all with the combustion air flowrates used here. Even in the case of the 30-i swirler, a flame was stabilized only if used in combination with the 70-o or -70-o swirlers. The combustion air flowrates were selected in order to approximate overall equivalence ratios in gas turbine combustors.

All the flames obtained were between 150 and 240 mm in length. The maximum width of each of the flames was comparable, with each flame displaying a maximum diameter of approximately 40-60 mm.

In the cases where a small outer swirl angle was employed (Null-o or 42-o) the flame geometry depended primarily on the geometry of the inner swirler. In cases where the outer swirl angle was large (70-o or -70-o), the flames obtained with each inner swirler did not vary dramatically in size or shape. The counterswirling flames obtained with the -70-o outer swirler did not vary dramatically from their coswirling counterparts, though the flame region did appear to be slightly shorter. This may indicate that mixing of fuel and oxidizer occurs more rapidly in the counterswirling flames.

In an enclosed, submerged combustor, the flame should be as compact as possible. The most compact flame obtained was achieved by use of the 45-i/Null-o configuration, with combustion terminating 150 mm downstream of the fuel nozzle. This flame was also lifted, with combustion beginning 30 mm downstream of the fuel nozzle. This lifting effect was interesting, since swirl-stabilized flames are not generally lifted (Gupta, et al., 1984). The presence of the atomizing air from the fuel nozzle was an additional factor in this case, and the effect of the atomizing air jet on the flow, in both the nonreacting and reacting cases, had to be investigated further in order for this lifting effect to be explained.

6.5 Effect of the Atomizing Air Jet on Recirculation Zone

The 3-D PIV technique was applied again in order to understand the structure of the 45-i/Null-o flowfield. The PIV technique cannot be applied effectively if a fuel spray is present. The fuel droplets are generally much larger than the seeding droplets, and do not follow the airflow. The PIV images obtained in such a case could provide information on the features of the fuel spray (Linck and Gupta, 2003) but would not allow the flowfield of the gaseous phase to be examined. A fuel spray is inherently necessary for combustion to occur, however, so it was also impossible to examine the gas-phase flowfield of the reacting flow in this combustor with the currently-available technology.

However, the non-reacting airflow field could be conveniently observed. Since the structure of the flame is closely linked to the features of the airflow field, the nonreacting airflow provided important information that assisted in the analysis of the flame structure.

In order to understand the effect of the atomization air from the fuel nozzle on the air flowfield, 200 image sets were obtained, in order to provide well-converged contours of average velocity. A series of observations were carried out using the 45-i/Null-o swirl configuration. The flow was unenclosed. A region of the flow extending from the centerline to a maximum radial distance of 30 mm was examined. Axial locations from 1 mm to 24 mm above the swirler exit plane were examined. Both Reynolds number conditions, and three atomization air flowrate cases, were examined. The Reynolds number conditions have been described previously. The atomization air flowrate in each case is scaled according to the Reynolds number condition, in order to examine whether similar flow structures can be created across a range of Reynolds number conditions, even when a central atomization air jet is present.

In the first atomization air case, (Atom. Air Case 1) the flowrate of atomization air was 0 g/s for both Reynolds number conditions. In the second case (Atom. Air Case 2), the flowrate of atomization air was 0.04 g/s for Reynolds Number Condition 1, and 0.08 g/s for Reynolds Number Condition 2. Similarly, Atom. Air Case 3 provided 0.07 g/s of air for Reynolds number condition 1, and 0.14 g/s of air for Reynolds number condition two. The relationship between the Reynolds number conditions and atomization air cases is clarified in Table 4.

	Reynolds Number Condition	
Atomization Air Case	***Condition 1***	***Condition2***
1	0 g/s	0 g/s
2	0.04 g/s	0.08 g/s
3	0.07 g/s	0.14 g/s

Table 4. Atomization air cases; Reynolds number conditions refer to conditions described in detail in Table 2.

The objective of this approach was to examine scaling; if the effect of the atomization jet on the flowfield can be scaled with Reynolds number, then the flowfield geometry can be controlled simply by controlling the atomization air flowrate, and a uniform flowfield can be established across a range of Reynolds numbers.

So, does it work? The answer is apparent in Figure 43. The figure shows a comparison of axial velocity contours, at both Reynolds number conditions, and using Atomization Air Cases 1 and 2. In Atomization Air Case 1, the recirculation region in both flows extended all the way down to the atomization nozzle. In atomization air case

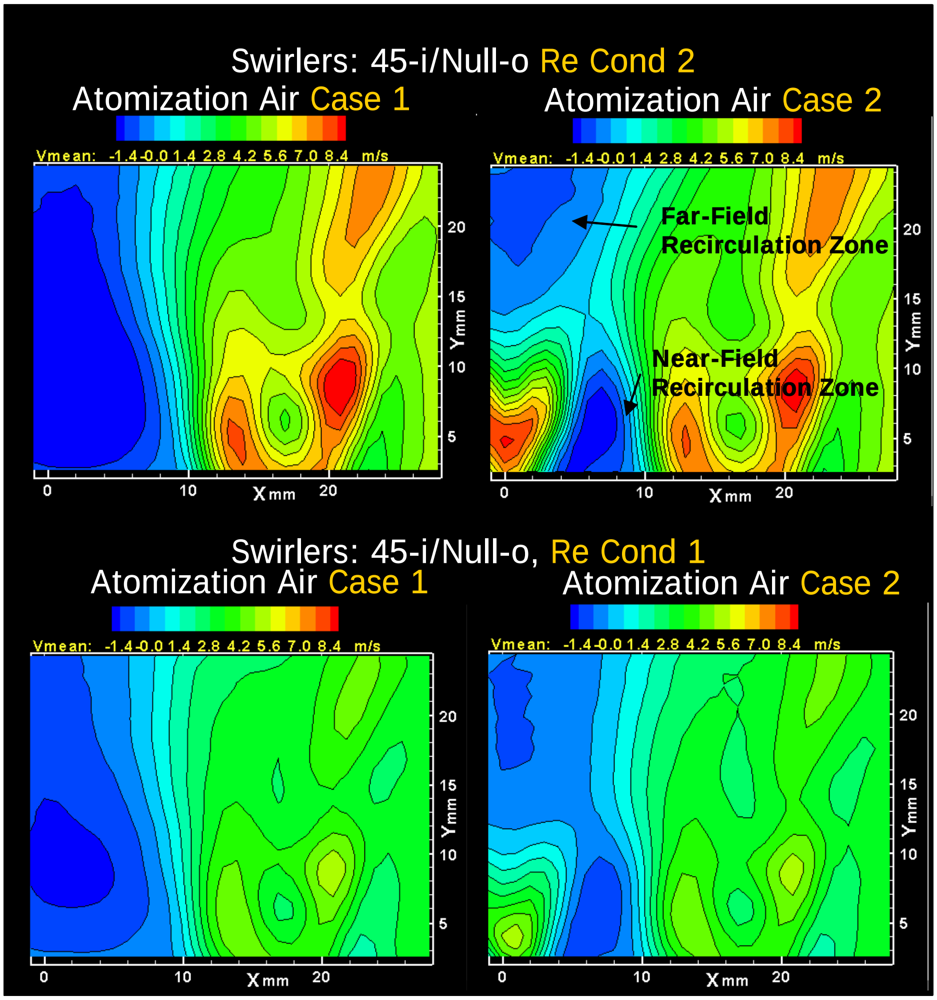

Figure 43. Effect of atomization air jet on air flowfield

2, a scaled atomization airflow was present. This flow emanated from the nozzle at the centerline, and produced the positive axial velocities seen at the centerline and extending 10 mm upward into the flow. For both Reynolds number conditions, the presence of atomization air produced the same effect on the recirculation region. Two separate recirculation regions were produced, one being confined to the region immediately surrounding the fuel nozzle, and one extending further downstream. These will be referred to as the near-field and far-field recirculation regions, respectively.

Given that the effect of the atomization air jet can be scaled with Reynolds number, it made sense to examine all three atomization airflow cases side by side at a single Reynolds number condition. Figure 44 shows comparisons of mean axial velocity contours associated with the three atomization air cases, at Reynolds Number Condition 2. Atomization Air Case 3 produced the most dramatic effect. In this case, the separation between the near-field and far-field recirculation regions was complete. Since this case corresponded to the airflow features used in the flames described above, the lifting effect seen in the 45-i/Null-o flame is clearly explained. The near-field recirculation region did not stabilize combustion. Instead, combustion was stabilized at the boundary of the far-field recirculation region, which also accounts for the geometry of the flame and the lifted flame structure.

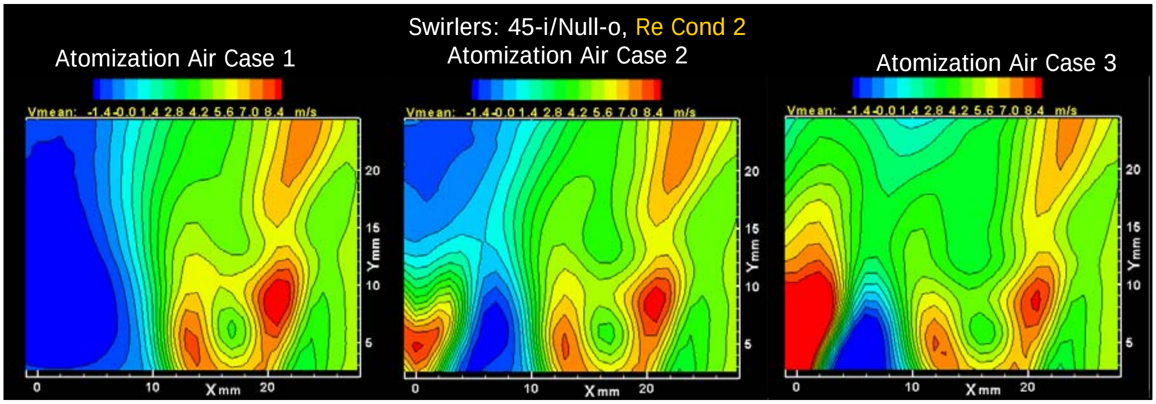

Figure 44. Three atomization air cases, compared at a single Reynolds number condition

The examined region of the flow in each PIV session was limited. This limitation was addressed by carrying out a series of carefully-indexed experiments at increasing vertical elevations above the injector. The observations were carried out in an effort to map out the extent and geometry of the far-field recirculation region. Four PIV sessions were acquired, with each session consisting of 200 image sets. The contours of axial velocity were then mapped, and the data plotted on the same set of coordinates. The resulting contours of mean axial velocity, showing the near-field and far-field recirculation zones in the 45-i/Null-o flow, are shown in Figure 45. Reynolds Number Condition 2 and Atom. Air Case 3 applied, and the features of the nonreacting airflow therefore corresponded to the 8.2 kW, 45-i/Null-o flame shown in Figure 42. The features of the flow, including the recirculation zones, showed an immediate resemblance to the shape of the luminous region of the flame. This correspondence in features is shown more directly in Figure 46, in which the contour plot and the flame are compared directly on either side of the centerline.

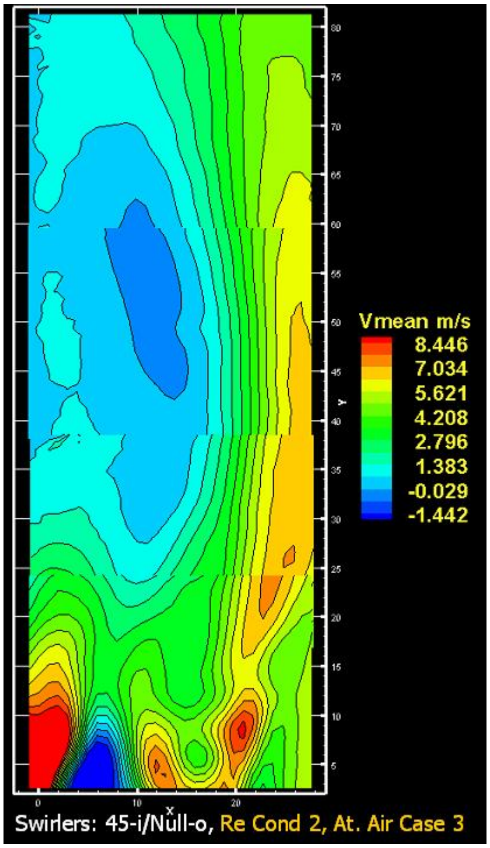

Figure 45. Mean axial velocity contours showing near-field and far-field recirculation zones

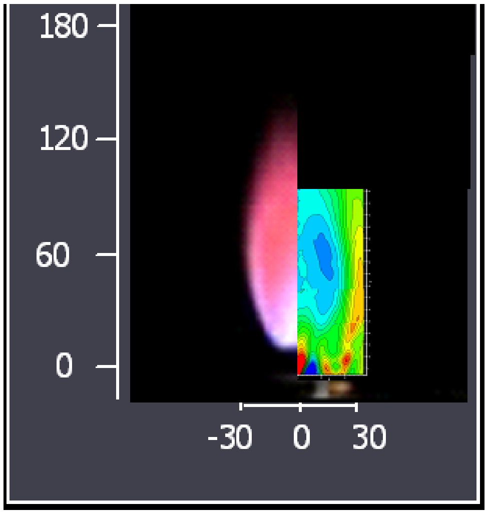

Figure 46. Comparison of axial velocity contours with corresponding 8.2 kW flame

The implications of this observation are significant. It has been known for some time that the features of premixed, swirl-stabilized flames correspond to the features of the flowfield. However, the results shown in Figure 46 indicate that the non-reacting air flowfield can also be used to directly analyze the features of the much more complex liquid-fuelled flames, created using fuel sprays obtained from twin-fluid atomizing nozzles, examined here. Thermal effects, droplet evaporation, and other issues associated with the presence of the fuel spray clearly play only a minor role in shaping the flame. The overall volume of the far-field recirculation zone is somewhat larger in the combusting case, due to heat release, but the shape of the structure is determined by the structure of the air flow. The momentum fluxes of the swirling airflows and atomization air jet are dominant in determining the features of the flow.

6.6 The Effect of Thermal Loading on Flame Geometry

One other factor was found to be extremely important in determining the geometry of the flame. The thermal load of the flame has a significant impact on its size, and the effect of this parameter on the 45-i/Null-o flame was examined. Again, an unconfined experiment was undertaken, and air flowrates set so that Reynolds Number Condition 2 was obtained. Atomization air, matching Atom. Air Case 3, was also used to atomize the fuel stream.

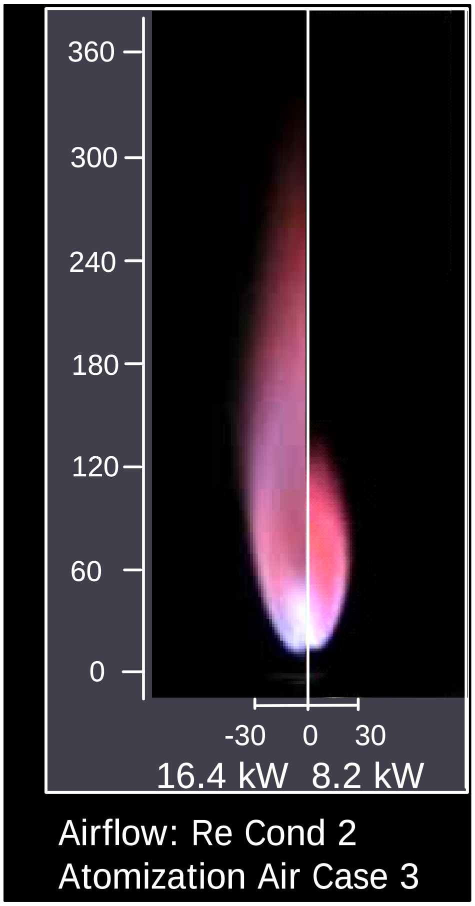

Figure 47. Effect of increased thermal load on flame structure

The flame was then photographed at two different thermal loads. First, the 8.2 kW flame, described above, was imaged. Then, the fuel flowrate was doubled, so that a thermal load of 16.4 kW was achieved. The flame was imaged again. The two flames are shown in a side-by-side comparison in Figure 47, with half of each flame on either side of the centerline. The increased thermal load was seen to double the length of the flame almost exactly. However, other aspects of the flame geometry remained unchanged. The lower edge of the reaction zone remained in the same position at 16.4 kW of thermal loading as at 8.2 kW. The width of the flame did not change appreciably. Essentially, the increased heat release caused the far-field recirculation region to increase in size, due to the increased expansion of gases in this zone. Features of the flame that were not affected by this downstream heat release, such as the liftoff height, were unaffected by the changes in thermal load. It is not clear on the basis of this set of observations whether the relationship between thermal load and flame length is linear for all conditions. It appears unlikely that this would be the case, particularly in a confined flame, where wall

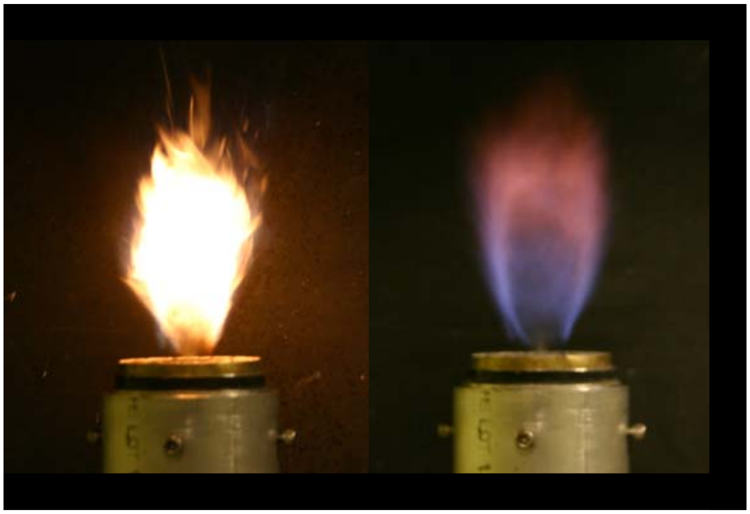

Figure B.3.1 Unconfined kerosene (left) and methanol (right) flames, at equal thermal load (from Linck, et al., August 2004)

Figure B.3.2 Confined kerosene (left) and methanol (right) flames, at equal thermal load (from Linck, et al., August 2004)

interactions would play a role. However, across the range of conditions examined here, the length of the flame does appear to vary linearly with thermal load, at least approximately.

The effect of thermal load on flame structure also appears to be independent of fuel type. Linck, et al. (August, 2004, included in Appendix B) compared the structures of unconfined and confined methanol and kerosene spray flames, in which the flowrates of combustion and atomization air, as well as the thermal load, were equivalent. As can be seen in figure B.3.1, the structure of the unconfined flames was very similar for both fuels. The color of the flames was different, due to soot and soot precursors in the kerosene flame that were not present in the methanol flame, but the location, shape and size of the flames was very similar. This is significant, since the volumetric flowrate of methanol is double that of kerosene for an equivalent thermal load. Confined flames, at atmospheric pressure fired at the same thermal load, are shown in figure B.3.2. Again, the flame structures were quite similar. The confined kerosene flame looks larger in figure B.3.2, but, in fact, the flames were very nearly the same size. In the kerosene flame, luminous particulates caused the flame to be visible in regions of the flow where the methanol flame emits very little radiation, and, as a result the image of the kerosene flame appears larger.

6.7 Flame Scaling

Thus far, two important factors have been identified, which determine, to a great degree, the structure of the reaction zone in the swirl-stabilized spray flame. It is clear at this point that the flame structure is largely controlled by the airflow parameters and thermal load of the flame. Using this approach, it was possible to create a scaled flame, at

Reynolds Number Condition 1, using Atomization Airflow Case 3, with an 8.2 kW thermal load, which had many of the same features of the 16.4 kW flame, created using Reynolds Number Condition 2, and Atomization Airflow Case 3. Thus, the atomization air flowrate was scaled with the Reynolds number of the combustion airflow, so Atomization Air Case 3 implied that 0.07 g/s of atomization air were fed when Reynolds Number Condition 1 was applied, and that 0.14 g/s of atomization air are fed when Reynolds condition 2 was applied.

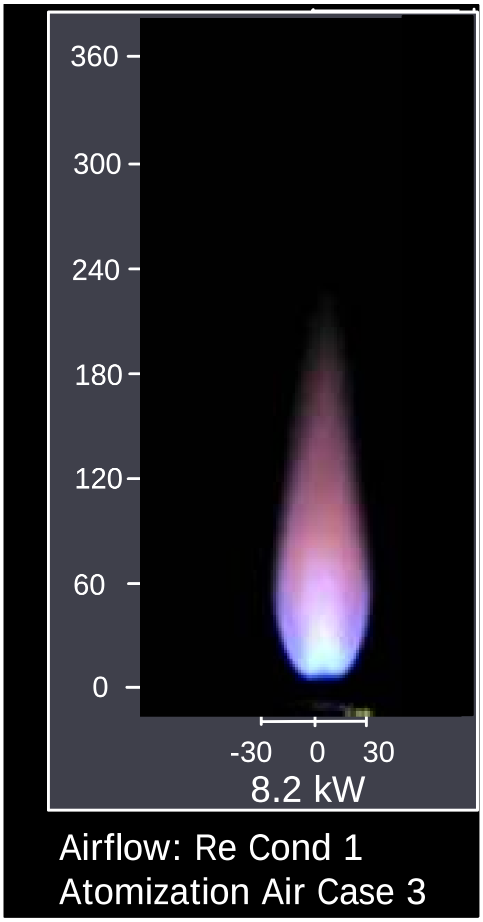

Figure 48. Scaled 8.2 kW flame

Figure 48 indicates that this approach to scaling of flames is valid, with certain caveats. The flame shown in the figure was an 8.2 kW flame at Reynolds Number Condition 1, and did, in fact, closely resemble the 16.4 kW flame at Reynolds Number Condition 2. There were some differences; for example, the length and shape of the flame was not quite the same. The differences may be due to factors that were not addressed directly, such as the amount of energy needed to vaporize the fuel, relative velocities of droplets in the fuel spray, fuel droplet size distributions, and surface tension effects in the fuel spray. The fuel spray will be considered in greater detail below. For the moment, it is sufficient to note that the flame can at least be approximately scaled if the relationship between airflow and thermal loading parameters is maintained from one operating condition to another. As long as the relationship is the same, and the system pressure and effective fuel atomization are maintained, a very similar flame structure should be observed.

6.8 Effect of Airflow Distribution on Flame Structure

Given that the scaled flame, at Reynolds Number Condition 1, and at a thermal load of 8.2 kW, seemed to share important structural features with the 16.4 kW flame at Reynolds Number Condition 2, further experiments were carried out in order to examine the effect of airflow distribution on flame structure. The 8.2 kW thermal load was retained, and the total combustion air flowrate was held constant, at 10.94 g/s. The reader will recall that, for Reynolds Number Condition 1, equal volumetric air flowrates were fed through each annulus. The proportion of air fed through the inner and outer annuli was then varied, so that, in the first case, only 25% of the total air was fed through the inner annulus, and in the last 75% of the total air was fed through the inner annulus. The three distributions examined will be referred to as the 25/75, 50/50, and 75/25 distributions.

The swirl configuration was not altered, and remained the 45-i/Null-o configuration that had received detailed attention so far.

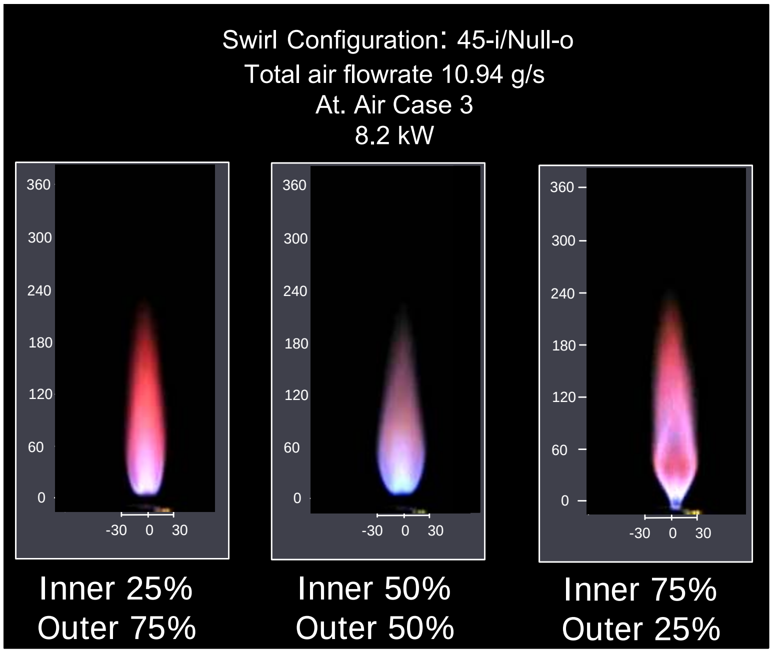

Figure 49. Effect of airflow distribution on scaled 8.2 kW flame

The three flames created by the different airflow distributions are shown in Figure

49. An increase in the proportion of air fed through the inner annulus increased the overall swirl in the flow, since only the air flowing through the inner swirler had any swirl imparted to it. The flame obtained using the 75/25 combustion airflow distribution was not lifted; in this case, the swirl in the airflow was great enough for combustion to be stabilized all the way down to the fuel nozzle. The 25/75 distribution was lifted, and the location where combustion was initiated occurred at the same axial location as in the flame obtained with the 50/50 distribution. The flame from the 25/75 distribution was narrower and longer than those from the other distributions.

Interestingly, the most compact flame was still the one produced by the 50/50 airflow distribution. Increasing the amount of swirl in the flow did not necessarily produce a more compact flame. The factors controlling the flame geometry are more complex; mixing, droplet evaporation, and heat release location all play a role in shaping the reaction zone, and these are linked to the flowfield characteristics in complex ways.

In any case, the 45-i/Null-o swirl configuration, with a 50/50 airflow distribution, produced a flame with features best suited for a compact, underwater propulsion system, and the focus will remain on this experimental case.

6.9 Fuel Spray Characterization

6.9.1 Planar Laser Scattering

Up to this point, the fuel spray has not been discussed in any detail. Thermal loads, as a function of fuel flowrate, have been stated, but the detailed structure of the fuel spray has not been dealt with. The structure of the flame has been shown to depend primarily on the flowfield characteristics and on the thermal load. However, a more detailed understanding of the spray characteristics is necessary to develop a really thorough understanding of the factors affecting the flame structure.

Given that the 45-i/Null-o flame, at two scaling conditions, had already been characterized, further work was done to understand further aspects of this flame. Since the flame structure appeared to be optimal when the 50/50 airflow distribution was employed, this condition was also applied during characterization of the fuel spray. The fuel spray was examined under Reynolds Number Condition 2 and Atom. Air Case 3. Thus, 9.3 g/s of air were fed through each of the combustion air annuli, and 0.14 g/s of atomization air was fed through the fuel nozzle.

Two fuel flowrates were examined. The fuel nozzle was rated by the manufacturer to disperse 0.5 gallons per hour of water. This corresponded to a flowrate of 31 ml/min, and to a thermal load of methanol of 8.2 kW. This condition was examined first.

Since a 16.4 kW thermal load was also used in experiments discussed above, the methanol spray associated with a fuel flowrate of 62 ml/min was also examined. The fuel sprays were first imaged under noncombusting and combusting conditions, using planar laser scattering. Components of the PIV system, including the lasers and one of the cameras, were used to obtain the images. As in the PIV procedure, described above, a narrow-band-pass filter, fitted to the camera optics, and a mechanical shutter were used to remove the image of flame in the combusting cases, allowing only images of the droplets imaged by the laser sheet to be detected by the camera.

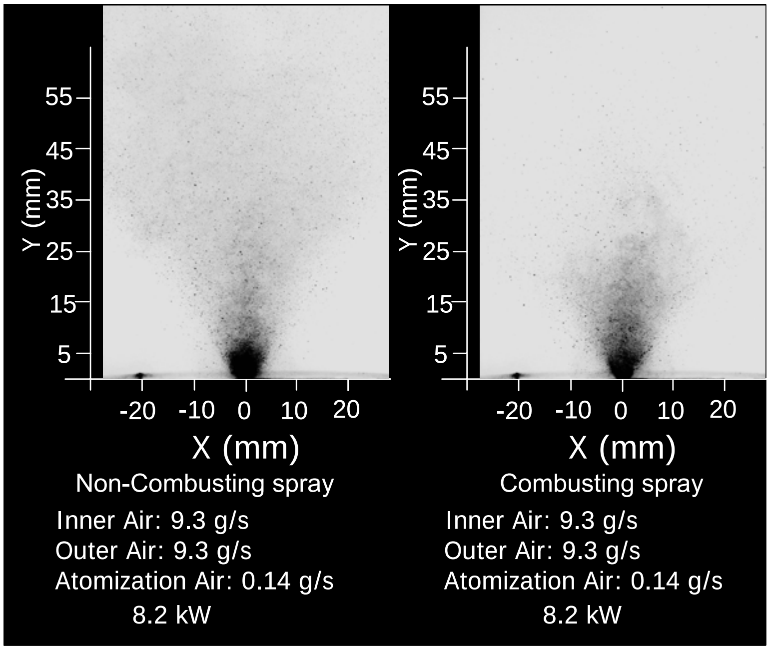

Figure 50. Fuel spray images, 8.2 kW fuel flowrate

Planar laser scattering images of the 8.2 kW fuel spray, under noncombusting and combusting conditions, are shown in Figure 50. Images of the 16.4 kW fuel spray, under noncombusting and combusting conditions, are shown in Figure 51. The images are monochrome, and have been inverted, so that fuel droplets appear as dark regions in the image. At both fuel flowrates, the spray was a solid-cone spray, with an included angle of approximately 60 degrees. The spray associated with the 16.4 kW fuel flowrate was much denser, particularly near the fuel nozzle. This was reasonable, since the volumetric flowrate of fuel through the nozzle in this case was doubled. The sprays were very symmetrical in both cases.

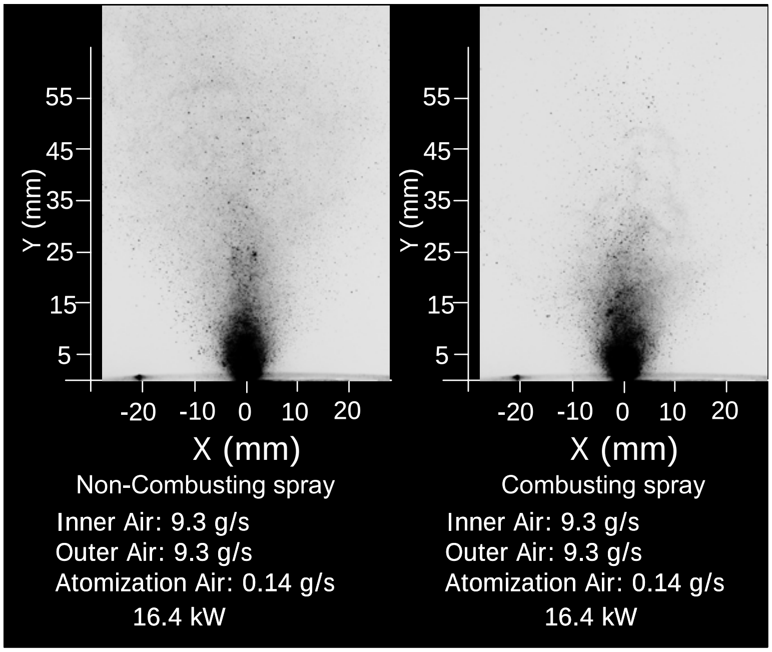

Figure 51. Fuel spray images, 16.4 kW fuel flowrate

In the combusting

cases, the smaller droplets in the spray were not seen in regions more than 35 mm above the fuel nozzle. This is reasonable, of course, since the heat from the flame eliminated the droplets rapidly. Large droplets also became scarce at elevations over 55 mm above the fuel nozzle. Some isolated droplets, with unusually large diameters, persisted even further in the flow; this is more the case in the 16.4 kW spray.

6.9.2 PDPA Examination of Fuel Spray

More detailed information about the characteristics of the fuel spray was obtained using the PDPA system. Only one droplet at a time can be measured using the PDPA technique; if two or more pass simultaneously through the measurement junction formed by the four laser beams, the data point is discarded. Data was gathered on one side of the combustor centerline, at an elevation 35 mm above the fuel nozzle. This location was chosen, because droplets at this elevation in the spray were fully formed, and were spaced out widely enough to pass individually through the measurement junction, but were only beginning to burn away. Data was gathered at 2 mm intervals, until the edge of the spray was reached.

Plots of droplet mean axial velocity and mean radial velocity are shown in figures 52 and 53. It is apparent that the primary factor influencing the shape of the curves, particularly near the combustor centerline, was the presence or absence of combustion. The 8.2 kW curve and the 16.4 kW curve share the same shape, and nearly the same values, at every radial location.

Plots of the arithmetic mean diameter and Sauter mean diameter are shown in Figures 54 and 55. The arithmetic and Sauter mean diameters are often referred to as D10 and D32 in the literature (Fleming, et al., 2001). The arithmetic mean diameter of a droplet population was calculated from

$$\boldsymbol{D10} = \frac{\sum \boldsymbol{N_i D_i}}{\sum \boldsymbol{N}} \qquad (17)$$

While the Sauter mean diameter was calculated from

$$\boldsymbol{D32} = \frac{\sum \boldsymbol{N_i D_i^3}}{\sum \boldsymbol{N_i D_i^2}} \qquad (18)$$

In the expressions, *N* is the total number of droplets in the sample and N_i is the number of droplets with a particular diameter, D_i. The arithmetic mean diameter provides a simple measure of the average droplet size, while the Sauter mean diameter is the diameter of a droplet that has the same volume-to-surface area ratio as the entire droplet population.

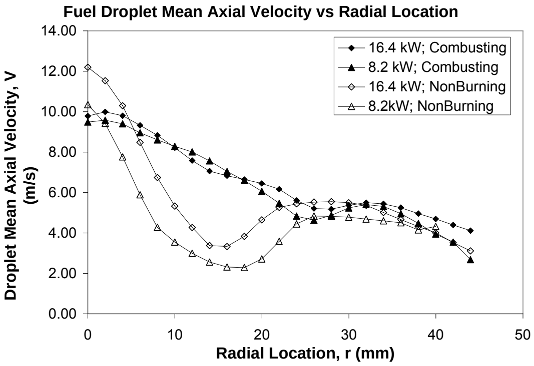

Figure 52. Fuel droplet mean axial velocity

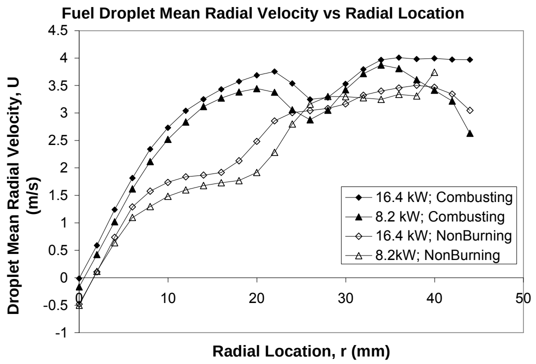

Figure 53. Fuel droplet mean radial velocity

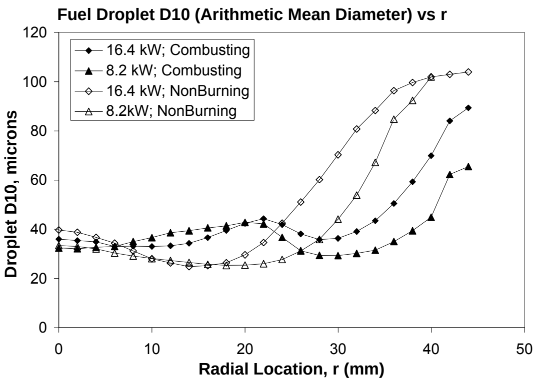

Figure 54. Mean arithmetic diameter curves

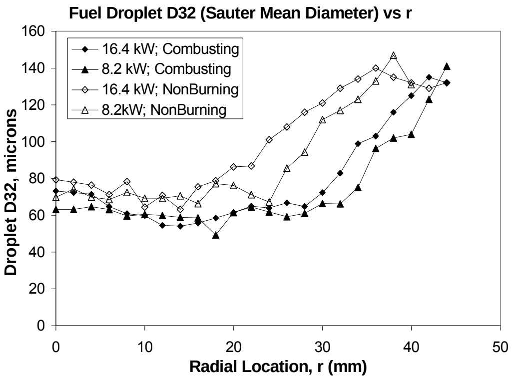

Figure 55. Sauter mean diameter curves

Again, the shapes of the curves were influenced more by the presence or absence of combustion than by the fuel flowrate. This is a clear indication that the twin-fluid atomization system employed in the burner provided effective fuel atomization across a wide range of fuel flowrates. The D32 was generally larger than the D10, because of the range of droplet sizes observed in the population. The D32 is sensitive to large droplets in the spray. Even if they do not occur frequently, they may affect the D32 of the entire population. This accounts for the noise seen in the D32 curves. Only a few large droplets are necessary to introduce considerable variation into the calculated value of D32 at a given point.

6.9.3 Effect of Atomization Air Flowrate on Fuel Spray

The effect of the atomization air flowrate on the fuel spray properties is also of interest. For both fuel flowrates, the D10 and D32 were measured at the spray centerline, and the atomization air flowrate was varied across a wide range. The data gathered is shown in Figure 56. It is clear that a certain amount of atomization air is necessary to atomize a given fuel flowrate. Above this minimum, however, the atomization air flowrate can be varied across a wide range, in this case from about 0.09 g/s to about 0.21

g/s, without any significant change in the mean droplet diameters. Again, twin-fluid atomization is shown to provide flexible, stable atomization across a wide range of operating conditions, which means that atomization air flowrate and fuel flowrate are not necessarily linked. A given atomization air flowrate can be set in order to achieve the correct flame structure, and as long as it is sufficient to provide effective atomization, the fuel will be effectively atomized across a range of power settings.

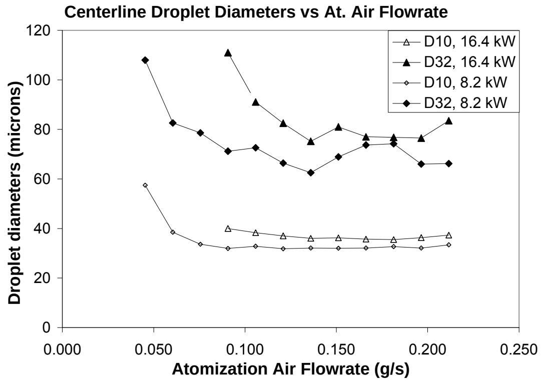

Figure 56. Effect of increased air flowrate on atomization

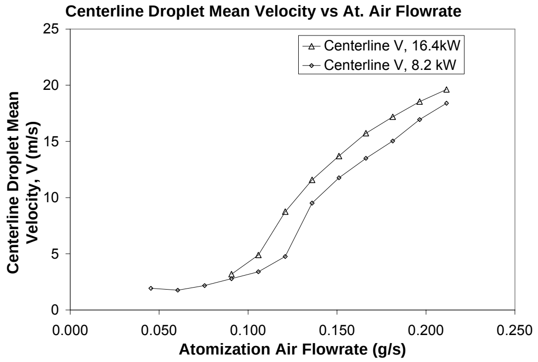

Figure 57. Effect of increased air flowrate droplet velocity

One characteristic of the fuel spray was found to vary with atomization air flowrate. The mean velocities of droplets in the spray at the centerline were observed to increase nonlinearly with atomization air flowrate, as shown in Figure 57. This effect is not particularly important, however, since it is simply linked to the increasing atomization air jet velocity. The momentum of individual droplets, 30-50 microns in size, does not appear to have a significant effect on the flame structure. The effect of the increased velocity of the atomization air jet would play a much larger role in determining the structure of a flame due to its interaction with the other air flows fed into the burner.

6.10 Exhaust Temperature Measurement

Further experiments were carried out with the combustion enclosure installed.

Initially, the combustor was fired at atmospheric pressure to examine the flame structure and to measure the exhaust temperature. The aluminum nozzle block was set in place, but no exhaust nozzle was installed. The exhaust port was unobstructed, and this port, which was 16.8 mm in diameter, allowed the exhaust gas to escape without a large rise in the combustor pressure. The exhaust gas temperature was measured 55 mm above the exhaust port, at the centerline of the flow.

The 45-i/Null-o swirl configuration and Reynolds Number Condition 2 were employed. 0.14 g/s of atomization air were fed to the nozzle. The combustor was fired at 8.2 kW and 16.4 kW thermal loads.

The flame structure, under enclosed conditions, was found to closely resemble the same flame structure under unenclosed conditions. The enclosure of the flames had no significant impact on the shape of their luminous regions, and important dimensions, such as the liftoff distance, width, and overall length, did not change (see Figure 58). Only the 16.4 kW flame was visibly affected by the presence of the enclosure. The upper tip of the flame cannot be seen in Figure 58, due to the size of the observation window, but this section of the flame made contact with the nozzle block at the top of the combustor. The general similarity between the enclosed and unenclosed flames is due largely to the size of the combustor. The combustor used here is considerably wider than the inlet duct, and

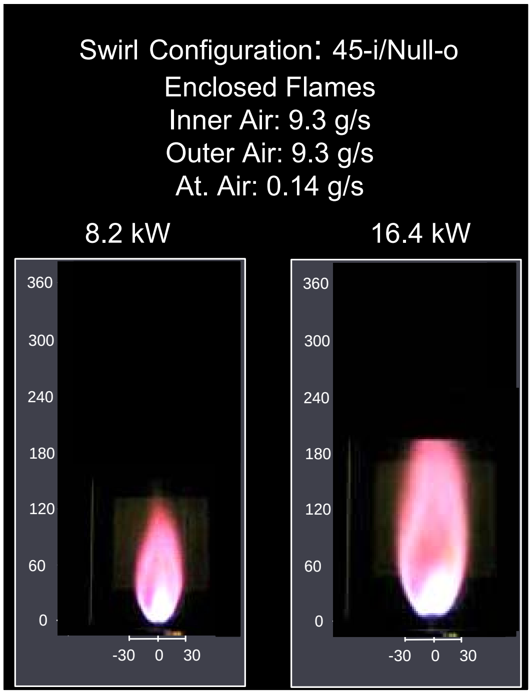

Figure 58. Enclosed, unpressurized flames

was sized so that deposition of fuel droplets on the windows would not present an obstacle to observation. In a smaller combustor, interference between the flow and the wall of the enclosure might significantly change the flame structure. The tests were of brief duration, under one minute in length, and the temperature of the combustor enclosure did not rise above 40 °C.

The temperature of the exhaust gas produced at both thermal loads was measured. The overall equivalence ratio was quite lean in both cases. For the 8.2 kW flame, the equivalence ratio was 0.18, while for the 16.4 kW flame, the overall equivalence ratio was 0.35. For this reason, relatively low exhaust gas temperatures were measured. The 8.2 kW flame produced an exhaust gas temperature of 458 K, while the 16.4 kW flame produced an exhaust gas temperature of 733 K. As described above in the chapter on diagnostics, the thermocouple measurements were not corrected for radiation or other losses, and give only an approximate value. The total recorded combustor pressure rose to 1.06 bar when the 8.2 kW flame was examined, and to 1.08 bar when the 16.4 kW flame was examined.

The theoretical exhaust gas temperatures, based on an assumption of complete combustion and an adiabatic system, are 712 K and 1087 K for the 8.2kW and 16.4 kW cases, respectively. The measured temperatures are much lower, because the tests were of very brief duration and the combustor was not allowed to heat up. The temperature was measured in the center of the exhaust jet, and very near the combustor exit, where entrainment of cool outside air is not likely to lower the measured temperature. The temperature measurements were brief, because later submerged tests were also of very brief duration, and because the water in the mixing chamber provided a large heat sink.

The enclosed, non-submerged, unpressurized flames had to be examined under conditions where the enclosure would experience a similarly small rise in temperature. The stream of exhaust gas was thus cooled significantly, due to contact with the walls and nozzle block.

6.11 Submerged, Nonreacting Experiments

In order to examine the combustor under submerged conditions, the mixing chamber, with its baffle cartridge, and exhaust nozzles were installed. A small air flowrate was fed to the combustor, so that the pressure in the combustor was 0.4 psig higher than the ambient. Once the combustor pressure was slightly elevated, the mixing chamber could be filled readily with water, to a depth of 15 cm. The lowest baffle plate was submerged. Air emerged continuously from the exhaust nozzle during filling, preventing any water from entering the combustor.

A stream of air was then fed into the combustor until the combustor pressure rose to 1 psig (total pressure 1.07 bar). The combustor pressure, P_C, was found to be the most important parameter affecting the behavior of the exhaust jet. Swirl associated with the air was found to play no role in determining the exhaust jet behavior.

With $P_C = 1.07$ bar, the exhaust jet was observed to emerge from all three exhaust nozzles as a repeatable series of bubbles, whose motion depended primarily on buoyancy forces. Images of the exhaust jet were recorded at 500 frames per second. Stills, showing a representative bubble cycle produced by each of the three nozzles (FMN, CPN, and CCDN) are shown in Figures 59, 60, and 61. Significantly, the nozzle geometry at this combustor pressure had very little effect on the shape of the bubbles emerging from the nozzle, nor does it greatly affect the frequency with which they emerge.

The Strouhal numbers of the bubble formation cycles were calculated for each nozzle geometry, using equation (12). Some variation in the duration of the cycle was observed, and the Strouhal numbers reported for each geometry are average values. The Strouhal number of the bubble emergence cycle for the flush-mounted nozzle was found to be 0.0023. When the CPN Nozzle was used, the Strouhal number of the bubble formation cycle was found to be 0.0037, and when the CCDN nozzle was used, the Strouhal number was 0.0045. These values are much smaller than those associated with

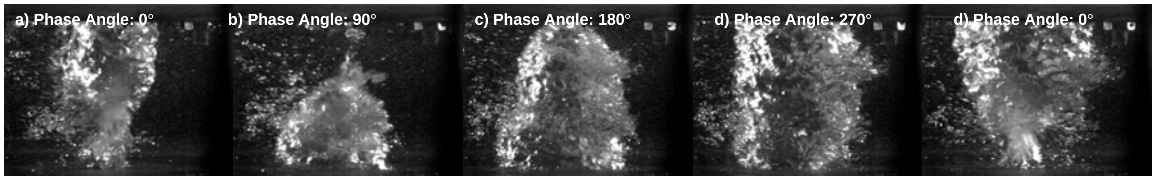

Figure 59. Bubble-emergence cycle, flush-mounted nozzle

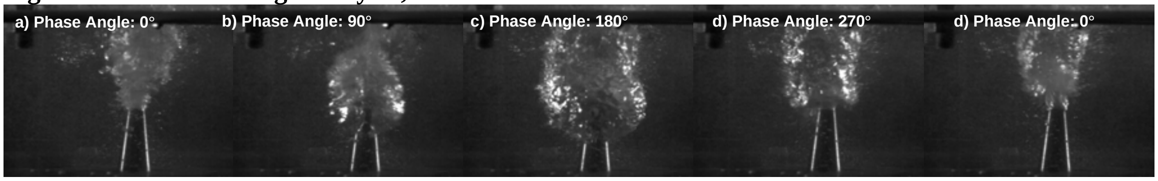

Figure 60. Bubble-emergence cycle, conical projecting nozzle

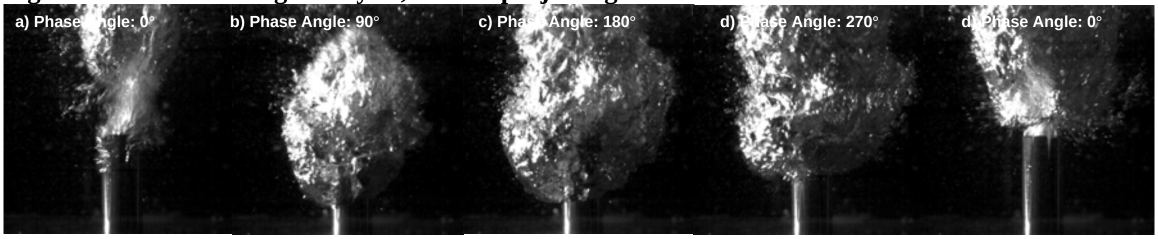

Figure 61. Bubble-emergence cycle, corrugated converging-diverging nozzle

shear layer instabilities in single-phase flows, where the Strouhal number is usually found to be 0.2 to 0.5 (Schadow and Gutmark, 1992). The Strouhal numbers varied slightly with nozzle geometry, because the shape of the trailing edge of the bubble was different. In a buoyancy-driven flow, the rate at which a bubble of gas can rise through the surrounding liquid depends on the balance between buoyant forces and drag forces acting on the bubble. The bubbles formed by the projecting nozzles (CPN and CCDN) were able to form smoothly-rounded trailing edges, which allowed them to rise more rapidly. The lower surface of the bubbles emerging from the CCDN nozzle was initially distorted by lobe-shaped structures emerging from the perforations in the nozzle. This effect is shown in Figure 62. However, as the bubble emerged fully, the lobe-shaped distortions disappeared, due to surface tension, allowing a smoothly-rounded lower surface to form on each bubble. The flow emerging from the FMN initially spread out laterally before rising to form the bubble, and the formation of the lower portion of the interface took more time. As a result, the Strouhal number was lower.

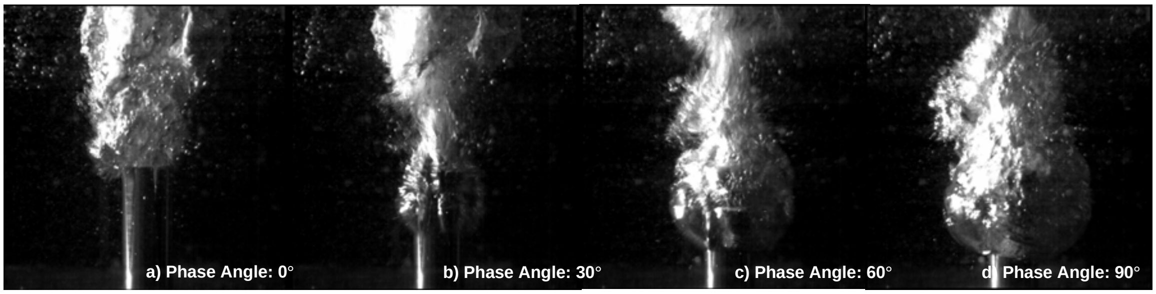

Figure 62. Initial phase of bubble emergence from CCDN nozzle, showing lobe-shaped distortions of bubble surface due to ejections from perforations

The total diameter achieved by the bubbles was consistently approximately 5*D_E, where D_E was the diameter of the throat of the exhaust nozzle.

Further nonreacting experiments were carried out with airflows at P_C = 2.02 bar. In this case, the flow through the exhaust nozzles was choked, since the necessary pressure drop across the exhaust nozzle was present. The agitation of the water in the mixing chamber was much more violent at the higher pressure condition, and direct observation of the behavior of the exhaust jet emerging from the FMN was impossible. The water rapidly became so clouded by small bubbles that the region in the vicinity of the exhaust jet was obscured.

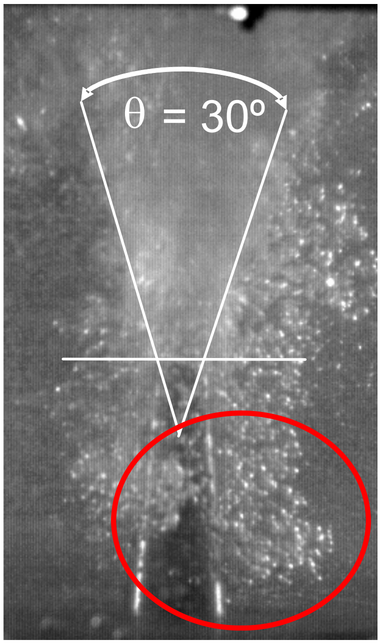

Figure 63. Open-jet mode, observed at P_C = 2.02 bar; bubbles ejected upstream are circled

However, the exhaust jet emerging from the pressurized combustor could be observed if either the CPN or CCDN were installed. Two general jet modes were observed at this combustor pressure condition. The first mode, which will be referred to as an open-jet mode, consisted of an open channel to the surface of the water. The walls of the channel angled outward at approximately 30 degrees. This jet mode, seen emerging from the CPN nozzle, is shown in Figure 63. The open-jet mode was not stable, however, and collapsed occasionally, at apparently random intervals. When such a collapse occurred, the nozzle was briefly blocked by water. A round bubble then formed around the nozzle, with a heavily corrugated surface. The bubble rapidly disintegrated into a cloud of much smaller bubbles, a few millimeters in diameter. Interestingly, the maximum diameter reached by the bubble structure in this mode was still 5*DE, just as had been the case at the lower combustor pressure. Multiple bubble structures sometimes occurred in close succession before the open-jet mode could be reestablished. The Strouhal number of this cycle was also found to be approximately 0.002 to 0.005. This jet mode will be referred to as the bubble-formation mode. An image of such a bubble, emerging from the CPN Nozzle, at its maximum diameter just prior to breakup, is shown in Figure 64.

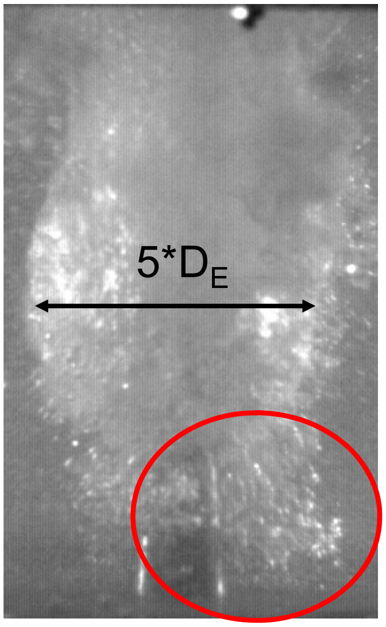

Figure 64. Bubble mode, observed at P_C = 2.02 bar; bubbles ejected upstream are circled

The open-jet and bubble-formation modes were observed for both the CPN and CCDN nozzles. The type of unstable cycle, and the mechanism of open-jet formation and collapse, did not appear to be effectively controlled by the special features built into the CCDN nozzle. However, the perforations cut through the walls of the CCDN nozzle did allow gas to escape further upstream, closer to the mixing chamber baseplate, when this nozzle was used. The perforations also produced a more heavily-corrugated surface in the air/water interface, since lobe-shaped gas structures were forced laterally out of the nozzle through the perforations.

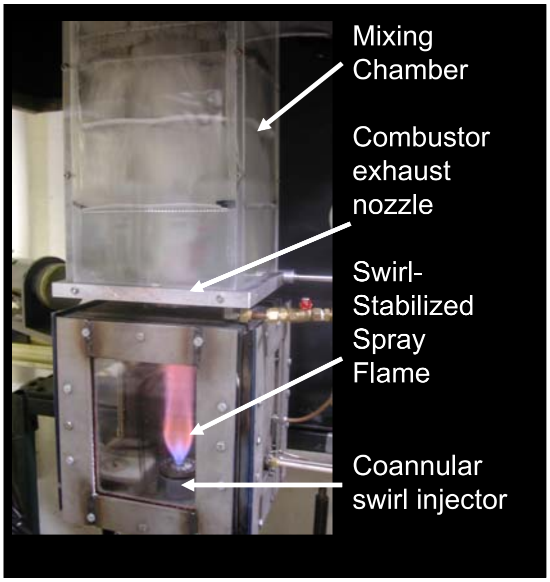

Figure 65. Submerged combustor in operation

One further observation was made. The high-speed jets were generally surrounded by veils of small bubbles, with diameters on the order of millimeters. These bubbles are indicated by the circled regions in Figures 63 and 64. These bubbles were often ejected upstream, toward the baseplate, and then slowly rose upward due to buoyancy. The mechanism by which these bubbles were formed may be indicative of particular instability mechanisms present in the two-phase regime. In particular, pressure fluctuations, interacting with the interface, may play a role in the creation and location of these bubbles. The possible nature of the instability mechanism is discussed in greater detail in the chapter on discussion, below. No comparable behavior has ever been reported in single-phase systems. Neither the momentum of the exhaust jet nor buoyancy would appear to explain their presence in the regions where they are observed, so the process by which these bubbles are formed will be discussed in greater detail in the discussion section of this chapter.

6.12 Submerged Reacting Flow

A submerged flame, venting its exhaust jet into the mixing chamber, can be seen in Figure 65. The flame shown in the image is a preliminary trial flame; the flame geometry shown differs slightly from the final flame achieved at the correct experimental conditions. The flow in the mixing chamber in the image is a white blur; the exposure duration used for the photograph was too long to capture the detailed motion of the two-phase flow.

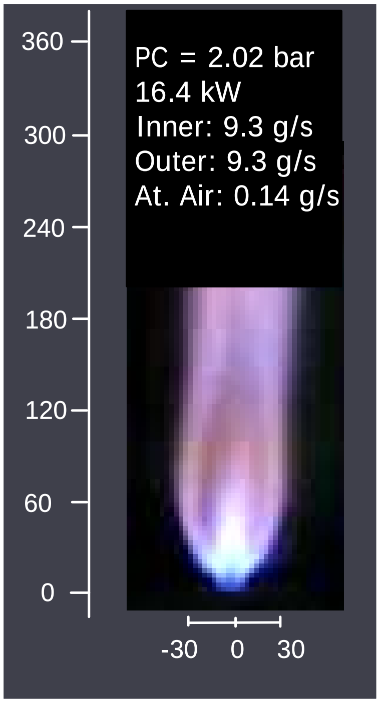

Figure 66. Pressurized, submerged flame

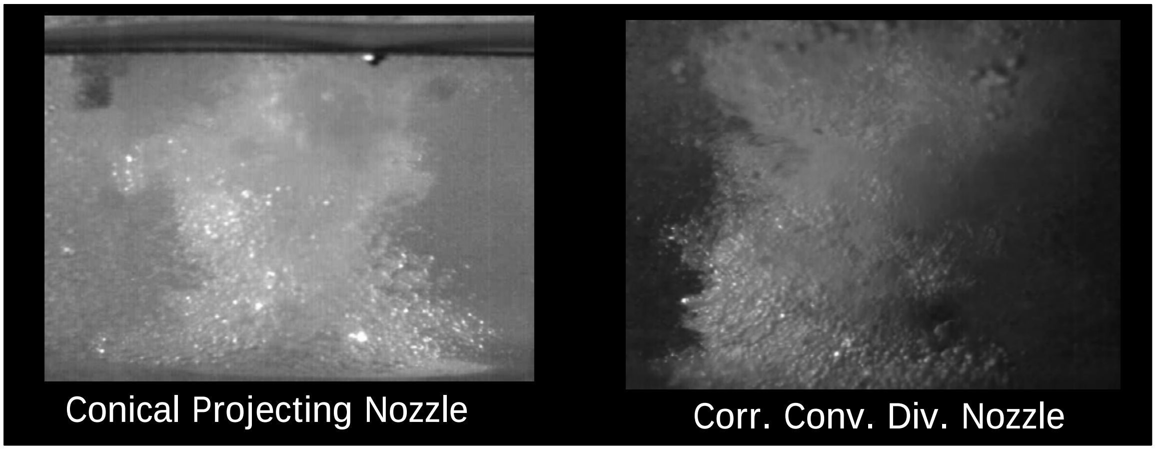

Figure 67. Exhaust jets produced by reacting flow in combustor with P_C = 2.02 bar; note curtains of bubbles surrounding jets from both CPN and CCDN nozzles

In order to examine the behavior of the two-phase interaction of an exhaust jet produced by a reacting flow, a 16.4 kW flame, using 9.3 g/s of air through the inner and outer annuli, 0.14 g/s of atomization air, and the 45-i/Null-o swirl configuration, was created under submerged conditions. The combustor pressure in this case rose to 2.02 bar. An image of this flame is shown in Figure 66. The structure of the flame is very similar to that of the atmospheric-pressure 16.4 kW flame described previously, and shows directly that the features of a swirl-stabilized, liquid-fuelled spray flame under confined and pressurized conditions can be analyzed and understood on the basis of data obtained from flames and flows examined under less-demanding experimental conditions.

The exhaust jet associated with this flame was forced out through both the CPN and CCDN nozzles, and the two-phase interaction was examined. Images of each condition are shown in Figure 67. The exhaust jets produced by the flame in the combustor were extremely chaotic. Dynamic events, occurring on a wide range of timescales, distorted and interrupted the structure of the flow. Both flows were also completely engulfed in curtains of small bubbles, which, again, were often ejected outward and downward. The distance traveled by the bubbles was greater in this case, where combustion was present, than it have been in the case of the nonreacting flow at the same P_C value. This observation is, again, consistent with Richtmyer-Meshkov instability, as will become clear in the discussion.

The absence of a dramatic difference between the jet properties observed with the CPN and CCDN nozzles, under nonreacting and reacting flow conditions, is also an indication that the flow, in the two-phase regime, is affected by fundamentally different instability mechanisms than are present in single-phase jet interaction. This point will also be discussed in further detail in the discussion section below.

6.13 Sound Spectrum Analysis

Since the experimental diagnostics available for examination of a two-phase system like that in the mixing chamber are limited, sound spectrum analysis represents a way to generate detailed information on the dynamic events occurring in the flow. The sound spectrum analyzer was connected to the baseplate of the mixing chamber, and sound spectra associated with the CPN and CCDN nozzles were obtained. Nonreacting cases at $P_C = 1.07$ bar and $P_C = 2.02$ bar were examined. The effect of combustion on the sound spectrum of the exhaust jet leaving the CCDN nozzle was also examined. The sound spectrum produced by the jet from the 16.4 kW flame, at $P_C = 2.02$ bar, was compared with the spectrum of the nonreacting air jet at the same combustor pressure.

The effect of increased combustor pressure on the CPN and CCDN sound spectra is shown in Figures 68 and 69. The principal effect of increased combustor pressure was seen at frequencies above 50 Hz. The lowest frequencies in the spectrum, which likely corresponded to unstable events in the jet with the largest length scales, were almost unaffected. The sound pressure levels associated with the higher frequencies, near 300 Hz, were increased by up to 20 decibels.

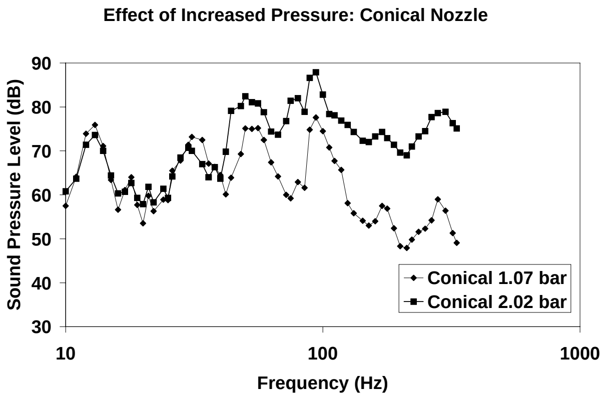

Figure 68. Sound spectra associated with CPN nozzle, nonreacting flow, showing effect of increased pressure

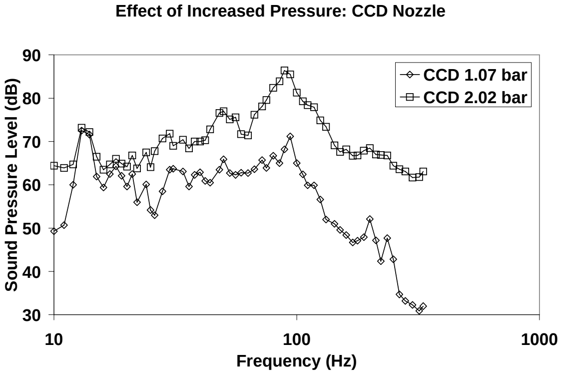

Figure 69. Sound spectra associated with CCDN nozzle; nonreacting flow, showing effect of increased pressure

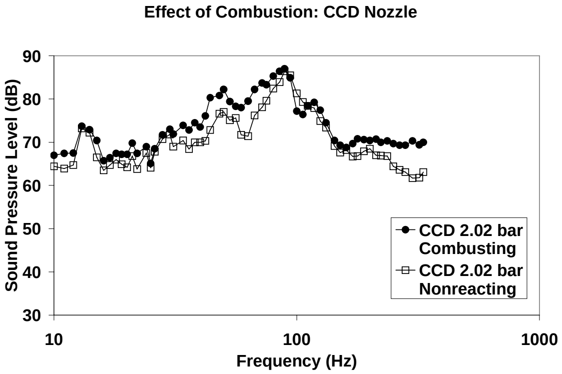

Figure 70. Sound spectra associated with CCDN nozzle; showing effect of increased combustion

While there were some differences in the sound spectra obtained for the CPN and CCDN nozzles, important features of the spectra were not affected by the changes in nozzle geometry. Both nozzles had associated sound spectra with local maxima at approximately 20 Hz and at 100 Hz. Other areas of the spectrum displayed differences, implying that some limited effect on the sound spectrum, and on the dynamic behavior of the flow, can be achieved through changes in exhaust nozzle geometry.

The effect of combustion (as compared with the nonreacting airflow) on the sound spectrum of the jet emerging from the CCDN nozzle was also limited, and is shown in Figure 70. Interestingly, the shape of the curve was nearly identical in the combusting and non-combusting cases. At most frequencies, the reacting flow displayed sound pressures 2-5 dB greater than the nonreacting flow. The added energy from the flame may be responsible for this effect. Other factors, such as the effect of increased temperature on the viscosity of the liquid phase, may also play a role.

6.14 Discussion of Results

6.14.1 Factors Affecting Flame Structure

As is clear from the results presented above, the structure of the flame is heavily dependent on the features of the air flowfield associated with the flame. The effect of the atomization air jet is of particular importance, and the presence or absence of the fuel spray does not significantly affect the interaction between the atomization air jet and the other features of the air flowfield. Different swirl configurations respond differently to the atomization air jet. Swirl configurations that impart high degrees of swirl display a single central recirculation region, and the atomization air jet (and fuel spray) are contained within the boundaries of this recirculation region. If the total amount of swirl imparted to the airflow is low, as is the case in the 30-i/Null-o and 45-i/Null-o configurations, the atomization air disrupts the recirculation region. In the case of the 30-i/Null-o configuration, this effect is so pronounced that no flame can be stabilized at all. However, in the case of the 45-i/Null-o swirl configuration, two distinct recirculation zones are formed. The smaller, near-field recirculation region surrounds the central atomization air jet. The larger, far-field recirculation zone stabilizes the flame. Interestingly, this swirl configuration produces the most compact flame. The flame associated with the 60-i/Null-o recirculation region is much longer.

This observation is unique in the literature. The effect of a central jet, directed up into the recirculation zone of a swirling flowfield, has never previously been described. The lifted flame produced by the two recirculation regions in the flow may allow more effective mixing between oxidizer and fuel upstream of the reaction zone, so that combustion can go to completion more rapidly in the reaction zone itself. This flame may therefore be behaving, to some degree, like a premixed flame. In the non-lifted flames, the flame seems to behave more like a diffusion flame, and the process of mixing between fuel and oxidizer appears to occur more slowly, resulting in a longer flame.

The thermal load was also found to have an important effect on the flame structure. At the thermal loads examined here, the length of the flame was found to increase in proportion to the thermal load. This effect appears to be linked to the expansion of gases in the far-field recirculation region, caused by the heat release from the flame. When more heat is released, the gases expand to a greater extent, forcing the boundaries of the recirculation zone and flame front outward.

6.14.2 Effect of Pressure on Flame Structure

The structure of the flame was not seen to change dramatically when the flame was enclosed, nor when it was pressurized. However, the increased pressure did have some slight effect on the flame structure. The changes observed are likely due to changes in the rates of chemical reaction at the flame front. Doubling the pressure doubles the concentrations of reactants, which will accelerate the rates of most chemical reactions. Many of the reactions in a flame depend on the collision of two molecules, leading to a second-order expression for the rate of the reaction, as given by

$$\boldsymbol{rate} = \boldsymbol{k}[\boldsymbol{A}][\boldsymbol{B}] \qquad (19)$$

The rate of the reaction depends on *k*, a temperature-sensitive rate constant, and on *[A]* and *[B]*, the respective volumetric concentrations of reactants A and B. The rate is therefore quite sensitive to concentration. Doubling the concentration in this case would increase the rate of the reaction by a factor of four. Flame chemistry is in itself an extremely complex subject, however, and will not be dealt with in further detail in this work.

The diffusivity of species is also sensitive to pressure, and, as the pressure (and density) in a system increase, the diffusivity decreases. In a turbulent spray flame, however, the diffusivity is relatively unimportant, since mixing by turbulent action is much faster. Similarly, increases in the rate of reaction due to pressure also have a limited effect on the flame structure, since the rates of reaction are already very high.

Changes in the evaporation of droplets from the fuel spray due to pressure also play a very limited role in shaping the flame structure. The vast majority of droplets evaporate very quickly at both atmospheric and elevated pressures, and most appear to evaporate fully before coming in contact with the flame front. Some larger droplets in the spray do appear to survive longer, but these apparently represent a small proportion of the total fuel, and play an insignificant role in determining the structure of the flame. The flexibility and utility of the twin-fluid atomization approach is also demonstrated here, since the average velocity of the atomization air jet is halved when the combustor pressure is doubled, assuming the mass flowrate of the atomization air is constant. This effect might present a problem if the atomization of fuel were significantly affected by the increase in pressure and resulting decrease in atomization air jet velocity. However, for the conditions examined here, it was found that the atomization air supplied was sufficient to effectively atomize the fuel at both 1 bar and 2.02 bar total pressure. Since the mean droplet diameter produced by the nozzle is insensitive to changes in atomization airflow across a wide range of atomization airflows, this atomization approach can be seen to be quite effective.

The main factors influencing the structure of the flame at the pressures examined here remain the airflow parameters and thermal load.

6.14.3 Two-Phase Exhaust Jet Characteristics at Low Combustor Pressure

The dynamic behavior of the two-phase exhaust jet interaction is determined primarily by the pressure drop across the exhaust nozzle. The geometry of the nozzle affects the geometry of the distortions at the interface only to a limited degree. When the total pressure drop across the exhaust nozzle is low, a buoyancy-driven flow is observed, in which the exhaust jet emerges as a series of distinct bubbles. The momentum of the exhaust jet is insignificant in comparison to the buoyant forces acting on the bubble. The presence or absence of swirl has no observable effect on the mechanism or period of bubble formation. Bubbles formed always achieve the same maximum diameter, which, in this case, is approximately $5*D_E$, where D_E is the diameter of the throat of the exhaust nozzle. The Strouhal numbers of the bubble-formation cycle were found to vary somewhat, depending on the exhaust nozzle geometry, implying that the length of the bubbles (but not their width) is changed by changes in the nozzle geometry. The two nozzles projecting more than 2.5*D_E above the mixing chamber baseplate show higher Strouhal numbers than the flush-mounted nozzle. The geometry of the bubble, during formation, affects the Strouhal number, because the relationship between buoyant forces and drag over the outside of the bubble changes. The balance of forces determining the rate at which the bubble can rise is affected, and the projecting nozzles allow the bubble to form a smoothly-rounded lower boundary, which decreases the drag, and allows each bubble to rise more quickly.

This exhaust jet condition, where the pressure drop across the exhaust nozzle is small, might be encountered in a submerged combustor if the combustor is at great depth, or is operated at a low power setting. Since practical submerged combustors would need to operate at a range of power settings, this buoyancy-driven exhaust condition may, in fact, be encountered. Since the exhaust jet has a particular dynamic mode at a particular average combustor pressure, it is entirely possible that unstable combustion may occur in the combustor if the combustor characteristics are such that heat release harmonizes with the exhaust jet dynamics. If the ejection of a bubble is linked, in some way, to an increase in heat release in the combustor, the Rayleigh criterion may be met, and unstable combustion may occur. This effect was not examined directly in the investigations described here, but it must be pointed out that this is a possibility, which may form the basis for future investigations.

6.14.4 Two-Phase Exhaust Jet Characteristics at Elevated Combustor Pressure

When the combustor pressure was increased to 2.02 bar, under nonreacting, airflow-only conditions, the dynamics affecting the exhaust jet were seen to change. The regular emission of distinct bubbles was not observed; instead, the exhaust jet displayed unstable behavior on a wide range of time and spatial scales. A detailed description of the unstable behavior of the jet is not possible at this point, due to the complexity of the instabilities observed, and the complications introduced by the two-phase interface between the exhaust gas jet and water.

Several salient comments can be made, however. The first significant observation is that there is no dramatic difference between the unstable behavior of the jet emerging from the CPN and CCDN nozzles. This point is significant because, in single-phase jet interaction situations, the behavior of a jet emerging from a simple converging nozzle, and the jet emerging from a converging-diverging nozzle would have different properties. With a combustor pressure of 2.02 bar, both jets are choked. The shock front is not stabilized at any particular point in the CPN nozzle, and is thus free to emerge from the nozzle and potentially interact directly with the region downstream of the nozzle. In the case of the CCDN nozzle, the converging-diverging design should trap the shock front at the narrowest section of the flow in the throat. Further, in a single-phase situation, the corrugations and perforations in the wall of the nozzle would allow the exhaust jet to interact with the surrounding fluid over a range of length scales, affecting the features of the turbulent interaction and introducing observable differences between the jet emerging from a simple converging nozzle and that emerging from a converging-diverging nozzle.

Given that both nozzles display very similar dynamic behavior in the two-phase exhaust jet experiments, it seems clear that the dynamics affecting two-phase interaction are fundamentally different than those affecting single-phase jet interaction. In a single-phase situation, Kelvin-Helmholtz instability (KHI) is the primary mechanism driving the unstable distortion of the jet boundary. KHI occurs at a flow boundary due to the low pressure of the fast-moving material in the jet. Any distortion in the boundary acts as an airfoil; as the fast-moving stream of material in the jet passes over the distortion, lift is created which amplifies the distortion. Growth of the distortions is initially linear, and, when the small structures created by KHI merge and interact, dominant modes can predicted, so that the resulting structures evolving at the boundary of the jet have Strouhal numbers between 0.2 and 0.5. The ultimate evolution of the instability becomes nonlinear, and the structure thus developed will generally break down into turbulence at some point, and then the ordered, regular structure of the distortions can no longer be observed.

This mechanism may certainly play a role in distorting the two-phase boundary present in the two-phase exhaust jets examined here; however, some distinct differences are observed. The two-phase jet was seen to operate in two modes, one where a continuous passage to the surface was opened, and one that occurred when this passage collapsed, resulting in the ejection of a large bubble structure. The Strouhal number of these bubble structures was still observed to be approximately 0.002, and the maximum diameter was still approximately $5*D_E$, indicating that the buoyancy effects seen when the total combustor pressure was 1.07 bar may play a role at the higher combustor pressure, as well. The jet was also surrounded much of the time by curtains of small bubbles that were ejected outward from the exhaust jet, to maximum distances anywhere from 2*D_E to 10*D_E. The mechanism by which these bubble curtains were generated may indicate the presence of pressure-wave interactions with the interface, an instability mechanism similar to that observed in Richtmyer-Meshkov instability.

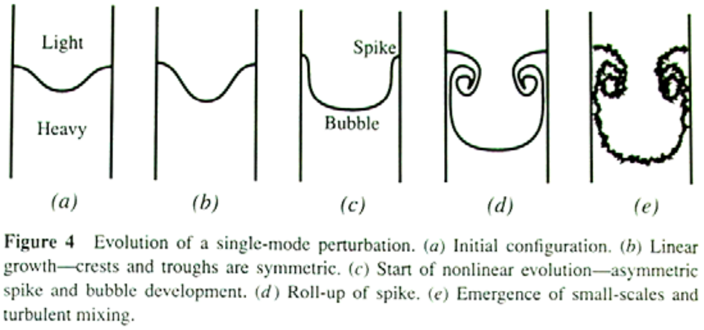

Figure 4 Evolution of a single-mode perturbation. (*a*) Initial configuration. (*b*) Linear growth—crests and troughs are symmetric. (*c*) Start of nonlinear evolution—asymmetric spike and bubble development. (*d*) Roll-up of spike. (*e*) Emergence of small-scales and turbulent mixing.

Figure 71. Initiation and growth of Richtmyer-Meshkov Instability (from Brouillette, 2000)

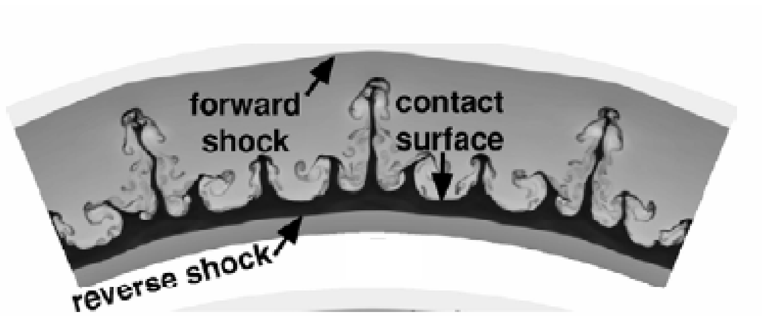

Figure 72. Interface distortion via Richtmyer-Meshkov instability (from Drake, 2005)

The RMI mechanism has been studied in a number of contexts, including the evolution of structures in stellar nebulae and laser-driven nuclear fusion experiments. Essentially, RMI occurs when a shockwave travels through one phase and collides with a phase interface (Brouillette, 2002) . A rarefaction wave is reflected from the interface back through the phase in which the shockwave originated, and the interface itself is distorted and pushed forward through the adjacent phase as the shockwave passes through. This process is illustrated in Figure 71, (from Brouillette, 2002). The growth of the distortion in the interface is initially linear, but rapidly becomes nonlinear past as certain point. Once an interface distortion has been amplified far enough, the boundaries of the distortion are themselves affected by KHI, which distorts the boundary and produces a distinct mushroom-shaped structure. The boundary will then tend to be further distorted by turbulence. This effect is shown directly in Figure 72, (from Drake, 2005). Drake (2005) investigated RMI in connection with shock interactions between adjacent regions in stellar nebulae. The effect of RMI on structures seen in supernovae is also examined by Kane, et al. (1999). The same type of mechanism may be connected with the clouds of bubbles that surround the exhaust jet emerging from the submerged combustor. A jet of gas, punched through the interface by a shockwave, can remain a coherent jet only briefly. It must break down rapidly into a string of bubbles, which are then controlled by surface tension, drag, and buoyancy. This mechanism may explain how clouds of bubbles are generated upstream of the exhaust nozzle exit, and the fact that the bubbles associated with the exhaust jet from the combusting case penetrate further into the surrounding liquid, since the amplitudes of peaks in the sound spectrum, which are associated with pressure waves in the system, are greater when combustion is occurring.

Due to the characteristic behavior and location of the bubbles surrounding the jet, it appears likely that the two-phase interface of the exhaust jet may be destabilized by pressure waves from the combustor. Both the CPN and CCDN nozzles display this effect, so direct interaction between the shock front in the sonic jet and the two-phase interface is not likely to be primarily responsible. The dynamic pressure in the combustor was not measured directly in these experiments, but the sound spectra associated with the jets provide significant insight. The sound spectra associated with both nozzles, under nonreacting and combusting conditions, are similar, and the behavior of small bubbles observed near each nozzle is similar. An intense peak, with a sound pressure level near 90 dB, is observed at a frequency of 100 Hz. The peak is present both at a combustor pressure or 2.02 bar and at a combustor pressure of 1.07 bar, though, obviously, the amplitude is much greater when the combustor pressure is 2.02 bar. The sound waves corresponding to this peak may destabilize the jet interface in a way that drives the RMI-type instability. Unfortunately, the flow is too chaotic for this hypothesis to be directly confirmed on the basis of the data presently available, but future work with better diagnostic tools may make it possible to do so.

The effect of combustion on the observed unstable behavior of the exhaust jet offers further evidence that pressure-waves play an important role in determining the exhaust jet behavior. In the combusting case, the clouds of small bubbles ejected by the jet were seen to be denser, and the bubbles were ejected further from the jet. This is consistent with the sound spectra of the jet, which shows somewhat higher sound pressure levels at almost every frequency, including the peak at 100 Hz, when combustion is present. The effect of combustion appears to promote the lateral ejection of bubbles, partly because the sound pressures are increased, and perhaps also because the viscosity of water in the immediate vicinity of the jet is reduced by the heated exhaust stream.

Some sort of pressure-wave interaction with the interface, resulting in an instability that generates bubble clouds, may be present; however, there are several further factors that make a straightforward analysis of this phenomenon difficult. First, RMI is usually studied in connection with very intense shockwaves. In the two-phase exhaust jets examined here, there is no evidence of a direct interaction between a shockwave and the interface; any wave-induced distortion of the interface must take place in connection with acoustic pressure waves, which are much less intense. RMI is also generally encountered in systems where an acceleration of both phases is oriented coaxially with the path of the pressure wave. In the two-phase exhaust jets, the interface is vertical (rather than horizontal), and the acceleration due to gravity, as well as the gradient in density between phases, is not necessarily aligned with the path of the wave. RMI is also generally associated with systems where the pressure wave travels through the more-dense phase, and rebounds from the interface between the more-dense and less-dense phases. The denser phase is driven effectively into the less-dense phase. In the exhaust jet instability, however, an acoustic wave would have to push the less-dense (gas) phase into the more-dense (liquid) phase in order to produce bubbles located at great distances from the exhaust jet. Some question exists, therefore, as to whether a pressure-wave interaction of the type proposed here would really be RMI, or whether it would be an example of a less-specific type of baroclinic instability.

Further, the increase in the number of bubbles associated with the heated jet may be due to the increased exhaust jet temperature, rather than an increase in the amplitudes of frequencies in the sound spectrum. Although the bulk temperature of the water phase never exceeded 40 °C in these trials, liquid water may be vaporizing at the interface, destabilizing it, and promoting the ejection of bubbles. Bubbles may also be forming near the interface, and then be pushed outward by large-scale motions of the liquid phase, which cannot be characterized directly in the present experiments. Further investigation into these phenomena could yield fundamental insights into the precise nature of the instabilities affecting these kinds of interfaces.

6.14.5 Effect of Submersion on Pressurized Flame

The flame in the combustor, fired into the water in the mixing chamber, was quite stable, and displayed no fluctuations in size or intensity that would indicate a direct unstable interaction between the flame and the condition at the exhaust nozzle. This observation can be explained by the fact that the exhaust jet was choked. In a choked flow, it becomes impossible for conditions downstream of the constriction to affect conditions upstream, and this indicates that submerged combustors can be operated quite readily as long as such a choking condition occurs. However, it is worth noting that the large pressure drop across the exhaust nozzle would only occur at a high combustor power setting, or when the vehicle is operated in shallow water. At a high combustor pressure, however, the exhaust jet is quite noisy, and would make the vehicle easily detectable; a lower pressure drop across the nozzle would make the vehicle more quiet. Managing these factors would represent the major challenge in development of practical underwater propulsion systems using combustion as a power source.

7. Conclusions

7.1 Conclusions of Present Work

7.1.1 Submerged Combustion

The swirl combustor has been demonstrated under unconfined and confined, submerged conditions representing operation in shallow and deep waters. Effective operation of a swirl-stabilized combustor under submerged conditions is shown to be possible, even at relatively low combustor pressures. The two-phase exhaust condition at the exhaust nozzle exit examined here does not present a major obstacle to operation of a submerged combustor. Elementary precautions must be taken to avoid combustor flooding, and the combustor must be designed in such a way that a stable flame can be contained within the combustor volume, but there is no inherent barrier preventing systems like this from being implemented in a range of applications, and operated at a variety of power settings. Submerging the combustor can affect the flame in two ways, depending on whether the exhaust jet is choked. If the exhaust jet is not choked, the potential for a direct interaction between fluctuating pressure conditions in the combustor and an unstable exhaust jet condition exists, and the submerged combustor may also experience different wall temperatures (thermal boundary conditions) than is the case when it is not submerged. If the exhaust jet is choked, the downstream environment cannot affect the combustor pressure directly, but the thermal boundary conditions may still be altered by the liquid surrounding the system.

7.1.2 PIV Examination of Effect of Reynolds Number on Swirling Flowfields

3-D PIV is a highly effective way to characterize the complex, three-dimensional swirling flowfield emerging from a swirl assembly. The setup and calibration of the 3-D PIV diagnostic system must be validated, and a validation using turbulent jets crossing the laser plane at various angles is effective and reliable. The swirl number of the flow emerging from a twisted-vane swirl assembly changes slightly with air flowrate, due to changes in the boundary layers within the swirler. This effect is relatively weak, however. The swirl number increases as the air flowrate is increased, since the boundary layer at the outer wall of the duct becomes thinner, and more of the flow travels along the outer edge of each swirl vane, where the vane angle is greatest. The swirl number of a vane assembly can be approximated as the tangent of the assembly’s outer swirl angle, but this approximation is likely to be too high by about 20%-30%. The approximation will be better at high Reynolds numbers, since more of the flow is distributed toward the outer edge of the swirl vane.

7.1.3 Factors Affecting Structure of Swirl-Stabilized Flames

In the flames investigated, the overall length of the flame depends on the thermal load and on the swirl configuration. The swirl configuration has only a weak effect on the maximum diameter of the flame, but can affect the length of the flame. In the cases where a small outer vane angle is employed the flame geometry depends primarily on the geometry of the inner swirler. In cases where the outer vane angle (meaning the angle between the vane surface and the axial centerline) is large, the vane angle of the inner swirler becomes much less important. Counter-swirling flames do not vary dramatically from their co-swirling counterparts, though the flame region does appear to be slightly shorter. This may indicate that mixing of fuel and oxidizer occurs more rapidly in the counter-swirling flames.

7.1.4 Analysis of Flame Structure via Examination of Nonreacting Airflow

The structure of an enclosed, pressurized spray flame can be analyzed and predicted on the basis of data obtained in unconfined flame, so long as combustion is stabilized by internal rather than external recirculation regions in the flow, and the enclosure used to confine the flame is significantly larger than the flame. The flames examined in this investigation involve low overall equivalence ratios, and large amounts of excess air. Equivalence ratios of 0.15 and 0.35 were investigated, and these are similar to overall equivalence ratios found in gas turbine combustors. For flames under this type of operating condition, in both unconfined and confined cases, the structural features and overall dimensions of the flame are determined primarily by the features of the airflow and the thermal load. The features of the flame are quite similar to those of the nonreacting airflow. This may not be the case for flames where the equivalence ratio is closer to unity.

7.1.5 Effect of a Central Atomization Air Jet on Swirl-Stabilized Flame Structure

The nature of the interaction between the central atomization air jet and the recirculating flow depends on the swirl configuration and relative air flowrates emerging from the injector. If the relationship between the flowrates is constant, they can be scaled across a range of Reynolds numbers without changing the structural features of the flow. Under certain conditions, where the swirl associated with the combustion airflow is relatively weak, the central jet partitions the recirculation region at the center of the flow into near-field and far-field recirculation regions. However, if the swirl associated with the flow is relatively strong, a single recirculation region encloses the atomization air jet. If the swirl associated with the flow is too weak, the atomization air jet prevents any recirculation from occurring, and a flame can not be stabilized at all.

The most compact flame obtained can be achieved by use of a relatively weak swirl configuration, which, in connection with the atomization air jet, produces two recirculation regions in the flow. This flame is lifted, and the compactness of the flame appears to be due to premixing between the fuel spray, which occurs around the near-field recirculation region, which then allows combustion to go to completion more rapidly in the (larger) far-field recirculation region.

7.1.6 Twin-Fluid Atomization of Fuel

Twin-fluid atomization provides effective fuel atomization over a range of conditions. If the atomization air flowrate fed to the atomizing nozzle is held constant, a wide range of fuel flowrates can be effectively atomized. If the fuel flowrate is held constant, and the atomization air flowrate is varied, the diameters of the fuel droplets in the spray will not vary significantly, as long as the atomization air flowrate remains above a certain threshold. The nozzle used in these investigations, with this nozzle, appears to work well as long as more than 0.1 g/s of atomization air are used. If the atomization air flowrate drops below this threshold, the atomization will not be effective. Since the flame structure depends much more heavily on the features of the central jet than on the properties of the fuel spray, it is possible to control the jet in a way that allows the flame structure to be controlled, without compromising effective atomization.

7.1.6 Dynamics of Two-Phase Exhaust Jets

Two-phase exhaust jets display instability mechanisms which are not seen in single-phase cases. The primary parameter affecting the two-phase exhaust jet characteristics is the pressure drop across the exhaust nozzle. At low pressure drops, buoyant and drag forces dominate the behavior of the exhaust stream. At higher pressure drops, the jet interface is highly unstable, and appears to be affected by instability mechanisms different from those seen in single-phase jet interaction situations.

Large-scale distortions of the jet interface occur at both combustor pressures examined in this work, and are characterized by a Strouhal number of 0.002 to 0.005. These Strouhal numbers are two orders of magnitude smaller than those associated with large-scale instabilities in single-phase jets. Exhaust nozzle geometry may have an effect on Strouhal number, and exhaust jets emanating from projecting nozzles appear to display higher Strouhal numbers, since the projecting geometry allows the lower boundary of an emerging bubble to develop a rounded surface.

Evidence is presented that indicates that the interface may be affected by instabilities linked to the effect of acoustic pressure waves on the jet interface. This type of instability is not present in single-phase jet interaction, and would be similar to the effect of shockwaves on interfaces in Richtmyer-Meshkov instability. Pressure-wave interaction may be involved in the dynamics of baroclinic instability at the interface, since an increase in combustor pressure increases the sound pressure levels of frequencies in the sound spectra associated with the two-phase exhaust flow, and flows observed at an increased upstream pressure are surrounded by thicker clouds of small gas bubbles, which appear to have been forced through the interface into the liquid phase. The presence of combustion also produces an increase in the sound pressure levels associated with almost every frequency in the spectrum, compared with a nonreacting flow emerging at the same combustor pressure, and the resulting exhaust jet is surrounded by very thick clouds of bubbles. However, the heated exhaust jet may also promote instability by initiating local vaporization of water and by reducing the viscosity of water at the jet interface. The density of the heated exhaust jet is also lower than that of an unheated exhaust jet at the same combustor pressure, and this will tend to make the interface inherently more unstable.

7.2 Recommendations for Future Work

7.2.1 Future work on Swirl-Stabilized Spray Flames

The fundamental issues dealt with in this investigation are quite broad, and more work could be done in a number of areas associated with this research. The structure of swirling spray flames at higher pressures, and at a wide range of thermal loads, should be investigated to determine if the trends observed above also apply. The effects of flame structure and flow parameters on combustion completeness and flame chemistry are also of interest, and this question was not addressed directly in the work described above. For instance, emissions associated with swirl-stabilized flames, examined at a range of pressures, and using a variety of swirl configurations, would be of considerable interest. Combustion instability is also an important phenomenon. The potential for unstable combustion in a pressurized, swirl-stabilized system of the type described in this work should be investigated, particularly since unstable, liquid-fuelled, pressurized combustors have not been studied extensively. Other fuel types and fuel atomization gases should also be examined, at a range of pressures, in order to explore new methods to control combustion instability.

7.2.2 Advanced Diagnostic Techniques

Further diagnostic techniques can also be applied to the optically-accessible flame. PLIF (planar laser-induced fluorescence) imaging can provide detailed information about species distributions in the reacting flow, and may help develop combustor geometries that will provide complete combustion with fewer emissions. The PIV technique described above is quite powerful, but is still not able to fully characterize a reacting, two-phase flow containing a fuel spray. The development and application of a new PIV algorithm, capable of separately tracking the fuel and gaseous phases in the flame, could provide essential information about the detailed behavior of the reacting flow. The thermal field in a spray flame is also difficult to characterize with the present technology, but it may be possible to use spectroscopy techniques based on Rayleigh scattering or thermal imaging to obtain this information.

7.2.3 Instabilities and Dynamics of Two-Phase Exhaust Jets

The instabilities affecting the two-phase exhaust jet are extraordinarily complex, and much more work needs to be done to really understand the nature of the events at the phase interface. New diagnostic techniques are necessary here, as well. Small probes, inserted into the two-phase flow, might provide useful information about the frequency and scale of the instabilities. The frame rates used to image the interface in the present work were relatively low. Further studies, using far higher frame rates, and focusing on a much smaller area of the interface, will also help characterize the instabilities. The fundamental effect of fluid properties, particularly viscosity, temperature, and density, on the interface dynamics of the exhaust jet should also be investigated.

The potential for linked instabilities, occurring in both the combustor and the two-phase region surrounding the exhaust jet, is also quite interesting. If the pressure drop across the exhaust nozzle is low, and the exhaust jet is not choked, it may be possible for an unstable mode of the combustor to become synchronized with the unstable condition of the exhaust jet. Means of amplifying or controlling this interaction may be central to any future attempt to develop and operate submerged combustors.

Each of these areas should really be addressed individually. Interestingly, however, they can all be examined in the context of submerged combustion, using equipment and facilities developed for the present work.

Appendix A: Construction of Twisted-Vane Swirl Assemblies

A.1 Construction of Twisted-Vane Swirl Assemblies

The effects of swirl flow are known and have been appreciate for many years. Some of these effects can be undesirable like tornadoes but, in the case of combustion, the swirl can stabilize and increase the efficiency of the flame. In order to be able to compare and characterize different swirl flows, a number without dimension: the Swirl Number (S). S equals $\frac{\text{Angular Momentum Flux}}{\text{Axial Momentum Flux} \times \text{Radius}}$. In the case of gas turbine combustor or rocket engine, the velocity and the mass rate of the flow is so important that the flame can goes away, and as a consequence, extinguish the flame. To prevent that, a recirculation zone is created by a swirl flow. This can only happen when the amount of swirl is high (S>0.4).

Some previous swirlers have been made of brass during the 90s. The blades were too thin so that they get partially destroyed. As a matter of consequence, the airflow coming out the swirler is not anymore symmetrical. The flame drastically changes and becomes no more consistent from one experiment to the other. No notice was available to rebuild them, and no one understands how they have been made. So a new way of manufacturing new swirlers has been set up. The relevant steps of the conception of the new swirlers are developed in the following part. Figure i) shows a side view of the burner geometry and the kind of geometry we have for the inner and outer swirlers.

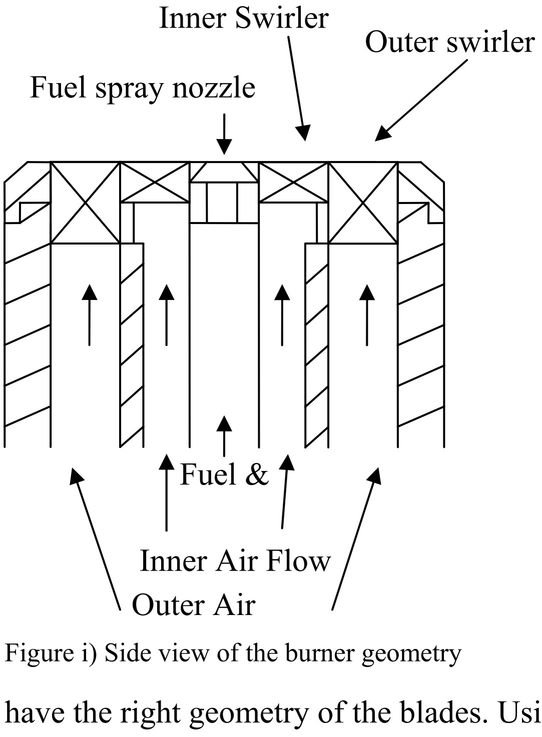

Figure i) Side view of the burner geometry

Accuracy has always been a real target. In fact, we have to assemble two different set of swirlers (the inner and the outer ones). If we want them to fit perfectly together, the tolerance has to be around 0.001'' or 25μm. This represents the limit of the machine-tool technology used. So during all the machining process, we had to hold the tolerance on the order of 25μm. The other reason to explain why a such accuracy was ask is that, the air flow profile can change drastically when there are flaws in the swirlers. Consistency from one experiment to another one is in fact a very important notion. So data and results shouldn't depend on the day there are taken.

The swirlers are made of aluminum and are manufactured with lathes and mills. Settings have to be found in order to have the right geometry of the blades. Using a lathe, a cylindrical piece is manufactured at the right dimension within 0.001'' (25μm). The angle of the blades is important to be known. This will enable to make some comparisons to others experiments with the previous swirlers which were manufactured in the lab. The blades are manufactured using a mill and a rotational step motor, shown in Figure ii). The angle is defined from the vertical line at the outside border of the aluminum cylinder. It can be deduced from a simple trigonometric calculation. So that, the angle of the blades is determined with the rotational step (1.8° minimum) and the step forward of the mill table. Due to the way they are machined, the blades are not straight but curved. The angle of the blades increases when the radius increases.

As the thickness of the blades was a weakness of the previous swirlers, the target is here to have the more stable blades as possible. This will be the result of parallelepiped blades. The thickness of the blades should be constant when the radius increases. So they won't tend to change geometry during the experiments and the flow will be and stay symmetrical.

The amount of aluminum to remove is not the same at the outer and the inner diameter. A conical endmill could be use, but its angle and depth would depend on the thickness of the blades and on the mean diameter of the swirler (inner or outer). That is the reason why we changed our mind and decided to use a straight endmill. As the Figure iii) below shows, using a straight mill is possible if we cut a face of the blade at each pass. So there are two passes to be done.

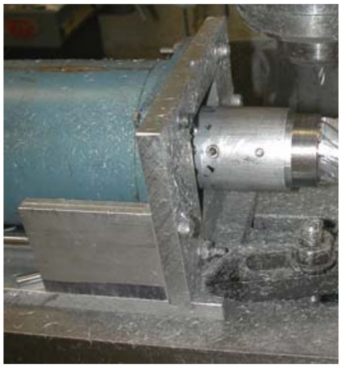

Figure ii) Picture of the stepper motor on the mill table

All the sources of error or inaccuracy had to be listed. Solutions have been found in order to minimize their effects on the finished swirlers. The step motor has been equipped with an assembly of aluminum plates. This device enables the step motor to be perfectly aligned with the axis of the mill table. This is a very important step to be sure that each time we use the mill, that the step motor is perfectly aligned. Some strain problems appeared during the manufacturing, so that some blades were broken and the accuracy was not high enough. This was solved by changing the order of machining operations.

In order to obtain the curved blades with the right angle, a successions of little step forward and rotational step have to be done. Experiments implies, as shown on the previous Figure iii), that the endmill is off-centered from the cylinder. An empirical relationship has been found between this offset and the number of rotational step taken at the beginning of each pass. The offset equals the number of step times the radius times the rotational angle (radians). Tests have been made to check the efficiency of the process.

Seven different kind of swirler have been manufactured. The different settings are summarized in tables below.

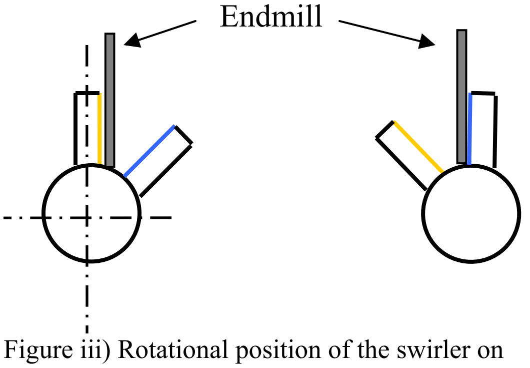

Figure iii) Rotational position of the swirler on the endmill when cutting the ▬ face (left) and the ▬ face (right)

Inner Swirlers	Tool used : endmill	Number of steps	Offset	Step forward
30°	1/8	8	0.094	+0.042
45°	1/8	7	0.082	+0.025
60°	1/8	3	0.035	+0.014
0°	Conical 30°	-	-	-

Figure iv: Settings used to machine the inner swirlers

Outer Swirlers	Tool used : Endmill	Number of steps	Offset	Step forward
30°	9/32	6	0.1535	+0.042
60°/-60°	1/8	5	0.1280	+0.014

Figure v: Settings used to machine the outer swirlers

A.2 Process of Machining an Inner Swirler

Example: 30° Inner Swirler

Aim of the process:

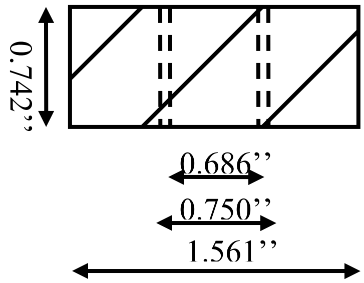

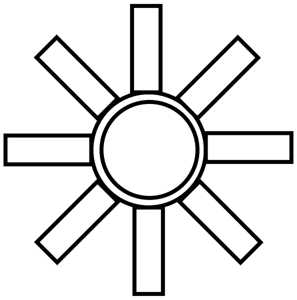

Step 1:

Machine a cylindrical piece of aluminum which has the following dimensions, this becomes the blank:

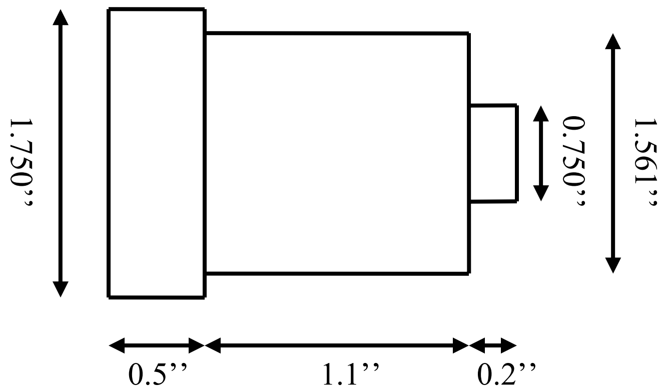

Step 2:
With an endmill, machine a keyway on the bigger diameter, about 0.2 in large.
Step 3:
Put the blank in the indexer so that the set crew will sit on the keyway. This will prevent the blank to move relatively to the indexer.
Step 4:
Set up the indexer: Align with axis of table using a square fixture and two rail pins. Use the front edge of the indexer for alignment. Clamp down the indexer tightly; both front and back!
Step 5:
Insert an aluminum blank into the indexer. Use the blank-set-screw to fix the blank in the sleeve. Use an allen-wrench.
The blank dimensions must be:
Small diameter: 0.750 inches
Large diameter: 1.561 inches
Step 6:
Use the indexing pin to index the first position. Tighten the shaft-set-screw.

Step 7:
Insert the 3/8ths edge-finder into the mill. Center the relevant mill axis on the blank axis.
The diameter of the small segment of the edge finder is 0.200 inches
Thus, the radius must be 0.100 inches; this radius must be accounted for during zeroing.
Step 8:
Install a 1/8 inch diameter (or: 0.125 inches) carbide, two-flute mill end into the mill.
Step 9:
Zero the other mill table axis so that the carbide mill end just barely fails to touch the face of the blank.
Step 10:
Make sure that the index pin is REMOVED! Now, rotate the blank counterclockwise EIGHT steps, using the indexer. This will create a rotation of 14.4 degrees.
Step 11:
Move the mill 0.094 inches from the center axis of the blank.

Set the mill end on the small diameter of the blank so that the corner of the mill end is just touching the smaller diameter surface.

Step 12:

Turn on air and lubrication on the mill end (involves help from an assistant, or an automated device for this purpose)

Step 13:

Turn on the mill in high gear; set the mill for 4000 rpm.

Step 14:

Cut the first pass; taking steps of 0.042 inches laterally.

Step 15:

Pull up the endmill.

Step 16:

Rotate one indexer step so 1.8°.

Step 17:

Pull down the endmill slowly while removing some materials.

Step 18:

Repeat step 14 to 17 as many time as needed.

Step 19:

Once the first pass is finished (when the mill begins to cut the largest diameter of the blank) turn off the mill. NOTE: The current lateral position of the mill!! All other passes will be just the same length.

Step 20:

Raise the quill out of the groove; return to lateral zero.

Step 21:

Loosen the shaft set screw; return the indexer to the first position!

Tighten the shaft set screw.

Remove the index pin!!!!

Step 22:

Rotate the blank 8 steps (or 14.4 degrees) in the clockwise direction.

Move the mill to -0.094 inches off the blank axis. Note that you move in the positive direction this time.

Lower the mill end until the corner just touches the smaller blank diameter.

Step 23:

Turn on air and lubrication on the mill end (involves help from an assistant, or an automated device for this purpose)

Step 24:

Turn on the mill in high gear; set the mill for 4000 rpm.

Step 25:

Cut the second pass; taking steps of 0.042 inches laterally, rotating one indexer step each time.

Step 26:

The second pass is complete when the same lateral direction has been obtained as was obtained on the first pass. The first groove is now complete.

Step 27:

Raise the quill out of the groove; return to lateral zero.

Return also to off-axis zero.

Step 28:

Loosen the shaft set screw, move the indexer to the second position.

Tighten the shaft set screw!

Remove the index pin!!!!

Step 29:

Make sure that the index pin is REMOVED! Now, rotate the blank counterclockwise eight steps, using the indexer. This will create a rotation of 14.4 degrees.

Step 30:

Move the mill 0.094 inches from the center axis of the blank.

Set the mill end on the small diameter of the blank so that the corner of the mill end is just touching the smaller diameter surface.

Begin to cut passes for subsequent grooves, repeating previous steps as necessary.

Step 31:

When all the 12 blades have been machined, remove the blank from the indexer.

Step 32:

Center the blank in a lathe.

Step 33:

Use a templing tool to clean the edge of the blades. Orient it such a way that a really sharp part of the tool will cut a part of the blade. Use also a high rotational speed for this operation, around 1300 rpm if it is possible.

Step 34:

Put the blank on a wise with a machining square block on a mill table. This enables to be perfectly aligned with the bigger diameter because the bottom plan of the blank is not perfectly flat.

Step 35:

With the rotational blade on the mill, we cut 0.775 inches at 800 rpm. This corresponds to: 0.742’’ (depth of the swirler we need) + 0.280’’ (thickness of the blade) + 0.004’’ (thickness of the sheet paper used to set the depth).

Step 36:

Finish the cut of the swirler with a very thin metal hand saw blade.

Settings used for the Inner Swirlers:

	Tool used : endmill	Number of steps	Offset	Step forward
30°	1/8	8	0.094	+0.042
45°	1/8	7	0.082	+0.025
60°	1/8	3	0.035	+0.014
0°	Conical 30°	-	-	-

A.3 Process of Machining an Outer Swirler

Example: 30° Outer Swirler
Aim of the process:

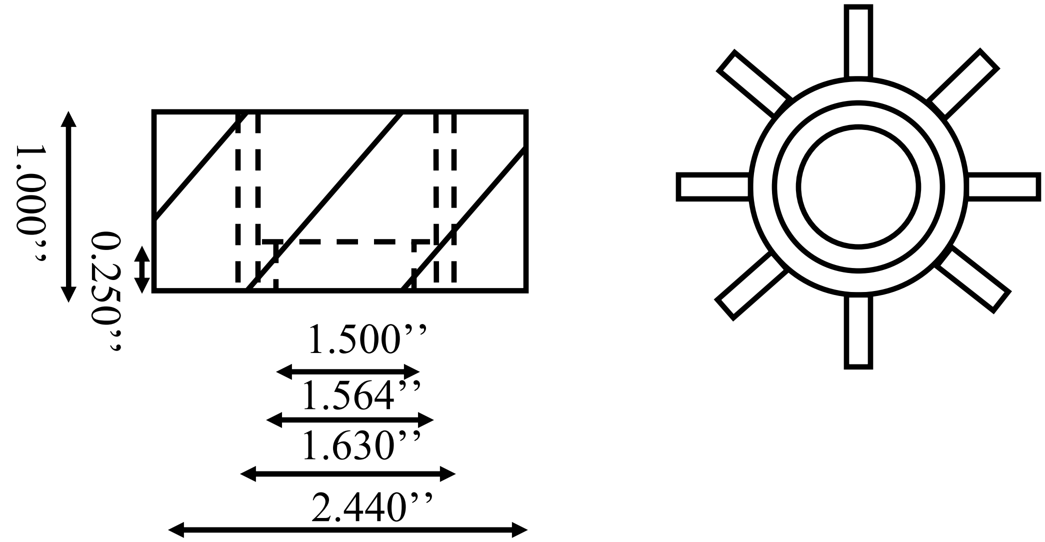

Step 1:
Machine a cylindrical piece of aluminum which has the following dimensions, this becomes the blank:

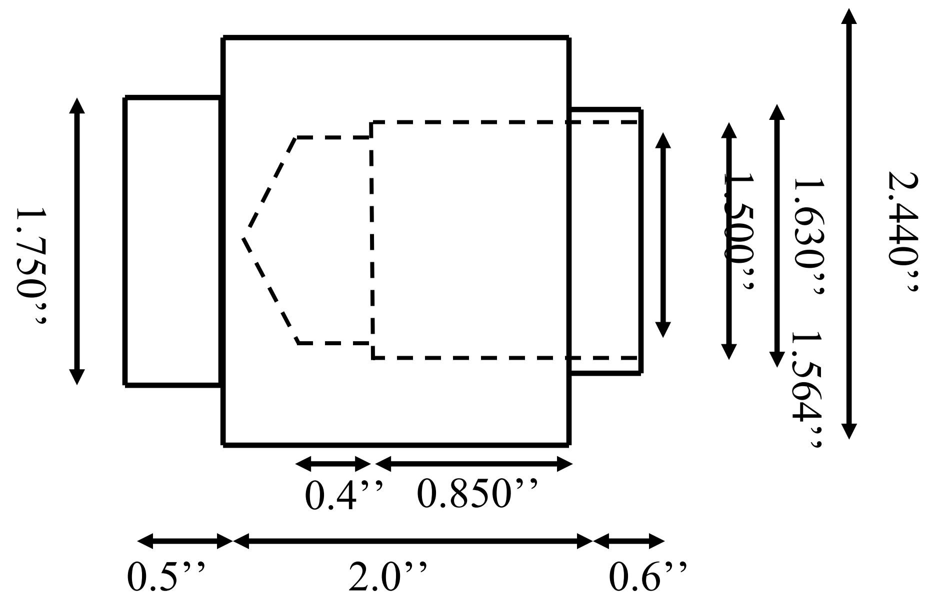

<u>Steps 2 to 7:</u>
Identical to those used for the inner swirler
<u>Step 8:</u>
Install a 9/32 inch diameter (or: 0.28125 inches) carbide, two-flute mill end into the mill.
<u>Step 9:</u>
Zero the other mill table axis so that the carbide mill end just barely fails to touch the face of the blank.
<u>Step 10:</u>
Make sure that the index pin is REMOVED! Now, rotate the blank counterclockwise SIX steps, using the indexer. This will create a rotation of 10.8 degrees.
<u>Step 11:</u>
Move the mill 0.1535 inches from the center axis of the blank.
Set the mill end on the small diameter of the blank so that the corner of the mill end is just touching the smaller diameter surface.
<u>Steps 12 & 13:</u>
Identical to those used for the inner swirler
<u>Step 14:</u>
Cut the first pass; taking steps of 0.042 inches laterally.
<u>Steps 15 to 21:</u>
Identical to those used for the inner swirler
<u>Step 22:</u>
Rotate the blank 6 steps (or 10.8 degrees) in the clockwise direction.
Move the mill to -0.1535 inches off the blank axis. Note that you move in the positive direction this time.
Lower the mill end until the corner just touches the smaller blank diameter.
<u>Steps 23 & 24:</u>
Identical to those used for the inner swirler
<u>Step 25:</u>

Cut the second pass; taking steps of 0.042 inches laterally, rotating one indexer step each time.

Steps 26 to 28:

Identical to those used for the inner swirler

Step 29:

Make sure that the index pin is REMOVED! Now, rotate the blank counterclockwise six steps, using the indexer. This will create a rotation of 10.8 degrees.

Step 30:

Move the mill 0.1535 inches from the center axis of the blank.

Set the mill end on the small diameter of the blank so that the corner of the mill end is just touching the smaller diameter surface.

Begin to cut passes for subsequent grooves, repeating previous steps as necessary.

Step 31:

When all the 12 blades have been machined, remove the blank from the indexer.

Step 32:

Center the blank in a lathe.

Step 33:

Use a templing tool to clean the edge of the blades. Orient it such a way that a really sharp part of the tool will cut a part of the blade. Use also a high rotational speed for this operation, around 1300 rpm if it is possible. Cut the blank with the templing tool until the previous depth of 0.850'' becomes 0.750''.

Step 34:

Put the blank on a wise with a machining square block on a mill table. This enables to be perfectly aligned with the bigger diameter because the bottom plan of the blank is not perfectly flat.

Step 35:

With the rotational blade on the mill, we cut 1.0365 inches at 800 rpm. This corresponds to: 1.000'' (depth of the swirler we need) + 0.320'' (thickness of the blade) + 0.0045'' (thickness of the sheet paper used to set the depth).

Step 36:

Finish the cut of the swirler with a very thin metal hand saw blade.

Settings used for the Outer Swirlers:

	Tool used : Endmill	Number of steps	Offset	Step forward
30°	9/32	6	0.1535	+0.042
60°/-60°	1/8	5	0.1280	+0.014

Appendix B: Some of the Relevant Papers Published by the Author

Appendix B.1.

Linck, M., Gupta, A. K., “Control of Forced Combustion Instability in a Swirl-Stabilized Spray Combustor via Swirl and Airflow Distribution”

Accepted for Publication, J. Propulsion and Power, 2006 (in press).

Passive Control of Forced Combustion Instability in a Swirl-Stabilized Spray Combustor

M. Linck and A. K. Gupta*

The Combustion Laboratory

University of Maryland

Department of Mechanical Engineering

College Park, Maryland 20742

*e-mail: akgupta@eng.umd.edu

Abstract

A co-annular swirl-stabilized burner, equipped with a pulsation mechanism to introduce controlled periodic instability into the fuel flow to the nozzle, was used to examine instability mechanisms and demonstrate passive control of combustion instability. The effects of swirl configuration and airflow distribution on forced, unstable combustion were examined. Fuel pulsation was used to excite a dynamic response from the combustor that would mimic the behavior of instabilities encountered in many commercial, military and industrial systems. The response of a spray flame to pulsations of different frequencies was examined using a sound spectrum analyzer and particle image velocimetry. The effect of swirl distribution in the burner, including co- and counter-swirl distribution, on the amplitude response of three different flames to low-frequency fuel pulsation was examined. An analysis of the flame structure at different points during the cycle of a forced, low-frequency instability is presented for three swirling spray flames. The effect of airflow distribution on the dynamic response of one flame obtained with a particular swirl configuration is presented. Changes in swirl distribution, which affected recirculation and mixing, were found to reduce the magnitude of the flame response to forcing. Changes in airflow distribution, which affected residence times of product gases in the combustion region, were also found to reduce the combustor response to forcing. Changes in swirl and airflow distribution in a burner of this type were shown to provide effective passive control of combustion instabilities.

Introduction

Instabilities in combustors develop when cyclical heat-release mechanisms in the combustor become coupled to some characteristic frequency of the combustor. Often, this is the Helmholtz frequency of the combustor, although other components of the combustion system, such as the inlet duct or the exhaust duct may also be important in determining the frequency of the instability[1]. Once unstable combustion develops, both the heat release and pressure in the combustor will fluctuate periodically. The coupling of the heat release mechanism with the characteristic frequency of the combustor must meet the Rayleigh Criterion[2] in order to drive the instability. The Rayleigh Criterion requires that the cyclical heat release must oscillate with a period that is similar to the period of the pressure fluctuation, and is nearly in phase with it. Oscillations may occur on a large range of timescales, but only those corresponding to natural acoustic frequencies of the combustor will be amplified. If the curves are out of phase, the amplitude of the instability is likely to remain small.

The dominant frequency involved in unstable behavior depends on the combustor geometry, and on the resonant frequencies of equipment associated with the combustor. The possible frequencies depend on the local speed of sound in a given component, and each component has multiple acoustic modes[1]. Since acoustic waves can propagate in up to three dimensions in each component, it is difficult to predict which frequency is most likely to be associated with combustor instability in a particular system. Unstable combustion can be readily characterized via the sound spectrum emitted by the combustor. Frequencies represented in the sound spectrum are associated with the turbulent mixing in the flow, and peaks in the spectrum indicate that turbulent events occur at particular frequencies that drive mixing and combustion in the system[3]. The sound spectrum of an unstable combustor is generally dominated by the frequency of the instability, and this frequency will have an associated sound pressure level many orders of magnitude greater than that of the other frequencies in the spectrum[1].

In order for instability to be driven, oscillations in pressure due to acoustic resonance in the combustor must be linked to heat release from the combustor. Usually, the mechanism depends on interaction between the oscillating pressure in the combustor and the evolution and breakdown of turbulent structures involved in combustion. Gutmark and Schadow[4] illustrate this point in a review on the nature and control of flame instabilities. Their analysis of unstable gas-fueled dump combustors describes the role of vortex behavior in the development of instabilities. Vortical structures in the combustor form and break down in a cyclical fashion, which causes mixing between fuel and oxidizer, and the associated heat release, to increase and decrease cyclically.

Turbulent events and turbulent structures occur over a wide range of temporal and spatial scales in any turbulent flow, and determine the rate of mixing between fuel and oxidizer in a combustor. Since the heat release rate is affected by the phenomenon of mixing, the dynamic heat release in the combustor is linked to the timescales of turbulent mixing events occurring in the combustor[4]. When the timescale of a particular turbulent event matches the timescale of an acoustic mode in the system, the evolution and breakdown of a particular turbulent structure may become synchronized with the oscillation in pressure in the combustor. The turbulent structure in question depends on the flow. In a burning jet the instability may be linked to the shedding of vortices at the jet boundary[5]. In a dump combustor or bluff-body stabilized combustor, the instability may be linked to oscillations in the size and location of the recirculation region, even though vortices are not shed[1]. The unsteady heat release in the combustor can then drive instabilities, as long as it is sufficiently in phase with a characteristic frequency of the combustor. If the turbulent structures affecting heat release in the flame can synchronize effectively with an acoustic mode, unstable combustion can occur.

The objective of the present investigation is to examine the dynamic response of unconfined swirl-stabilized flames, fuelled by kerosene, to periodic changes in the equivalence ratio, leading to unstable flame behavior. Controlled, periodic variation of the equivalence ratio is achieved via pulsation of the fuel supplied to the flame. The global flame features associated with each operating condition are examined, and are related to features of the recirculation region in the combustion air flow. Specific effects of swirl configuration and airflow distribution on the dynamic response of the flame are discussed, in order to identify flame features and frequencies that are likely to be linked to unstable combustion, and in order to illustrate practical strategies for passive combustion control.

Passive Control of Instabilities

Due to the role played by large-scale vortical structures in the development of combustor instabilities, considerable work has been done to disrupt the formation of these structures. Instability can be avoided if the turbulent events affecting mixing and heat release in the flow can be altered in such a way that events associated with instability cannot dominate the rate of heat release.

Passive control of combustion instabilities depends on alterations in the combustor that do not actively respond to the onset or amplification of unstable behavior. An example of this type of modification in a dump combustor is described by Schadow, et al.[6]. A similar modification of a swirl-stabilized combustor is described by Paschereit and Gutmark[7]. In both cases, the geometry of the combustor was altered to introduce fine-scale turbulence into the flow, ensuring that mixing and heat release occurred on timescales other than those associated with large, vortical structures. In the dump combustor, combustion was stabilized by the installation of a series of small steps, rather than a single large one[6]. In the swirl-stabilized combustor, small vanes were installed at particular points, in order to change the behavior of the local boundary layer and create small-scale turbulence in certain regions of the flow[7]. Both approaches are examples of passive instability control. Both studies show that the amplitude of the instability was controlled, since the unstable features of the flow could not effectively synchronize with an acoustic mode in the system once the modifications to combustor geometry were made[6,7].

The use of non-circular or modified nozzles has also been examined to strategically control the behavior of large-scale vortical structures in combustors. Gutmark and Grinstein[5] provide a comprehensive review of the work done on non-circular nozzles. The most important observation is that nozzles with varying radii of curvature along their perimeter (such as rectangular nozzles, for example) produce different turbulent flow structures in different regions of the flow. Sides of the nozzle that are straighter, and have large radii of curvature, produce larger vortical structures. Regions where the radius of curvature is small create small, high frequency vortical structures. This phenomenon is of particular interest, since instabilities in combustors are often linked to the dynamic behavior of large vortical structures, which break down into fine-scale turbulence in a cyclical manner, releasing heat and driving oscillations. Since non-circular nozzles seem to promote both large and small-scale turbulence, these nozzles can be used to promote mixing on a range of spatial and temporal scales, altering or eliminating unstable combustion[5].

Hu, et al.[8] investigated the addition of mechanical tabs that protrude out into the flow at the exit of the nozzle to increase mixing of the flow in jet engines. These tabs were designed to cover approximately 1.5% of the exit area of the nozzle. The mechanical tabs produced small vortices, whose size was dependent on the tab dimensions, at the exit of the nozzle. Small-scale turbulent structures appeared further upstream in the flow when tabs were present, indicating that the addition of the tabs destabilized the interface between the jet and surrounding fluid, and promoted mixing over an expanded range of turbulent scales[8].

Combustor instability may also be linked to changes in inlet equivalence ratio. Steele and Cowell[9], working in conjunction with Smith and Cannon[10], present an experimental and analytical approach to stability control that incorporated a dynamically varying inlet equivalence ratio. Heat release is a function of equivalence ratio in the combustion zone; if the mixture becomes too lean or too rich, the adiabatic flame temperature of combustion decreases. If the equivalence ratio moves toward unity; near stoichiometric combustion, the combustion temperature at the flame front rises[3]. Based on the work of Richards and Janus[11], Steele and Cowell modeled an experimental combustor as a Helmholtz resonator during unstable combustion, and determined the most likely frequency of unstable combustion. They observed that the airflow rate into the combustor will become unsteady when the pressure in the combustion chamber pressure oscillates. If one assumes that the fuel flow rate is unaffected by the combustor pressure oscillations (as is often the case in practical systems, where fuel is delivered at very high pressure[12]), it becomes clear that the equivalence ratio of the air-fuel mixture entering the combustor will also become a function of time, since the proportions of air to fuel will be altered by the oscillatory behavior of the combustion airflow rate. The location of the fuel injector in the mixing plenum can then be adapted so that, when the instability develops, the fuel enters the combustion chamber in a manner that is out of phase with the instability[10,11]. To control the instability, the injector is located so that, when the oscillatory pressure nears its peak amplitude in the combustor, and the airflow rate drops, the resulting accumulation of fuel does not reach the combustor until the pressure in the combustor has decreased back to the minimum value. If the fuel always arrives at a point in the instability cycle when the combustor pressure is reduced, the instability will be effectively damped[9]. Experimental work confirmed that combustion instability was successfully controlled via this approach[9,10].

A very similar approach is described by Lubarsky and Levy[13]. They show that an effervescent spray injection system can control instability when correctly configured. The liquid-fueled ramjet combustor used in their study incorporated a low-pressure effervescent atomizer. In a standard pressure atomizer, the liquid fuel is converted into a spray when it is forced at high pressure through a small orifice, into a region of much lower pressure[12]. Effervescent atomizers force air bubbles into the fuel in a small mixing chamber upstream of the final orifice. The pressure drop across the orifice is lower than that for pressure atomizer, but the gas bubbles in the fuel stream destabilize the stream, effectively atomizing the fuel. Since an effervescent atomizer operates at a relatively low pressure drop, the amplitude of the pressure signal from the combustor instability represents a considerable fraction of the total pressure drop across the atomizer. Thus, the amount of fuel atomized can change dramatically in response to the pressure changes in the combustor. If this pulsating component of the total fuel fed to the combustor is sufficiently large, and sufficiently out of phase with the signal from the combustor, the combustion instability in the combustor will be damped[10].

Unstable combustion can be affected by the turbulent features of the flame, the acoustic modes of the combustion system, and changes in equivalence ratio that become linked with the instability. The present study examines the effect of these parameters on the unstable behavior of a turbulent, swirl-stabilized spray flame.

Swirl stabilization of combustion is a common technique, widely applied in practical combustion systems as described by Gupta, et al.[14]. If rotation is imparted to a flow, it can be characterized by a swirl number, S, which provides a comparison of rotational momentum and axial momentum. If the swirl number at the inlet to a combustor is greater than a critical number of approximately 0.6, vortex breakdown occurs at the center of the flow, and a toroidal recirculation region is formed, resulting in flow recirculation. Flames are commonly stabilized at the surface of the recirculation region, where fresh fuel and oxidizer mixes with the hot recirculating product gases[14]. Multiple concentric air annuli, each featuring a particular swirl number, can be employed to shape the features of the flow and flame[15]. The resulting flow displays complex turbulent behavior over a wide range of scales, and modeling of flows of this type is difficult[16]. Due to the complexity of the flow, it is also difficult to predict the possible unstable behavior of the flame. However, swirling flows can be manipulated to create desirable flame features. Linck, et al.[17], have shown that the interaction between a fuel spray and the flow can be altered by changes in the swirl conditions and flow features of the combustion air. Linck et al.[18,19] and Gupta and Linck[20] have also shown that the geometry and stability characteristics of the flame can be altered dramatically by changes in the swirl conditions introduced into the flow.

New analytical techniques, which will help to develop an understanding of combustor instabilities, are also being developed. For example, a new particle image velocimetry (PIV) technique, capable of overcoming the challenges inherent in examining the behavior the flowfields of luminous flames, has recently been introduced[21]. PIV in luminous reacting flows using CCD detectors is problematic, since the second image in an image pair tends to be overexposed. The new method utilizes narrow band-pass filters and mechanical shutters to ensure consistent illumination of the detector[21]. Linck and Gupta[22] show that the technique can be applied to examine the flowfield of the fuel spray in highly luminous swirl-stabilized kerosene flames.

Passive control of combustion instabilities in swirl-stabilized flames is also described by Conrad, et al[23] using n-heptane as the fuel. The fuel was atomized by tangentially-entering combustion air in a primary air duct. The swirling air-fuel mixture, with entrained fuel droplets, exited this primary duct, and was brought into contact with swirling air exiting a secondary air duct. The outer, secondary air swirled in the opposite direction, creating a counter-swirl condition. A quartz tube was fitted around the flame, and extended downstream. In non-reacting cases, examined without the quartz tube enclosure using a phase-Doppler particle analyzer (PDPA), the investigators showed that one could alter the structure of the spray by changing the amount of air fed through the inner and outer ducts. They also examined the heat release signature of the enclosed flame using a photomultiplier tube detector tuned to the light emission frequency of the CH radical. They found that the dominant unstable modes associated with the heat release signal from the flame could be shifted slightly in frequency by changes in the airflow distribution. The amplitude of the peak instability and the fuel spray structure could be affected dramatically by changes in airflow distribution between the primary and secondary ducts[23].

Conrad, et al.[23] showed that the flowfield has an effect on the dynamic response of a liquid fuelled spray flame. However, since they used a tangential-entry system to feed combustion air to their flame, the exact swirl distribution at the inlet of their burner was unknown. This situation complicates analysis and modeling considerably. Also, since their configuration examined only the behavior of flames in counter-swirling flows, it would be useful to examine the behavior of flames in co-swirling flows, where the air from each annulus rotates in the same direction. The flames examined by Conrad et al. displayed instabilities above 400 Hz; however, instabilities at much lower frequencies are often present in practical combustion systems, driven by characteristic frequencies of large components[1]. The introduction of a forcing signal, driving an unstable response from the flame, can help clarify the effect of swirling flow parameters on the dynamic response of the combustor. Conrad et al. investigated a single-component fuel[23]. Real fuels, such as kerosene or Jet-A are composed of large mixtures of compounds, featuring a wide range of properties. Fuel droplets composed of mixtures vaporize differently than do single-component fuels[24,25] and this may affect the dynamic behavior of the flame. Conrad et al. investigated a flame featuring a very fine fuel spray with a Sauter mean diameter of approximately 17 microns[23]. Practical liquid-fuelled combustors generally feature fuel sprays with much larger droplet diameters, on the order of 50 microns[12]. Larger droplets are not entrained as readily, and this effect may alter the unstable response of the flame. The current investigation addresses these issues directly.

Experimental Facility and Conditions

In order to provide good control of the swirl and airflow distribution, a burner featuring two co-annular air ducts was equipped with swirl vane assemblies at the outlets. A schematic diagram of the burner used is shown in Figure 1. The co-annular air ducts fed combustion air to the flame, and an air-assisted atomizing fuel nozzle, located at the centerline, was used to disperse the fuel. The air-assisted nozzle used a high-speed swirling stream of atomizing air to destabilize the fuel jet, creating a fine spray. Nozzles of this type have found wide practical application in combustion systems, and provide effective atomization over a wide range of fuel flowrates[12]. Since the swirl characteristics of the flow could be adjusted at will, both co- and counter-swirl flames were examined, to determine their on the dynamic response of the flame. The dynamic pressure signal from the flame was examined via the sound pressure level (SPL) spectrum of each flame. In order to excite a large-amplitude unstable response from the combustor, a forcing signal was introduced at frequencies between 10 and 250 Hz. This signal consisted of a periodic interruption of the fuel flow upstream of the fuel nozzle, and hence, a periodically-oscillating fuel flow rate and equivalence ratio at the nozzle. The introduction of a forcing mechanism allowed one to examine the flame response to a range of instability frequencies.

The swirl assemblies in the air annuli featured straight swirl vanes. Straight swirl vanes have a vane angle that does not vary with radial location. The swirl number, *S*, of a straight-vane swirl assembly can be approximated[14] as:

$$S = 2/3 \cdot \left[\frac{1-\left(d_h/d_o\right)^3}{1-\left(d_h/d_o\right)^2} \right] \cdot tan(\theta) \qquad (1)$$

where, d_h is the hub diameter of the swirler, and d_o is the outer diameter of the swirler. Thus the swirl number is found to depend primarily on θ, the swirl vane angle. Swirl vanes featuring angles greater than 70° from the burner centerline cannot usually be employed in practice. In this study the inner swirlers featured swirl angles of 30° and 45° degrees from the vertical centerline of the burner. The outer swirlers featured swirl angles of 50° and –50°. The swirlers used and the respective calculated swirl numbers, are shown in Table 1. The sign of the swirl number indicates the swirl sense; positive swirl numbers indicate clockwise rotation (looking into the burner from the top), while negative swirl numbers indicate counter-clockwise rotation.

Swirler Type	Swirler Vane Angle	Swirl Number
Inner	30°	0.385
Inner	45°	0.667
Outer	50°	0.795
Outer	-50°	-0.795

Table 1: Swirl Numbers of swirl vane assemblies

A mean fuel flow rate of 0.5 gallons per hour was fed through the fuel nozzle. An atomization air flow rate of 0.25 SCFM (standard cubic feet per minute) was necessary to obtain the desired atomization of the fuel. Droplet sizes of approximately 50 microns were observed, and a solid-cone fuel spray, with an included angle of approximately 60° was produced. The fuel spray produced by the nozzle was characterized in previous investigations using a 2-D phase Doppler particle analyzer[17,20]. The PDPA technique is described in detail by Bachalo and Houser[26]. Properties of the fuel spray produced by the nozzle are presented in Figure 2. Since the fuel spray was affected by the surrounding air flow, the spray was examined under combustor swirl and airflow conditions representative of those employed in the spray flames that form the basis of this investigation. Data shown in Figures 2(a-d) taken at 30 mm downstream of the atomization nozzle exit show mean axial velocity, radial velocity, arithmetic mean diameter, and droplet number density in the spray, respectively, for both a non-reacting and combusting spray. The mean fuel droplet diameter was found to vary with spatial location within the spray, presence or absence of combustion, and the air flow parameters (airflow distribution and swirl configuration). The arithmetic mean diameter of the fuel spray obtained is representative of many fuel sprays in practical systems. Further details on the properties of the spray are given by Linck, et al[17].

Three different swirl configurations were employed here. Their characteristics are listed in Table 2. In the first configuration, the inner annulus swirl vane angle was 45 degrees while the outer annulus swirl vane angle was 50 degrees (both from the vertical axis of the burner). This is referred to as the 45°/50° swirl configuration. The second swirl configuration featured an inner swirl angle of 30 degrees, and an outer swirl angle of 50 degrees. This is referred to as the 30°/50° configuration. Both the 45°/50° and 30°/50° swirl configurations were co-swirling, meaning that the air from each duct rotated in the same direction. The third swirl configuration employed a counter-swirling configuration, with an inner annulus swirl vane angle of 30 degrees and an outer annulus swirl vane angle of –50 degrees. This counter-rotating configuration is referred to as the 30°/-50° configuration. The objective of this counter-rotating swirl configuration was to examine the effect of high-shear region formed between the inner and outer annulus air flows where the two counter-rotating flows interacted.

Swirl Configuration	45°/50°	30°/50°	30°/-50°
Inner Annulus Vane Angle	45°	30°	30°
Outer Annulus Vane Angle	50°	50°	-50°
Swirl Condition	co-swirl	co-swirl	counter-swirl

Table 2: Characteristics of swirl configurations

Initially, volumetric air flow rates of 14.3 SCFM were fed through each air annulus of the burner. This will be referred to as a 50%/50% airflow distribution, where the first and second percentages indicate the proportion of the total air fed through the inner and outer annuli, respectively. All three swirl configurations were initially examined using this airflow distribution. Further experiments were carried out on the 30°/-50° swirl configuration to determine the effect of airflow distribution using 25%/75% and 60%/40% airflow distribution in the burner. Particle image velocimetry (PIV) was used to examine the flow and recirculation regions associated with each swirl configuration under conditions of equal air flows (14.3 SCFM) in each annuli of the burner (i.e., 50%/50% airflow distribution). The recirculation regions were examined under airflow-only conditions; the fuel spray was not present during this phase of the experiment. The presence of the fuel spray make it difficult, if not impossible, to observe the motion of seed particles in the combustion air[27]. The inner and outer air streams were seeded with latex micro-balloons, and the flow was illuminated with a vertical laser sheet from a twin-cavity Nd:YAG laser system. The mean diameter of the micro-balloons was approximately 5 microns. The laser sheet was projected though the vertical central cross-section of the flow. Data on the flowfield characteristics were obtained at elevations between 8 and 45 mm downstream of the burner exit, and 39 mm on either side of the burner centerline. The PIV technique allowed measurement of three components of velocity, but only the mean axial velocity is presented here, since the recirculation region is of primary interest in analysis of swirl-stabilized flames. Mean velocities were obtained on the basis of 249 image pairs. Details of the PIV system used are given in Gupta, et al.[21].

Design of the Fuel Pulsation System

In order to introduce modulated pulsations into the fuel flow, all fuel to the burner was routed through a solenoid-operated automotive fuel injector, designed to respond to a threshold voltage of 3 volts. Figure 3 shows a schematic of the fuel delivery system. The fuel injector was installed in the fuel line upstream of the burner, and, when closed, interrupted the flow of fuel to the atomizing nozzle. When the necessary voltage was supplied, the solenoid valve in the injector opened; when this voltage was absent, the valve closed, and halted the flow of fuel through the supply line. In order to control the action of the valve, a signal generator was used to send a control voltage in the milliamp range to a solid-state amplifier. The amplifier then sent an amplified signal to the valve. The system, including the solenoid valve, was able to respond to signal frequencies between 0 – 1000 Hz. The shape of the solenoid valve flow curve could also be controlled by manipulating the voltage offsets of the control voltage; thus, in a given cycle, the solenoid valve could be open for varying periods of time. It was found that the flame responded best when the solenoid valve was open for 22% of a given cycle. If the solenoid valve was open for too large a portion of the cycle, the fuel line downstream of the solenoid valve damped out the oscillation, and no cyclical instabilities in the flame were observed. If the solenoid valve was open for too small a period during the cycle, the mean fuel flow rate dropped dramatically, requiring high fuel pressures upstream of the solenoid valve to maintain a mean fuel flow rate of 0.5 gallons per hour.

In order to obtain good data, it was necessary to bleed the entire fuel system. The mean fuel flow rate was adjusted manually, upstream of the solenoid valve. When the solenoid valve was cycled at a given frequency, the upstream fuel pressure was adjusted to maintain a constant mean fuel flow rate. Thus, the introduction of pulsation into the fuel flow rate was the only change in the conditions examined for each pulsation frequency in a given swirl configuration. The sound spectrum was obtained for each set of swirl and pulsation conditions using a sound-spectrum analyzer capable of performing a fast Fourier transform on the frequency signals transmitted by a microphone. The microphone was a piezoelectric detector located 241 mm from the combustor vertical centerline, and 50 mm downstream of the burner exit.

Results and Discussion

Global Flame Features without Fuel Pulsation

Flames observed with each of the three swirl configurations, with a 50%/50% airflow distribution, and a steady fuel flowrate of 0.5 gallons per hour, are shown in Figure 4. The 45°/50° configuration has the greatest inner swirl angle; this produces the broadest and longest flame. The size and shape of the flame is directly linked to the features of the recirculation region associated with this swirl configuration. The flames produced with the 30°/50° and 30°/-50° flames are more compact, since they are stabilized by smaller, narrower recirculation regions. The 30°/-50° flame appears to be larger than the 30°/50° swirl configuration, and the flame front on the surface of the recirculation region extends further upstream towards the fuel nozzle. This is attributed to more effective mixing in the counter-swirling air case. The recirculation regions examined via PIV in the airflow associated with each flame are now discussed.

Characterization of Recirculation Region

The airflow field associated with each set of operating conditions has a dramatic effect on flame behavior. The inlet swirl strength and swirl distribution associated with the flow is an important parameter, particularly when a recirculation region is formed. Combustion occurs at the interface between the recirculation region and the surrounding flow, where hot recirculating gases and vaporized fuel come in contact with oxidizer in the swirling combustion air streams. The features of the flame are closely related to the features of the recirculation region, and direct characterization of this recirculation region is essential to analyze the swirl-stabilized flame structure and dynamic behavior.

Figures 5-7 show mean axial velocity contours associated with the 45°/50°, 30°/50°, and 30°/-50° swirl configurations. The color scale in each figure relates the colors associated with each contour to the local axial mean velocity. All three figures show recirculation regions located downstream of the nozzle exit, over the burner centerline. In each figure, the origin of the coordinate system marks the fuel nozzle location.

The recirculation region associated with the 45°/50° swirl configuration, shown in Figure 5, is the largest of the three. This is to be expected, since this swirl configuration features the largest swirl number in the inner air flow. Negative axial velocities of up to –2.7 m/s are observed, and the recirculation region extends approximately 15 mm to either side of the burner centerline. The length of the recirculation zone extends upward in the axial direction beyond the examined region. This swirl configuration also produced the largest flame, as seen in Figure 4. Positive axial velocities, on the order of 2.3 m/s, are observed at the base of the recirculation region. These positive velocities are due to the effect of atomization air, which emanates from the atomizing nozzle. The atomization air jet opposes recirculation, and forces the recirculation region away from the fuel nozzle. As a result, the region is pushed downstream. This creates the slender base of the flames, just above the fuel nozzle, see Figure 4.

Figure 6 shows mean axial velocity contours associated with the 30°/50° swirl configuration. Since the swirl strength associated with this flow is smaller, the recirculation zone is smaller, and does not extend as far upstream or to either side of the burner centerline. The effect of the atomization air can be clearly observed; positive axial velocities are seen near the origin in Figure 6, and the recirculation region is prevented from extending upstream to the fuel nozzle. In the positive axial direction, this recirculation zone also extends beyond the measurement region. Maximum negative mean axial velocities of –3.0 m/s are seen in the center of the recirculation zone.

The axial velocity contours obtained for the 30°/-50° configuration are shown in Figure 7. The recirculation zone in this case resembles that seen in Figure 6. This is not surprising, since the 30°/50° and 30°/-50° swirl configurations share the same inner swirl vane angle and combustion air flowrates. Since the inner air stream has a larger velocity than the outer air flow, and an equal mass flow rate, the features of the air flow field are most heavily affected by this inner air swirl in the combustor. However, Figure 7 shows a more compact recirculation region than Figure 6, and this is due to the effect of counter-swirl. The counter-swirling outer air stream present in the 30°/-50° configuration has the effect of opposing the rotation of the inner air stream somewhat, and converting rotational swirling motion into turbulence. Increased turbulence aids mixing at the boundary of the recirculation region and at the interface of two fluids[3]. However, it also effectively decreases the extent of the recirculation region, and this affects flame stability. Maximum negative mean axial velocities of –2.0 m/s are observed in this recirculation zone. The smaller recirculation velocities are due to the counter-swirl condition.

It is also apparent that the luminous combustion zone associated with the counter-swirling 30°/-50° flame in Figure 4 is larger than that for the co-swirling 30°/50° case. This effect is also due to the degree of turbulent mixing associated with the counter-swirl configuration, which distorts the flame front more extensively in the counter-swirling flow and creates a larger region of luminosity[3]. The effects of co- and counter-swirl on flame dynamic response to forcing will now be presented.

System Response as a Function of Forcing Frequency

To examine flame response to an unstable equivalence ratio, the sound spectra of the flames were obtained. The 50%/50% airflow distribution was employed. Background sound spectra with only the combustion airflow present were examined first. The sound spectra thus represented the background noise due to airflow through the ducts of the burner, blower motors, etc. The background noise, in the absence of a flame, must be characterized, so that it can later be removed from the sound spectrum associated with the combustor when a flame is present. The background spectra are shown in Figure 8. The sound spectrum between 10Hz and 332 Hz is shown in Figure 8a. A detailed view of the spectrum between 10 Hz and 50 Hz is shown in Figure 8b.

As can be seen from the figure, the swirl configuration had little effect on the background noise spectrum of the burner. All three swirl configurations display very similar background sound spectra. The important frequencies of the spectrum (such as the peak at 11 Hz) are determined by large components of the burner (such as the air ducts) and by features of the airflow, rather than by the particular swirl configuration.

For purposes of comparison, a baseline noise spectrum, with a steady fuel flowrate, then had to be established for each flame. These spectra, obtained under conditions where the solenoid valve remained open in order to provide a steady, uninterrupted fuel flow to the flame, are shown in Figure 9. The background sound pressure levels, shown in Figure 8, associated with each frequency in the spectrum have been subtracted from the spectra shown in Figure 9. The presence of a flame increases the sound pressure levels in the entire sound spectrum. This is not surprising, since the energy released by dynamic expansion of gas from combustion causes increased sound pressure levels throughout the examined spectra. The most dramatic increases in sound pressure levels are seen at the higher frequencies, above 100 Hz, where the flame spectra display sound pressure levels up to 10 dB higher than the background spectrum. The sound pressure levels of frequencies above 100 Hz are approximately 2 dB higher for the 45°/50° configuration than for the 30°/50° and 30°/-50° flames.

In order to assess the impact of the fuel pulsations at a particular frequency, the 45°/50° swirl configuration in the combustor was forced at a number of frequencies corresponding to peaks seen in the sound spectrum for the unforced flame. These peaks indicate unstable modes of the flame, marking frequencies at which important turbulent events participate in combustion. The objective was to force these modes in such a way that they dominated the sound spectrum. Figure 10 shows the difference in sound spectrum intensity due to forcing at the forced frequency, measured in dB.

The increase in sound pressure level was found to be most dramatic for frequencies in the lower range of the spectrum. For example, when the flame was forced at a frequency of 11 Hz, the flame displayed an increase in sound pressure level of 6.75 dB at this frequency. This suggested that, to examine the impact of swirl configuration, it would be necessary to force at one of these lower frequencies. Further, it was noted that harmonics of the forced frequency would also show an elevated sound pressure when the fuel flow was modulated, but that this response was weak.

Based on the behavior of the 45°/50° swirl configuration, it was decided to force the flame at 15 Hz. When the pulsation signal at 15 Hz was introduced into the combustor, the flame characteristics were observed to change considerably for each flame. A strobing effect, in sync with the fuel pulsation, was observed, and the brightness and size of the flames cycled in time with the pulsation, indicating a fluctuation in the flame heat release. The change in sound of the flames was audible; this low rumble dominated the tone produced by each flame when the fuel pulsation was introduced.

The resulting flame sound spectra, obtained for each swirl configuration when the combustor was forced at 15 Hz are shown in Figure 11. The sound spectrum from 10 Hz to 332 Hz is displayed in Figure 11a while the sound spectrum between 10 Hz and 50 Hz is shown in Figure 11b. Each forced spectrum shows a dramatic increase in sound pressure level at the forcing frequency of 15 Hz. Higher harmonics of the forcing frequency also show an increase in amplitude, resulting in peaks at 31 Hz and 44 Hz. The most dramatic response is seen from the 30°/-50° flame, which displays a peak sound pressure level of 92.2 dB at 15 Hz. This is a significant increase in sound pressure level; when no forcing was present, the 30°/-50° flame displayed a sound pressure level of only 70.3 dB at 15 Hz. The increase in sound pressure level at the forcing frequency and at the first and second harmonics of the forcing frequency for each swirl combination is shown in Figure 12.

Figure 12 shows that swirl configuration has an impact on the response of the flame to the introduction of instability in the fuel flow. The 30°/-50° configuration displayed a significant increase in sound pressure level at 15 Hz, 31 Hz, and 44 Hz. The 30°/50° configuration displayed a less pronounced increase in amplitude at the forcing frequency (15 Hz), no significant response at 30 Hz, and a moderate increase of 2.5 dB in the amplitude at the 44 Hz signal. The 45°/50° configuration displayed a response close to that of the 30°/-50° configuration at 15 and 30 Hz, but no increase whatsoever in amplitude in the 44 Hz signal. In fact, a slight decrease of 0.1 dB was observed.

It is important to note that the sound pressure spectrum is not the only characteristic of the flames that is affected by fuel pulsation. Combustion completeness, flame chemistry and fuel atomization are all affected by the fuel flow behavior. What does appear to be significant is the difference in dynamic response observed for each swirl configuration. These flames responded quite differently to the same input signal, indicating that passive control techniques based on swirl distribution can have a significant impact on controlling instabilities in spray flames.

Observation of Dynamic Flame Structure

In order to examine the physics of the flame instability produced by the forcing signal, a CCD camera was used to record global structure of the unstable flames at 30 Hz from the three swirl configurations. The global structure images were then examined to track the development of the luminous region of the flame during the instability cycle. Since the heat release signature of kerosene flames is closely linked to the flame luminosity, it is possible to examine the evolution of the heat release characteristics of the flame during the cycle of the instability. The structure of the luminous region, where heat release occurs, can be observed near the peak and minimum of the heat release cycle. The differences between the three flames are most dramatic at these points during the cycle.

The structure of the 45°/50° flame near peak and minimum heat release is shown in Figure 13. Near peak heat release, (show on the left in Figure 13) the flame is a tall column with the luminous flame region extending more than 3.8 burner diameters downstream. When the heat release is near its minimum (shown on the right in Figure 13), the flame region is much smaller, and extends only 2.9 burner diameters downstream. The flame region is detached from the burner during this phase. Fuel concentrations near the nozzle decrease, and combustion is sustained by unburned fuel entrained in the recirculation region. This explains why the 45°/50° flame did not respond readily to forcing at higher frequencies (see Figure 10), and why the highest harmonic of the forcing frequency (at 44 Hz) could not be excited (see Figure 12). The effect of any interruption in the fuel flow, or change in the spray characteristics, at higher forcing frequencies is damped out by the stabilizing effect of the large volume of entrained gases in the recirculation zone. However, at low forcing frequencies, the large volume of recirculating gas effectively heats and ignites the fuel spray burst occurring during the peak heat-release phase of the cycle.

For the 30°/50° swirl configuration, the flame structure near peak heat release is different than for the 45°/50° swirl case. Instead of forming a tall column, the flame is confined to a brush-shaped region (shown on the left in Figure 14), formed when a cloud of fuel is ejected from the fuel nozzle. In this flame, the recirculation region is much smaller; as a result, the volume of unburned fuel available to sustain the flame through the minimum heat-release phase of the cycle is smaller. This phase is shown on the right in Figure 14. As can be seen, the flame region above the nozzle decreases dramatically in size. The combustion is confined to a small region, less than a burner diameter in length, positioned immediately over the atomizing nozzle during the minimum heat release phase of the cycle.

This effect is even more dramatic for the 30°/-50° swirl configuration. As can be seen on the left and right sides of Figure 15, the flame structure cycles even more dramatically when this swirl configuration is used. During the peak heat-release phase of the cycle (shown on the left), the flame brush resembles that seen from the 30°/50° swirl configuration; however, during the minimum phase of the cycle, the flame is reduced to a small blue flame directly above the fuel nozzle (shown on the right). Due to the counter-swirl configuration, the recirculation region is weakened somewhat; and increased mixing due to the counter-swirling airflow in the region above the burner dilutes any hot gases present with cooler air. Hot product gases are not recirculated effectively, in a way that would allow the instability to be damped. However, when fresh fuel exits the nozzle during the next period of maximum heat release, it mixes rapidly with combustion air due to the counter-swirling flow, is rapidly ignited by the remaining flame at the nozzle, and burns out rapidly. The resulting combustion gases are then diluted and convected downstream; this effect is also evidenced by the flamelets entrained in the airflow above the nozzle in the image on the right side of Figure 15. This combination of effects appears to account for the sensitivity of this flame to instabilities in the fuel flow.

Effect of Airflow Distribution

The effect of airflow distribution on the unstable response of the flame is now examined. The 30°/-50° swirl configuration was selected for further examination, since its unstable response to forcing was larger than those associated with the other two swirl configurations. The total amount of air fed to the burner was constant, remaining at 28.6 SCFM. However, the proportion of air fed through the inner and outer air ducts was varied, so that the proportion of the total air fed through each duct was changed. In the 25%/75% distribution, 25% of the total air, or 7.15 SCFM, was fed through the inner air annulus, and 21.45 SCFM of air, or 75% of the total air, was fed through the outer annulus. The behavior of the 30°/-50° flame with a 50%/50% airflow distribution has already been described above. In addition, a 60%/40% distribution was also examined.

The flames obtained from the 30°/-50° swirl configuration with the three airflow distributions were all found to respond to forcing. The response of the sound pressure levels at the forcing frequency and higher harmonics is shown in Figure 16. As can be seen from the figure, an increase in the proportion of air fed through the inner annulus increases the unstable response of the flame. The sound pressure level of every frequency examined, including the first and second harmonics, increased by several decibels. There was a 7.1 dB increase in the sound pressure level at 15 Hz when the proportion of air fed through the inner annulus was increased from 25% to 50%.

The reason appears to be related to the extent of the recirculation region in the flow. The relatively weak swirl imparted to the air emerging from the inner annulus did not form a broad or extensive recirculation region. Since the airflow fed through the outer annulus had a higher level of swirl in this configuration, increasing the proportion of air fed through the outer annulus spread the flow radially, thus decreasing the axial velocity. The outer air annulus also had a larger cross-sectional area at the outlet; thus, if the same mass flowrate was fed through the larger duct, the total velocity of the flow decreased. Hot gases and combusting gases thus had a much longer residence time, and the unstable response of the burner to oscillatory equivalence ratio was far less severe. The rate of heat release remained more stable during the fuel-lean, minimum heat-release phase of the instability cycle, since combusting gases were convected out of the reaction region more slowly. The flame then reignited less abruptly when the fuel spray was reintroduced during the fuel-rich phase, since some quantities of unburned fuel were still present from the previous cycle, and the mechanisms of turbulent mixing leading to ignition occurred more slowly when the airflow velocities were lower.

Summary

Passive control of swirling spray flames has been demonstrated using radial distribution of swirl and air flow to a co-annular, swirl-stabilized spray burner. The installation of a solenoid valve in the fuel line, along with the necessary signal generator and amplification electronics, has made it possible to introduce oscillations in the equivalence ratio of the flame. The effects of co- and counter-swirl airflows and airflow distribution in the burner on the structure and dynamic response of the flame have been examined.

The structures of unforced flames, obtained with a steady fuel flowrate were found to depend heavily on the features of the recirculation region associated with the combustion airflow. The recirculation regions in the non-reacting airflow associated with each case were examined directly using PIV diagnostics. An increase in the swirl number associated with inner annulus air flow was found to increase the size of the recirculation region, thus creating a larger flame. A counter-swirling swirl condition was found to produce an increase in turbulent distortion of the flame.

The effect of swirl configuration and airflow distribution on the dynamic response of the spray flames to an oscillatory equivalence ratio has been investigated. When low-frequency instabilities were introduced into the fuel flow, the response of the flame was found to depend to a great extent on the swirl configuration. Larger recirculation regions in the flow and airflow distributions that increase the residence time of product gases and combusting gases above the burner, improved flame stability. The 30°/-50° configuration responded most dramatically, displaying an increase in the sound pressure level at the forced frequency of over 20 dB when equal flow rates of air were fed through the inner and outer air annuli. Higher harmonics of the forced frequency were also readily excited for this swirl configuration. The response of the 30°/50° and 45°/50° configurations were less dramatic. The 30°/50° flame showed the smallest increase in sound pressure level at the forcing frequency, and also damped out the higher harmonics of the forced frequency. This flame may have had a smaller acoustic response than either the 45°/50° or 30°/-50° flame for reasons related to completeness of combustion. This flame featured neither the extensive recirculation region of the 45°/50° flame, nor the aggressive mixing associated with the counter-swirl configuration; it is likely that some of the fuel was simply not burned effectively. The total heat release of the flame is thus lower, and thus less energy was available to drive unstable behavior.

Passive control of combustion driven instability can be obtained using radial distribution of swirl and changing the air flow distribution in the burner. On the basis of the above findings, it is to be expected that spray flames featuring large recirculation regions will be less vulnerable to high-frequency instabilities, and that spray flames whose airflow fields are configured to achieve the longest residence times will be generally less susceptible to instabilities in fuel flow rate. These observations demonstrate the practical applicability of swirl and flow distribution as a means of passive control.

Acknowledgments

This research was supported by the Office of Naval Research, program manager Dr. Gabriel D. Roy. This support is greatly appreciated.

References

1. Sivasegaram, S., and Whitelaw, J.H., Suppression of Oscillations in Confined Disk-Stabilized Flames, *Journal of Propulsion*, Vol. 3, No. 4, 1987, pp. 291-295
2. Rayleigh, J.W.S., *The Theory of Sound*, Vol. 2, Dover Publications, New York, 1945, pp. 170-235.
3. Gaydon, A.G., and Wolfhard, H. G., *Flames, Their Structure, Radiation, and Temperature*, Wiley, New York, 1979

4. Schadow, K.C., and Gutmark, E., Combustion Instability Related to Vortex Shedding in Dump Combustors and their Passive Control, *Progress in Energy and Combustion Science,* Vol. 18, No. 2, 1992, pp. 117-131.
5. Gutmark, E.J., Grinstein, F.F., Flow Control With Noncircular Jets, *Annual Review of Fluid Mechanics*, Vol. 31, 1999, pp. 239-272.
6. Schadow, K.C., Gutmark, E., Wilson, K.J., and Smith, R.A., Multistep Dump Combustor Design to Reduce Combustion Instabilities. *Journal of Propulsion and Power,* Vol. 6, No. 4, 1990, pp. 407-411.
7. Paschereit, C. O., and Gutmark, E., Passive Combustion Control Applied to Premix Burners. *40th AIAA Aerospace Sciences Meeting and Exhibit*, Reno, NV, January 2002, AIAA Paper 2002-1007**.**
8. Hu, H., Saga, T., Kobayashi, T., Taniguchi, N., Passive Control on Jet Mixing Flows by using Vortex Generators, *6th Triennial Symposium on Fluid Control*, Sherbrooke, Canada, August 2000.
9. Steele, R. C., Cowell, L. K., Cannon, S. M., Smith, C. E., Passive Control of Combustion Instability in Lean Premixed Combustors, *Journal of Engineering for Gas Turbines and Power*, Vol. 122, No. 3, July 2000, pp. 412-419.
10. Smith, C.D., and Cannon, S.M., CFD Assessment for Passive and Active Control Strategies for Lean, Premixed Combustors, *Proceedings of the 37th AIAA Aerospace Sciences Meeting and Exhibit*, Reno, NV, January 1999, AIAA Paper 99-0714.
11. Richards, G. A., and Janus, M.C.: Characterization of Oscillations during Premix Gas Turbine Combustion, *Proceedings of ASME Turbo Expo 97,* Orlando, FL, June 1997, ASME Paper 97-GT-244.
12. Nasr, G.G., Yule, A.J., and Bendig, L., *Industrial Sprays and Atomization: Design, Analysis and Applications,* London, Springer, 2002.
13. Lubarsky, E. and Levy, Y.: Experimental Investigation of Flame-Holding System for the Suppression of Ramjet Rumble, *Proceedings of the 27th Symposium (International), on Combustion,* The Combustion Institute, Boulder, CO, August 1998, pp. 2033-2037.
14. Gupta, A. K., Lilley, D. G., and Syred, N., *Swirl Flows,* Abacus Press, Tunbridge Wells, UK, 1984.

15. Mehresh, P., Habibzadeh, B., Gupta, A.K., Control of Spray Flame Characteristics using High Shear in a Double Concentric Swirl Burner, *Proceedings of the 2002 International Joint Power Generation Conference (IJPGC)*, Phoenix, AZ, June 2002, pp. 1027-1037.
16. Gao, Z., Mashayek, F., Linck, M., Gupta, A.K., Experimental Results and Calculations of 2-Phase Flow in a Swirl Burner Under Isothermal Condition, *Proceedings of the 41st AIAA Aerospace Sciences Meeting*, Reno, NV, January 2003, Paper AIAA 2003-0336.
17. Linck, M., Armani, M., and Gupta, A. K., Flow Characteristic Effects on Exhaust Gas Composition in Kerosene Spray Flames, *Proceedings of the 1st IECEC Conference*, Portsmouth, V, August 2003, Paper AIAA 2003-5929.
18. Linck, M., Armani, M., and Gupta, A. K., Passive Control of Unstable Combustion in a Swirl-Stabilized Spray Combustor, *Proceedings of the 42nd Aerospace Sciences Meeting and Exhibit*, Reno, NV, January 2004, Paper AIAA 2004-0810.
19. Linck, M., Armani, M., and Gupta, A. K., Effect of Swirl and Fuel Pulsation on Flame Dynamics, Flame Structure, and Droplet Dynamics in Swirl Stabilized Spray Flames, *Proceedings of the 6th Annual ASME Power Conference*, Baltimore, MD, March 2004, Paper PWR 2004-52048.
20. Gupta, A. K. and Linck, M., Passive Control of Flow and Flame Structure in Spray Combustion, *Intl. Colloquium on Combustion Control,* Cranfield University, Cranfield, UK, August 2003.
21. Gupta, A. K., Lourenco, L., Linck, M. and Archer, S., A New Method to Measure Flowfield in Luminous Spray Flames, *Journal of Propulsion and Power*, Vol. 20, No. 2, March/April 2004, pp. 369-372.
22. Linck, M. and Gupta, A. K., Effect of Swirl and Combustion on Flow Dynamics in Luminous Kerosene Spray Flames, *Proceedings of the 41st AIAA Aerospace Sciences Meeting*, Reno, NV, January 2003, Paper AIAA 2003-1345.
23. Conrad, T. J., Bibik, A., Lee, J.Y., Shcherbik, D., Lubarsky, E., and Zinn, B. T., Control of Combustion Instabilities by Fuel Spray Modification Using Smart Fuel Injector, *Proceedings of the 39th AIAA/ASME/SAE/ASEE Joint Propulsion Conference and Exhibit*, Huntsville, AL, July 2003, Paper AIAA 2003-4937.
24. Timmler, J., and Roth, P., Optical Measurement of Droplet Evaporation Rates*, Optical Particle Sizing: Theory and Practice*, Plenum Press, New York, 1988, pp. 511-522.
25. Presser, C., Gupta, A. K., Avedisian, C. T., and Semerjian, H.G., Effect of Dodecanol Content on the Combustion of Spray Flames, *Atomization and Sprays*, Vol. 4, No. 3, 1994, pp. 207-222.
26. Bachalo, W. D., and Houser, M. J., Phase/Doppler spray analyzer for simultaneous measurements of drop size and velocity distributions, *Optical Engineering*, Vol. 23, No. 5, 1984, pp. 583-590.
27. Raffel, M., Willert., C., Kompenhans, J.: *Particle Image Velocimetry, A Practical Guide*, Springer-Verlag, Berlin, 1998.

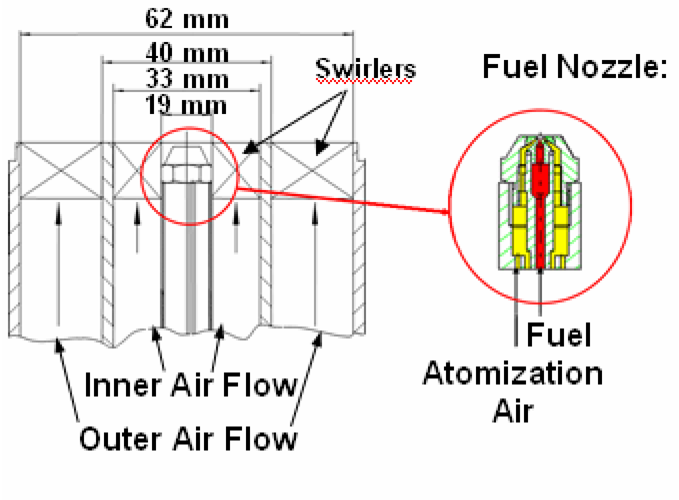

Figure 1. Schematic diagram of the spray burner and fuel nozzle

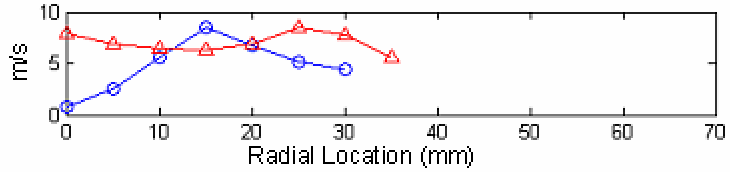

a) Mean Axial Velocity (m/s)

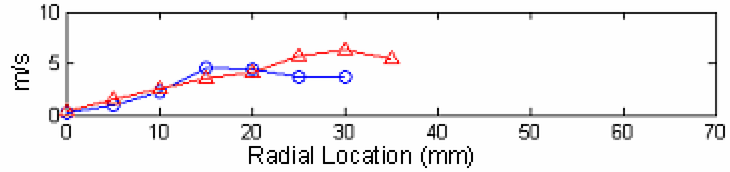

b) Mean Radial Velocity

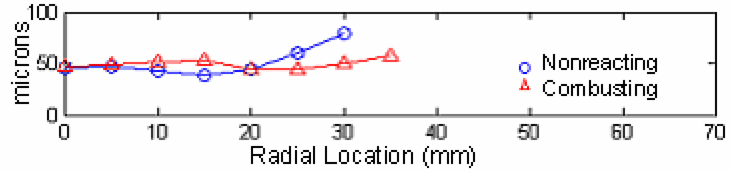

c) Mean Arithmetic Diameter

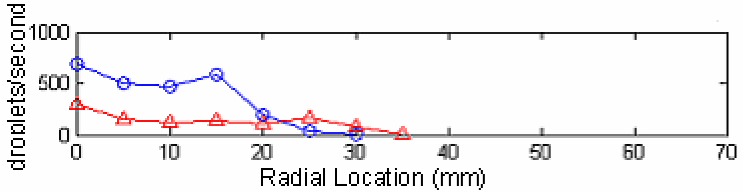

d) Droplet number density, in droplets/second

Figure 2. Fuel spray characteristics from the atomizing nozzle at 30 mm downstream from the atomization nozzle using 30°/50° combustion air swirl configuration, 50%/50% airflow distribution, 28.6 SCFM total air flowrate.

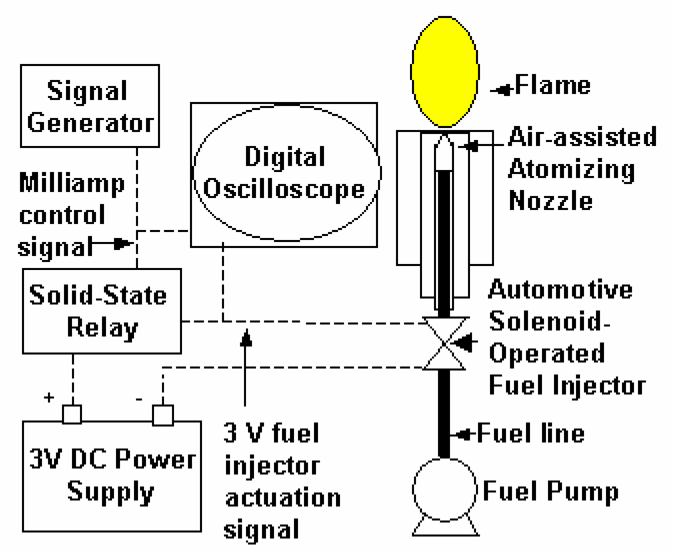

Figure 3. Schematic diagram of the spray burner fuel delivery system

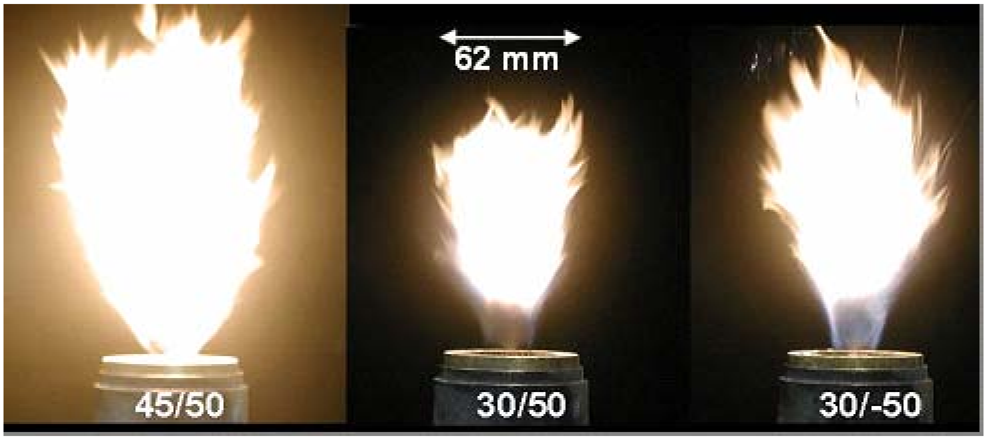

Figure 4. Flames generated by 45°/50°, 30°/50° and 30°/-50° swirl combinations; 50%/50% airflow distribution, 28.6 SCFM total air flowrate

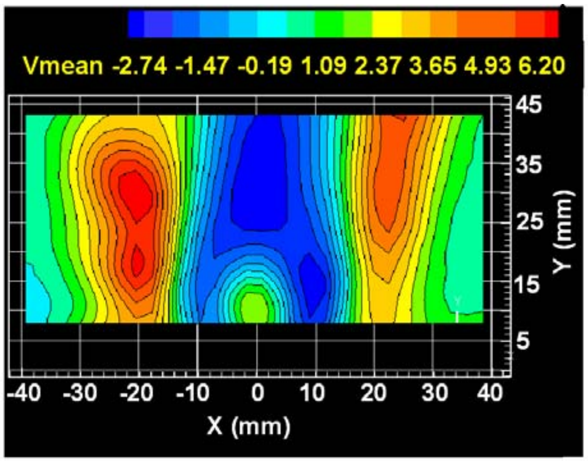

Figure 5. Mean axial velocity contours (Vmean in m/s), 45°/50° swirl configuration, 50%/50% airflow distribution, 28.6 SCFM total air flowrate

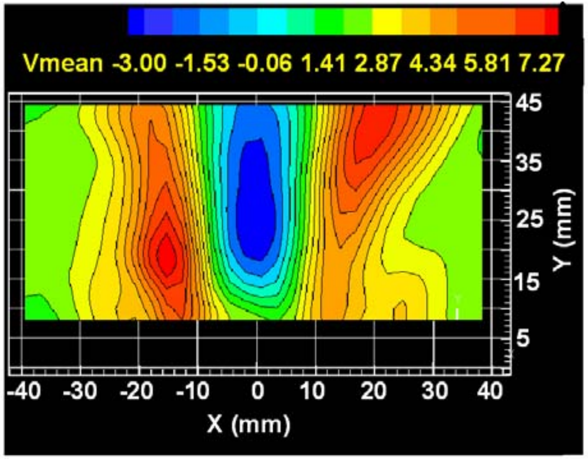

Figure 6. Mean axial velocity contours (Vmean in m/s), 30°/50° swirl configuration, 50%/50% airflow distribution, 28.6 SCFM total air flowrate

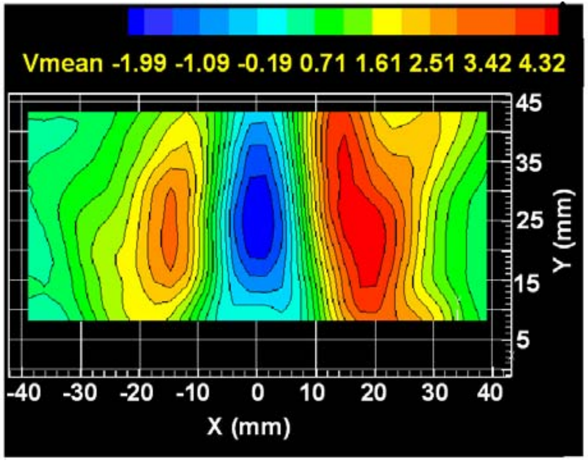

Figure 7. Mean axial velocity contours (Vmean in m/s), 30°/-50° swirl configuration, 50%/50% airflow distribution, 28.6 SCFM total air flowrate

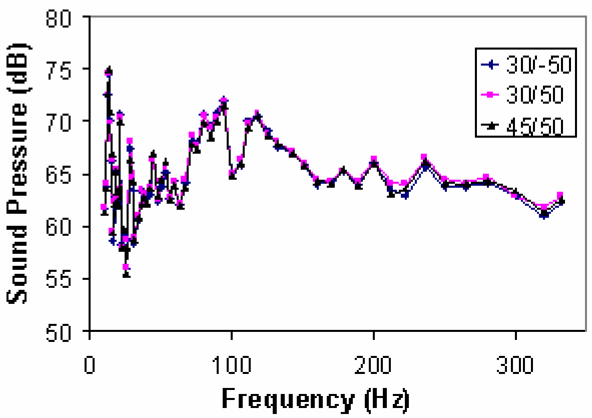

a) Frequency range 10-358 Hz

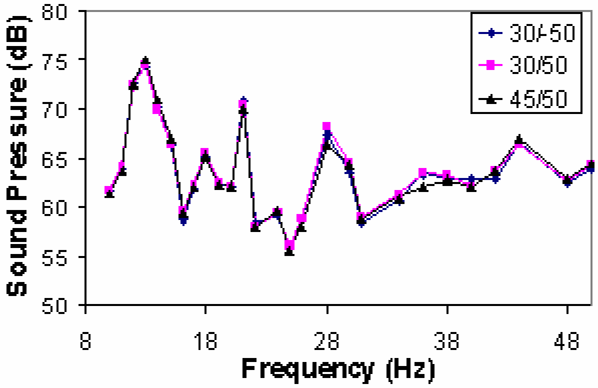

b) Frequency range 10-50 Hz

Figure 8. Background noise spectra without fuel spray or flame

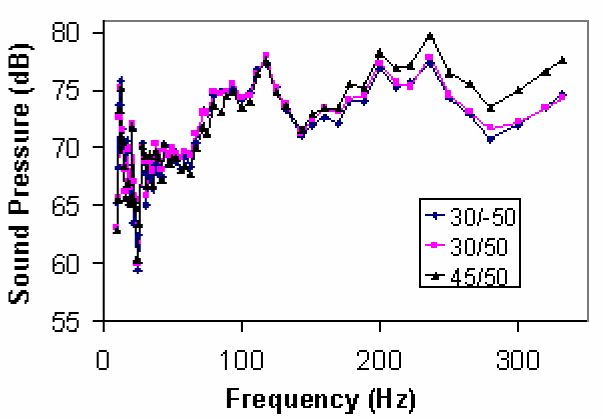

a) Frequency range 10-358 Hz

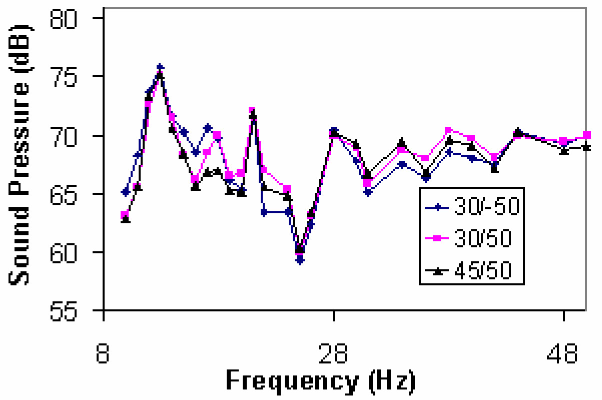

b) Frequency range 10-50 Hz

Figure 9. Sound spectra of unforced flames

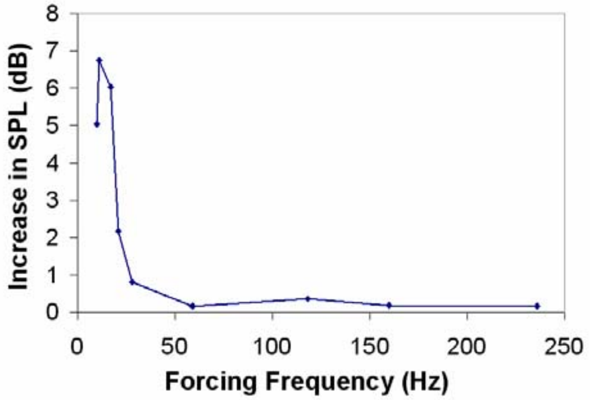

Figure 10. Response of 45°/50° flame at forced frequency to fuel pulsations

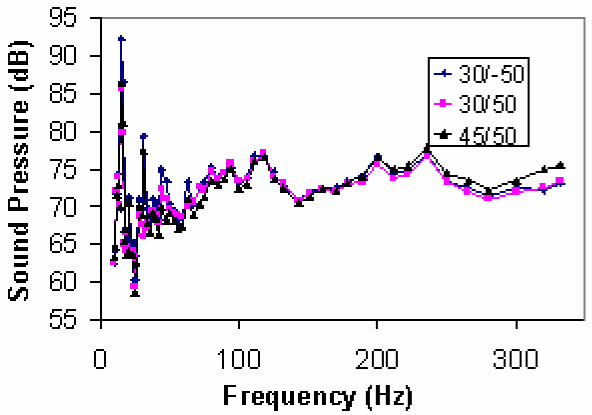

a) Frequency range 10-358 Hz

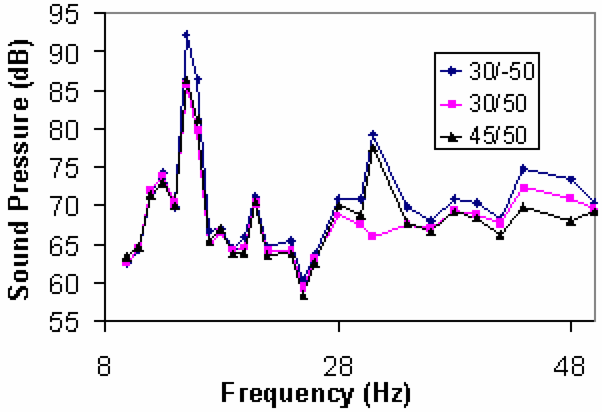

b) Frequency range 10-50 Hz

Figure 11. Sound spectra of forced flames with input signal at 15 Hz

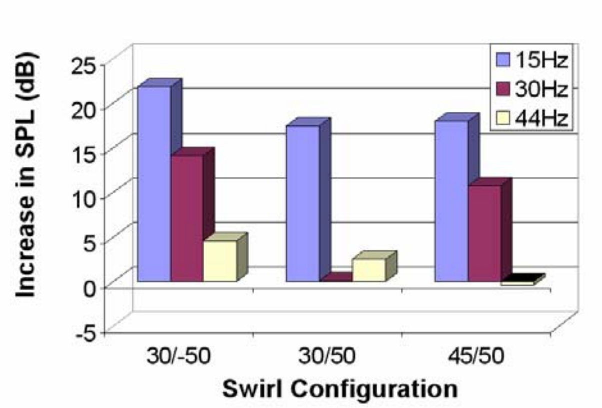

Figure 12. Flame acoustic response to forcing at 15 Hz with response shown at forcing frequency and harmonics

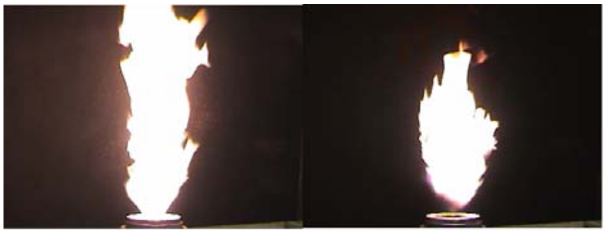

Figure 13. Images of forced 45°/50° flame. Left image: Flame near peak heat release. Right image: Flame near minimum heat release.

Figure 14. Images of 30°/50° co-swirling flame. Left image: Flame near peak heat release. Right image: Flame near minimum heat release.

Figure 15. Images of 30°/-50° counter-swirl flame. Left image: Flame near peak heat release. Right image: Flame near minimum heat release.

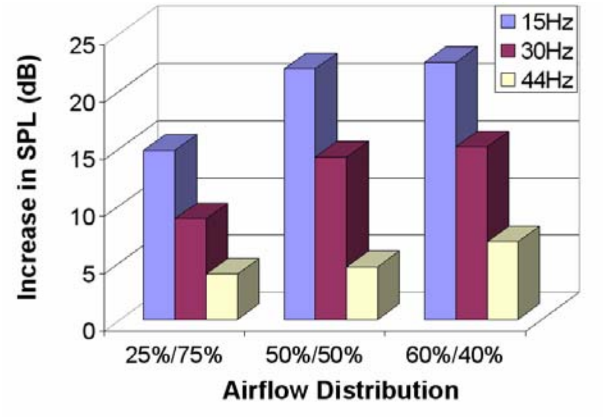

Figure 16. Effect of airflow distribution on flame acoustic response to forcing at 15 Hz with response shown at forcing frequency and higher harmonics

Appendix B.2

Gupta, A. K., Lourenco, L., Linck, M., and Archer, S., “A New Method to Measure Flowfield in Luminous Spray Flames”

J. Propulsion and Power, Vol. 20, No. 2, March/April 2004, pp. 369-372.

A New PIV Method to Measure Flowfields in Luminous Spray Flames

A.K. Gupta, L. Lourenco, M. Linck and S. Archer*
Department of Mechanical Engineering
University of Maryland
College Park, Maryland 20742
** Author for correspondence (e-mail: akgupta@eng.umd.edu)*

Abstract

The application of digital Particle Image Velocimetry (PIV) techniques to luminous flames is challenged by the high background radiation from the flame. Overexposure of the second frame in a given frame pair is common, due to the strong background signal from the flame and also due to the time necessary for the camera to read the first image from the horizontal register on the CCD chip, and store it to an off-chip memory while the second image is being captured by the photodiode array of the CCD chip. This technical note describes unique development of digital PIV techniques to observe particle and droplet motion inside a luminous liquid-fueled spray flame or other luminous flames. The technique uses narrow band-pass filters and mechanical shutters to eliminate the background signal and noise so that 2-D or 3-D instantaneous flowfield in flames can be determined from the high-quality double images recorded of the very high background radiating flames. The technique has been successfully demonstrated using a luminous spray flame to obtain clean pairs of instantaneous images of droplets and particles at two discreet time intervals. These images are then processed to obtain the distribution of mean and rms components of axial, radial and tangential velocity, strain rate, vorticity and other flow characteristics.

Introduction

Several investigators have used Particle Image Velocimetry (PIV) diagnostics to determine the flow characteristics of a range of laboratory-scale and practical devices that vary in geometry and flow complexity under isothermal flow (normal temperature) conditions[1-3]. In PIV the flow is seeded with submicron-sized particles and the motion of these particles is used to determine the gas phase velocity. The size and density of the particles depend on the nature of the flow characteristics. The flow velocity is determined from double exposures of these particles taken at a very small and known time interval. The flow velocity is determined by measuring the distance a given particle travels between the two consecutive exposures of the same particle. The particle size is very small and can flow the flow at high frequencies so that the flow velocity is the same as the particle velocity. In the case of luminous flames the determination of flow characteristics has not been possible before due to the high background signals emanating from flames during the combustion of fuels.

Since the introduction of particle image velocimetry (PIV) as a diagnostic technique, considerable progress has been made to develop systems that can extract information on the flowfield from any number of angles and in three dimensions[1-3]. The diagnostic technique provides instantaneous information on the entire flowfield for mean and rms values of axial, radial and tangential components of velocity, vorticity, strain rates and other flow characteristics. Such detailed characterization of a flowfield would take significantly longer time using other non-intrusive diagnostic techniques, such as, laser velocimetry, photon correlation or double spark photographic techniques. For the first time it is now possible to visualize the entire flowfield in 3-D so that one can make direct comparisons of the flow features with calculations. Systems with as many as six cameras have been utilized in the literature to analyze a wide variety of flows under normal temperature flow conditions, ranging from simple laminar to more complex turbulent and supersonic.

In principle PIV diagnostics can be used to provide important information on the flow and turbulence characteristics of any kind of flow under both isothermal and combustion conditions. However, PIV observations within luminous or semi-luminous flames have been problematic. The radiation from the flame tends to overwhelm the illumination of the laser sheet beam, thus preventing the acquisition of useful information about the movement of droplets, particles or seeded particles in the flow. In the case of spray flames, the flames in the near vicinity of the burner exit are often luminous so that illumination of the flow with a laser beam results in only over-exposed background signal levels, i.e, no information is obtained on the transport of droplets or small submicron size particles seeded in the flow from which information on droplet velocity or particle velocity (and hence the fluid flow) is determined.

This technical note documents the development of a new PIV system that incorporates narrow-band-pass filters and mechanical shutters, which can be used to alleviate the problem of high background flame radiation. The new method has been successfully used to observe the behavior of fuel droplets and/or very small size seed particles within the highly luminous kerosene spray flames from which information on the mean and turbulence characteristics of the flow associated with the droplets and carrier phase is determined.

Facility Design

A swirl-stabilized kerosene spray flame was used to obtain a luminous flame for flow diagnostics. The PIV system discussed below was used to observe the dynamics of fuel droplets and seed particles introduced into the combustion airflow to determine the airflow motion. The burner used was a double concentric swirl burner having fuel spray located at the center of the burner. Air was supplied to the burner through two concentric air annuli. The swirl angle and airflow rate distribution in the two annuli could be varied independently[4]. A commercially available air-assist spray nozzle was used to create a hollow cone fuel spray, with a mean droplet size of approximately 50 microns. The airflow and swirl angle could be used to alter the spray structure considerably[5,6].

The specific flames examined here are highly luminous and represents characteristics similar to those observed during the combustion of solid fuels and propellants, and high energy density fuels that have the propensity to produce high levels of soot. The high background luminosity from flames masks the scattered light signal produced from the submicron-size particles, droplets or particles. A sample photograph of the luminous kerosene spray flame used for flowfield diagnostics, showing high background flame luminosity, is shown in Figure 1. In order to take meaningful data from within such a flame, the PIV system had to be able to deal with the broad-spectrum radiation produced from the flames.

The PIV system

The specific system used here was a 3-D PIV manufactured by Integrated Design Tools (IDT^{TM}). A schematic diagram of the system is shown in Figure 2 and, consisted of the following:

1. A Solo PIV Nd:YAG pulse laser containing two laser cavities which fire independently.
2. Two 1280 X 1024 pixel CCD cameras (sharpVISION^{TM} 1300-DE, model Sony ICX085AL CCD) equipped with 532 nm narrow-band-pass filters having a bandwidth of 0.87 nm.)
3. Mechanical shutters that regulate the light entering each camera.
4. Power supplies for lasers and shutters.
5. IDT 1000 PIV system, which acts as a controller to synchronize the laser pulses and cameras.
6. IDT 2000 control modules for the cameras.

A PC equipped with the boards and the appropriate software necessary to acquire the images from the cameras and their subsequent analysis to obtain information on the velocity and turbulence characteristics. Velocity vector data generated by the software was then plotted and displayed using Tecplot^{TM} software.

The laser is used to project a thin sheet of coherent light through the region of interest. The pulse duration of each laser cavity is on the order of nanoseconds. The delay time between pulses can be adjusted in order to respond to different flow conditions.

The PIV measurements depend on capturing pairs of images separated in time of the order of nanoseconds. The fundamental problem to be resolved when attempting to carry out PIV diagnostics in high luminosity flames is to prevent overexposure of the photodiodes in the cameras during the two exposures. CCD chips used in PIV employ electronic shutters, which, when open, make the photodiode sensitive to incoming radiation. This electronic shutter opens before the first laser pulse is fired (see Figure 3). When the first laser pulse is fired, the light captured by the optics falls on to the photodiode array of the CCD camera. The impact of the photons on this array causes electrons to migrate into potential wells corresponding to each pixel. The electronic shutter then closes, and the charges developed on the photodiode array are transferred to the horizontal register, a process that, for CCD cameras, takes approximately 200 to 250 microseconds. The electronic shutter then opens again, and the second image illuminated by the laser sheet beam is then captured, but the information from the first image pulse is still on the register. The register takes ~30-80 ms to clear (depending on the type of CCD chip), during which time the electronic shutter remains open, and the photodiode array remains in a state where incident light from the flame is still recorded onto the camera detector. As a result, the second image is overexposed by the flame background luminosity, thus obscuring information from the particles or droplets. Our experience has shown that it is difficult, if not impossible, to utilize the conventionally available PIV systems for determining flowfield in high background spray flames.

In the system described here, the two cameras used allow one to measure flow velocity in 3-D after proper calibration. The acquisition of a calibration image for the 2-D case is relatively straightforward. A target with evenly spaced high-contrast features is placed in front of the camera, and an image is acquired. The distances between the features are entered into the software, and the software allows one to relate camera pixels to distance in millimeters. However, the 3-D calibration is more complex. For 3-D data acquisition, a series of at least five, and preferably nine, images each is acquired on the two cameras. Each image is recorded at some known distance from the known plane (centerline). The dimensions of one image are then entered into the software. The software observes the shift in the high-contrast features that results from each offset value, and develops a complex relation that establishes a particle’s motion in three-dimensional space on the basis of its travel between one PIV image and the next. The algorithm used to develop this relation is quite robust, and tolerates a surprising amount of non-ideality in target alignment, illumination, spacing, etc.

Each camera is equipped with a narrow band interference filter (centered at laser wavelength of 532nm), which blocks off majority of the background radiation produced by the flame other than this wavelength. Thus a filter alone cannot prevent overexposure of the photodiode in the camera since the light at the laser wavelength still enters the camera detector. The specific flame examined here was yellowish-white and produced a very broad spectrum of distributed radiation. A sufficient portion of that radiation is in the 532 nm range, which transmits through the filter. The second image is therefore overexposed. In order to deal with this problem, a mechanical shutter, situated behind the camera optics and in front of the filter is used. In operation the camera shutter begins to close at the initiation of each sample acquisition (first image). Therefore negligible light passes on to the camera detector after the second image acquisition since most of the light entering the cameras is during the significantly long time duration over which the register from the first image clears (~30-80 ms). The unwanted light passing onto the camera detector is thus eliminated. The second acquired image is thus of good and sharp quality. The mechanical shutter prevents overexposure of the photodiode array and makes it possible to carry out PIV analysis of luminous or high background radiation flames. This new operational cycle is described in Figure 4. The resulting double images captured using mechanical shutters and narrow band interference filters are shown in Figure 5. As can be seen, the second image is somewhat dimmer than the first, since the shutter is already partly closed. However, there is no overexposure from background radiation from the flame. Thus the images obtained with the new PIV system allows one to make accurate and reliable PIV measurements in flames as the two recorded images of the particles and droplets are very sharp and clear. In cases where the flames are not as luminous or possess lower background radiation, the quality of the images obtained are much better than those obtained without any mechanical shutter and/or interference filters, since the images obtained contains less noise with the result of more reliable and accurate information on mean velocity and turbulence characteristics.

The data files generated by the PIV system are displayed and manipulated using the software. The software allows one to calculate mean and rms values of axial, radial and tangential velocity. The information from the individual realization can also be used to calculate vorticity and strain rates, and other flow characteristics. A comparison of the velocity information obtained from PIV with other diagnostics, such as phase Doppler interferometry technique showed good agreement.

A sample flowfield average velocity vector plot from within a burning spray flame is shown in Figure 6. The radial velocity distribution immediately downstream of the burner is shown in Figure 7. The vector plots show the projection of the total 3-D velocity vector of the spray on the X-Y plane; the vectors are color-coded according to the magnitude of the vector component of interest (axial velocity, v or radial velocity u). The calculated vorticity distribution for the conditions given above is shown in Figure 8. The results show low average vorticities, between -.170 and .294, with the majority of the field near zero.

The data presented here has demonstrated the capability of the new PIV diagnostics to obtain measurements in any kind of combustion system including fuel sprays, solid fuel combustion, and other low or high background luminous flames. The diagnostic technique also allows one to obtain better quality data from flames with low or negligible background flame radiation. This type of data then allows one for the first time to make direct comparison between experimental data and predictions for the entire flow domain. The new PIV diagnostics also allow one to visualize the time resolved motion of the flow in 3-D as a movie.

Conclusions

It has been demonstrated that the simultaneous use of mechanical shutter and narrow band-pass interference filters can resolve over-exposure problems associated with PIV diagnostics in flames, in particular luminous flames that feature high background flame radiation. The PIV system discussed here is capable of detecting fuel droplets, particles or seed particles under a variety of flow conditions. The diagnostics allow one for the first time to obtain detailed and comprehensive information on flow dynamics associated with complex flows, including swirling flows, jets, and various kinds of practical systems under reacting and combustion conditions can be generated.

Acknowledgments

This research was supported by the Office of Naval Research, program manager, Dr. Gabriel D. Roy. This support is greatly appreciated.

References

1. Aroussi, A., Kucukgokoglan, S., Menacer, M., Pickering, S.J.: PIV Measurements of Swirling Flows From Two Adjacent Burners, 9th International Symposium on Flow Visualization, Heriot-Watt University, Edinburgh, Scotland, 2000.
2. Nie, J.X., Yeboah, Y.D., Bota, K.B., and Bai, T.: Laser Doppler Velocimetry and Particle Image Velocimetry Measurements of Premixed Methane-Air Flames and their comparisons, 3RD ASME/JSME Joint Engineering Conference, San Francisco, CA, USA, 1999.

3. Yeboah, Y.D., Nie, J.X., Bota, K.B., Bai, T., and Ross, H.D.: Particle Image Velocimetry Measurements of Premixed Methane-Air Flames, The Proceedings of 1998 ASME Fluids Engineering Division Summer Meeting, Washington, DC, FEDSM98-5267, 1-25, 1998.
4. Linck, M. and Gupta, A. K.: Effect of Swirl and Combustion on Flow Dynamics in Luminous Kerosene Spray Flames, AIAA Aerospace Sciences Meeting, Reno, NV, January 6-9, 2003, Paper No. 2003-1345.
5. Habibzadeh, B and Gupta, A. K.: Passive Control of Kerosene Spray Flame Structure in a Swirl Burner, Proc. Intl. Conference on Advanced Energy Conference and Related Technologies, RAN 2001, Nagoya, Japan, December 15-17, 2001.
6. Gupta, A. K., Habibzadeh, B., Archer, S., and Linck, M.: Control of Flame Structure in Spray Combustion, 15th ONR Propulsion Meeting, Washington, DC, August 5-7, 2002, pp. 29-34.

Figure 1. Photograph of a luminous kerosene spray flame.

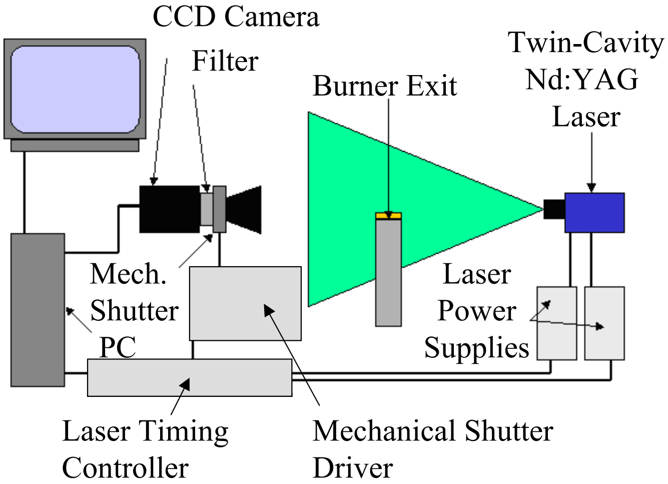

Figure 2. A schematic diagram of the PIV facility.

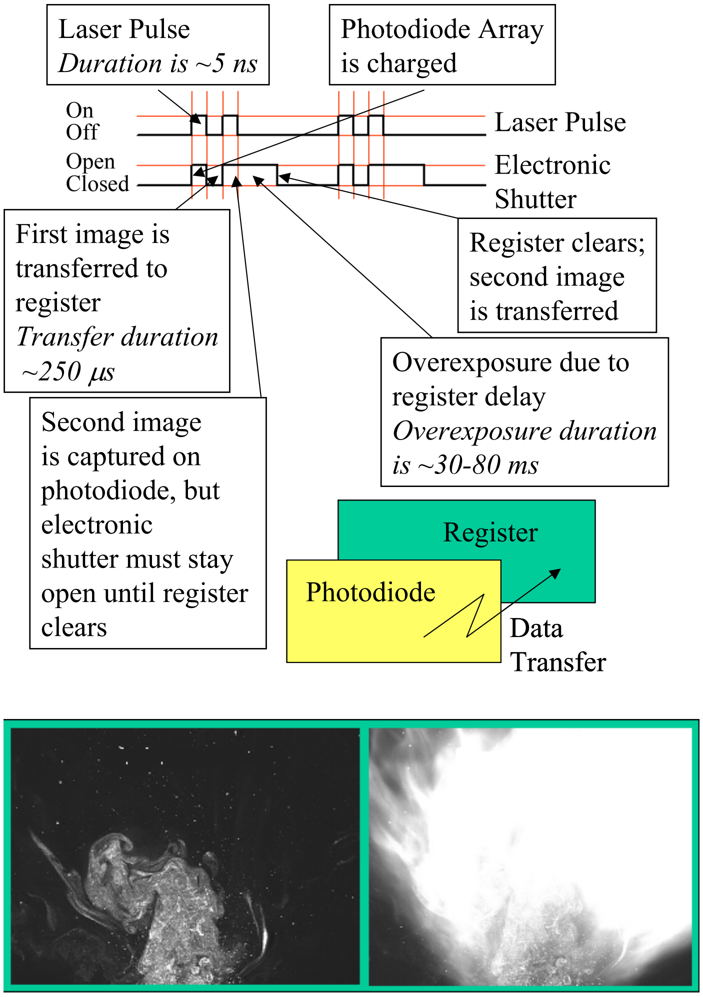

First Exposure Second Exposure

Figure 3. Operational cycle of conventional PIV system without mechanical shutter.

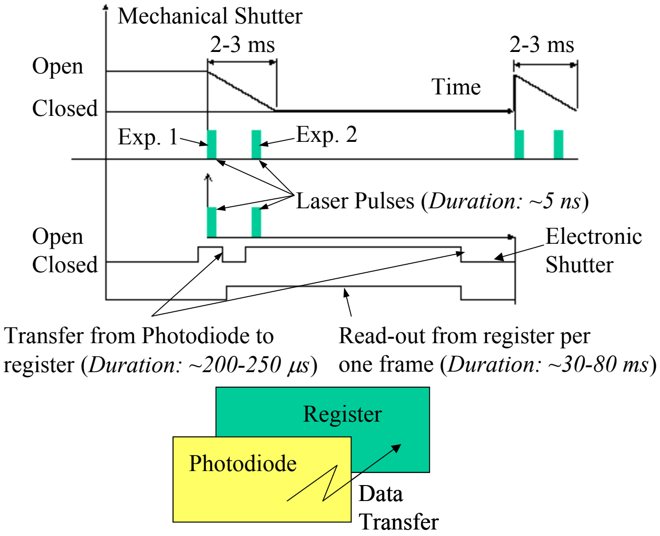

Figure 4. Operational cycle of the new PIV system.

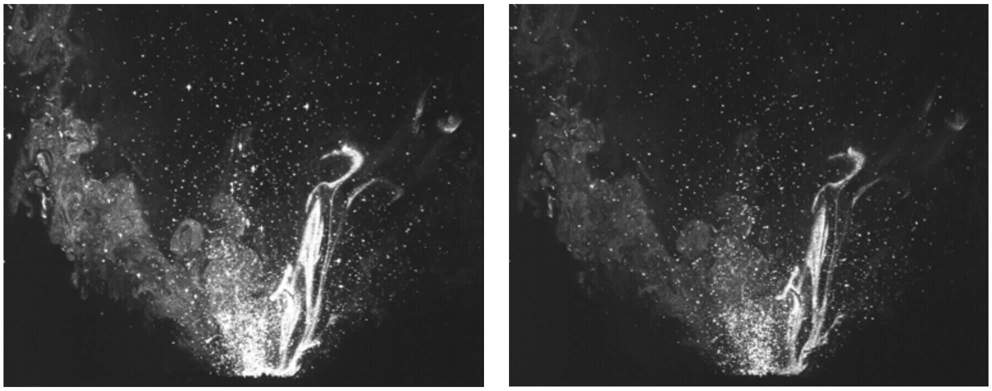

First Exposure Second Exposure

Figure 5. Sample images from successive exposures using a mechanical shutter and narrow band filter.

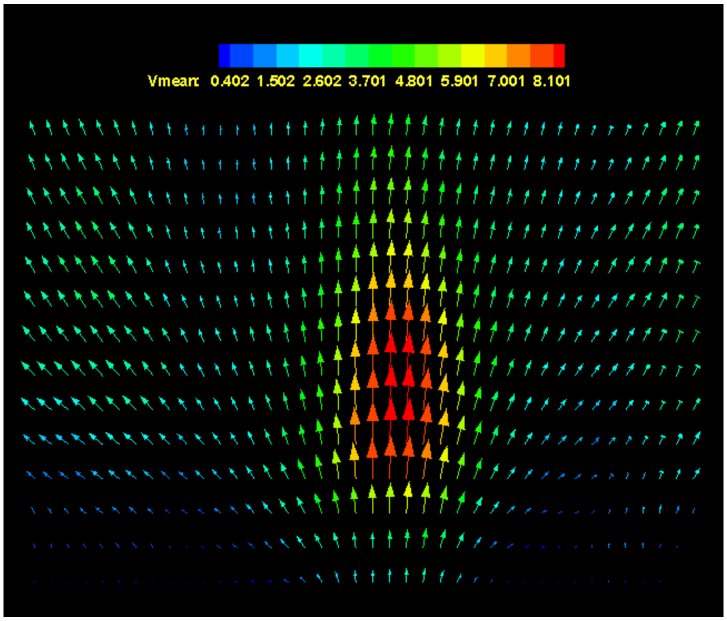

Figure 6. Average 3-D velocity plot, color-coded by axial velocity from within the luminous spray flame.

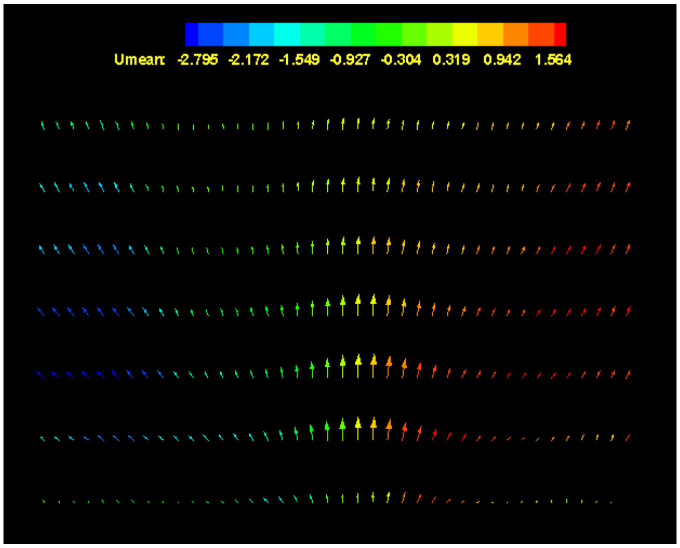

Figure 7. Time averaged radial velocity in the spray flame.

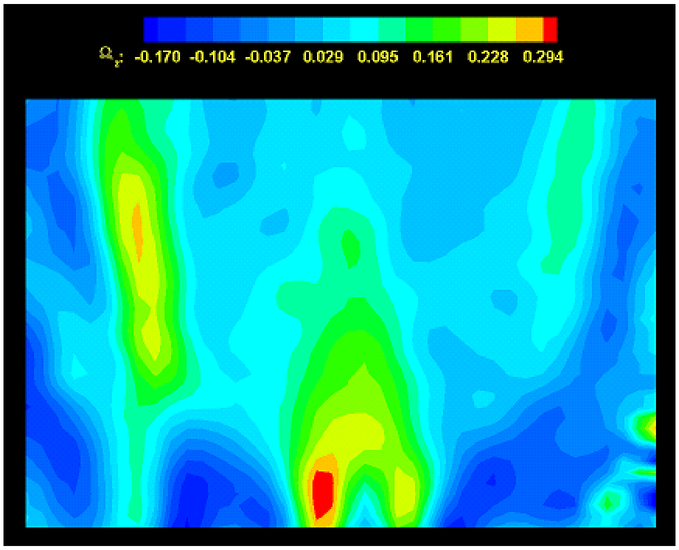

Figure 8. Time averaged vorticity map in the spray flame.

Appendix B.3

Linck, M., Yu, K. H., and Gupta, A. K., “Dynamics of Unconfined and Confined Methanol and Kerosene Spray Flames”

Proc. International Energy Conversion Engineering Conference (IECEC), Providence, RI, August 16-19, 2004, Paper No. AIAA-2004-5503.

Dynamics of Unconfined and Confined Methanol and Kerosene Spray Flames

M. Linck, K. H. Yu* and A. K. Gupta**

University of Maryland

Dept. of Mechanical Engineering

College Park, MD 20742, USA

* Department of Aerospace Engineering

**akgupta@eng.umd.edu

Abstract

An optically-accessible combustor enclosure has been assembled for investigating confined combustion conditions that simulate underwater propulsion under well defined conditions. The design consists of a coaxial swirl-stabilized spray burner fired into an optically accessible combustion chamber. The exhaust plume from this spray combustor is discharged into a second chamber that contains a co-flowing fluid of different properties to simulate underwater propulsion conditions. In this paper the thermal characteristics of spray flames in the first combustion chamber without the presence of second chamber downstream are first examined in detail for the effect of fuel property and thermal loading on global and quantitative flame behavior. Two each of confined and unconfined flames have been examined in detail. In one case the burner was fuelled by a single component (methanol) fuel while in the other case a hydrocarbon mixture (kerosene) was used. The four flames were examined under confined and unconfined conditions to determine the role of fuel property and confinement on combustion. Information was first obtained on global flame features followed by detailed examination. Detailed spray flame characteristics examined include: global flame features, flow dynamics, and noise-amplitude sound spectra. The results showed similar global features and dynamic effects of the flames at same thermal loads to the burner when same combustion air flows to the burner were employed under respective unconfined or confined conditions. This demonstrates the applicability of results obtained from this system to a variety of fuels, and establishes a basis for comparison with other studies using other fuels.

Introduction

In an underwater propulsion system, the performance of propulsion system will depend to a great degree on the operational conditions of the combustor. The discharge of the exhaust plume to the surrounding water will create a two phase mixture. The shear layer mixing of this two phase mixture will have an impact on the combustor performance which will subsequently have an impact on the two-phase mixing that will affect the combustor performance. Processes in the combustor, such as those related to the diffusivities of species and concentration-dependent rates of reaction, will be affected. Furthermore, practical systems will likely make use of liquid fuels, due to their high energy content and ease of handling. The combustion of liquid fuels can be quite complex, involving atomization, droplet dispersion, evaporation, mixing and downstream flow conditions. Each of these phenomena will be affected by the static and dynamic pressure conditions in the combustor. In order to develop a better picture of combustion of liquid fuels for underwater propulsion, and to examine downstream effects involving the interaction of the exhaust gases with the surrounding medium, investigations of scenarios in which these factors play a role must be carried out. To examine combustion issues related to underwater propulsion a simulated optically accessible experimental test section is under development at the University of

Maryland (see Figure 1). The test section consists of two chambers linked by a flow channel. The upstream chamber functions as a combustor, allowing a variety of diagnostics to be applied to flames in the combustor. The second chamber is designed to simulate a variety of surrounding conditions for underwater propulsion applications. It will contain a fluid with properties different from those of the gases exiting the combustor (e.g., density, viscosity, etc.). The interaction of the fluid in this second chamber with the exhaust gases from the first combustion chamber will cause shear layer fluid mixing between exhaust gases and the fluid in the downstream mixing chamber. This shear layer mixing can cause a subsequent effect on combustor performance which in turn will have an impact on the mixing between the two fluid streams. Thus the combustion phenomena in the combustor can be examined to simulate the underwater propulsion conditions with the experimental facility. This paper provides information on the effect of enclosure, thermal loading and fuel composition on flame structure in a liquid fuelled flames.

Design of the Optically-Accessible Combustor

The expansion ratio and length in a spray combustor must be small enough to resemble practical systems, but large enough to prevent droplet deposition on the combustor walls and possible sooting conditions. Extensive testing, involving a prototype combustor with polymer walls, indicated that a minimum expansion ratio of approximately four is required for the flames associated with this combustor. This configuration also allowed determination of the role of combustor walls as well as imperfections of the material on laser beam steering, alignment, and probe volume position issues. The completed combustion chamber is shown in Figure 2. A schematic of the chamber with relative position of the burner and exhaust gases exit is shown in Figure 3.

Experimental Conditions and Diagnostics

The burner used here features an inner and outer air annulus, surrounding a centrally located air-assisted fuel spray atomization nozzle1. The air annuli can be fitted with swirlers, allowing independent control of the swirl number of the flow through each annulus1-5. The amount of air flowing through each annulus can also be controlled independently. In the present investigations, the flame produced by the co-annular, swirl-stabilized burner was examined both under unconfined conditions and enclosed optically-accessible confined combustion conditions. Co-rotational swirlers with geometric swirl numbers of 0.385 and 0.795 (corresponding to a swirl blade vane angle of 30 and 50 degrees) were employed in the inner and outer air annuli, respectively. Four experimental cases have been examined. Kerosene flames have been examined under confined and unconfined conditions. Methanol flames have also been examined under identical conditions. The thermal load of the combustor was 16.2 kW in all cases. Due to the different heating values of kerosene and methanol, the volumetric fuel flow rate of methanol employed was 2.04 times that of kerosene. Since the specific gravities of both fuels are very similar, this means that the mass flow rate of methanol into the combustor was also double that of kerosene. However, due to the lower viscosity of methanol, it was found that no increase of atomization air was necessary to atomize the methanol fuel. Methanol fuel droplets were found to have very similar mean diameters (~60 microns under burning conditions, at elevations over 50 mm downstream of the nozzle exit) as had been previously observed in unenclosed kerosene flames.

The combustion air flow rates were also held constant in all four cases. The input fuel-air equivalence ratio for kerosene in the enclosed case was 0.4. For methanol, the confined case the equivalence ratio was 0.353. Equal air flow rates were fed though each annulus, resulting in non-swirling air flow velocities (defined as the velocity the air without any swirl to the combustion air flow) of 13.0 and 4.2m/s through the inner and outer air annulus, respectively. In the unconfined cases, the same air flow rates were fed, but due to entrainment of the surrounding air into the flame the local equivalence ratio was lower than that for the confined case.

The four different cases examined here as well as the different diagnostics used are shown in Table 1. Details on the PIV diagnostics used in spray flames, including the use of this diagnostics with high background radiation and luminous flames, is provided in ref. 6.

Results and Discussion

Global Features

In Cases 1 and 2, the general features of the methanol and kerosene flames, besides color, under unenclosed conditions were found to have very similar properties (see figure 4). Both are highly turbulent, and feature combustion stabilized by a compact recirculating region that is attached at the inner wall of the inner air annulus. For this airflow combination, PIV examination of the unenclosed airflow at the burner exit in the absence of the fuel spray and under non-burning conditions has been described previously2,3. The similar recirculation region appears to stabilize combustion in the unconfined cases is observed here for the confined cases. With both fuels, the fuel spray droplets are injected into the hot combustion products recirculating above the nozzle, and undergo evaporation in this oxygen-deficient region. Mixing across the shear layer between the recirculating regions drives the combustion, giving the flame its distinct shape. The shape is functionally identical, regardless of the fuel so long as the thermal load of the combustor is constant. The color of the flame is however different, due to the soot precursors formed by kerosene during combustion. These precursors cause very high flame luminosity when kerosene is used as the fuel. It was found that maintaining a constant mass flow rate, or a constant equivalence ratio, did not yield the same flame shape. It appears then that the heat release is the primary factor determining flame structure and dynamics. When the flame is confined (cases 3 and 4) a new feature is observed: a distinct elongation of the flame front along the new shear layer formed by the external recirculation region (see Figure 5). The central recirculation region, and the combustion occurring at its surface, is still observed, but the global features of the flame are distinctly different as compared to the unconfined flame case. In the absence of enclosure, of course, the external recirculation region is absent. The methanol and kerosene flames in the confined cases share the same structure; however, the elongated luminous brushes created by the shear region associated with the external recirculation region are far more obvious in the kerosene flame. This is due to the longer residence time necessary to oxidize soot particles from this flame; these particles travel farther along this shear layer before burning away. This results in a broader, brighter region of luminosity.

Conditions & Case No.	**Case 1**	**Case 2**	**Case 3**	**Case 4**
Fuel:	Methanol	Kerosene	Methanol	Kerosene
Enclosed:	No	No	Yes	Yes
Equivalence Ratio:	0.353	0.4	0.353	0.4
Thermal load:	16.2 kW	16.2 kW	16.2 kW	16.2 kW
Diagnostics				
Global flame photographs	Yes	Yes	Yes	Yes
PIV: 2-D Droplet Flowfield	Axial and Radial Velocity	Axial and Radial Velocity	Axial and Radial Velocity	Axial and Radial Velocity
Sound Spectra Frequeny	10-21000 Hz	10-21000 Hz	10-21000 Hz	10-21000 Hz

Table 1. Experimental conditions and corresponding diagnostics.

During experiments the kerosene flame was observed to deposit some soot on the inside of the transparent walls, but this process was slow enough to allow PIV measurements to be carried out.

The observation that the different fuels produce similar flames when the thermal loading is the same is quite important. The implication appears to be that, if the air flowfield is identical, and the amount of heat released by the fuel is comparable, the flame structure and dynamics will also be quite similar, despite the slightly different equivalence ratios, atomization properties, and flame chemistry. This could be very useful, as it is sometimes simply impractical to work with a particular liquid fuel. It also establishes continuity with other research done on enclosed methanol spray flames7. If the flow and flame dynamics are the same, studies carried out with a surrogate fuel will have considerable applicability to the fuel of interest (JP10, for example) in Navy propulsion systems. Since a range of high energy density fuels are likely to be explored in underwater propulsion, the general applicability of any result obtained will be of particular importance. It was found that maintaining a constant fuel mass flow rate, or a constant equivalence ratio, did not yield the same flame structure. The indication, then, is that the heat release is of greater importance than the fuel type for determining flame structure and dynamics in this type of spray flame, regardless of whether there is an enclosure present.

2-D PIV Results

The flowfield data from unconfined and confined methanol and kerosene fuelled flames was obtained using 2-D PIV diagnostics6. Since the fuel types employed were chemically quite different, it is useful to ask whether the resulting flow fields from the two different fuel sprays differed significantly. Contour maps showing the axial velocity profiles of the fuel spray, from 0.1D to 1.06D downstream of the combustor, are shown in figures 6 and 7. Increments in the plots are given in millimeters. The magnitude of the velocities indicated by the contour colors is in m/s. No seed particles were present in the airflow during these experiments; the plots are based only on the motion of the fuel spray. Figure 6 show a comparison of the axial velocity contours of the unenclosed flames (Cases 1 and 2). Figure 7 show a comparison of the axial velocity contours in the enclosed cases (Cases 3 and 4).

The contours for the two fuels shown in Figure 6 are very similar. In both cases, the regions of maximum droplet velocity are near the origin, and extend ~30 mm downstream of the nozzle exit. In both cases, the effect of the recirculation region is seen in the reduction in droplet velocities at radial distances between 10 and 20 mm from the centerline. Further from the centerline, droplet axial velocities are higher; this is reasonable, since droplets in this region have penetrated the flame front, and are being accelerated in the axial direction by the flow. Negative droplet velocities are not observed in this flowfield, but this is to be expected. Results from the PIV technique will be influenced by the motion of the largest, brightest droplets, as these are most likely to be detected by the camera. Larger droplets are not likely to recirculate, since the motion of the vapor phase affects them only weakly. The flow field is therefore biased towards the velocity of larger size droplets. Smaller size droplets and particles are largely lost in the measurement noise, though they do contribute to the flowfield to some extent. In the case of the unconfined methanol spray flame, the flame front was found to be located 20 mm from the centerline at an elevation of 55mm above the burner. In Figure 6, this is the region where one encounters increasingly large droplet axial velocities as one moves radially outwards from the burner centerline. In other words, the shear layer at the boundary of the recirculation region, which stabilizes the flame front, is clearly observed from the axial velocity plots shown in Figure 6.

The axial velocity contours shown in Figure 7 are also quite similar for the two fuels. Clearly, the flames produced by the two fuels share the same recirculation region characteristics. The droplet flowfield for the methanol is somewhat longer, showing higher axial velocities at elevations above 50mm than kerosene. This may be due to differences in atomization properties of the two fuels; since twice as much methanol is being atomized by the same amount of atomization air, the radial dispersion of this spray may be different. This may cause more large droplets to be accelerated downstream penetrating through the recirculation region and the flame front.

Noise Emission Spectra

Amplitude-frequency sound spectra for each case are presented in the 10-332Hz range, although the data was obtained over much higher frequencies. The results show the sound pressure level (SPL) in decibels at each frequency. In order to obtain these spectra, a receiver microphone, connected to a fast-Fourier transform analyzer, was positioned at a fixed distance from the burner centerline. This distance was not changed when the enclosure was installed. The resulting spectra are shown in Figure 8. Note that the enclosure condition completely determines the shape of the spectra. In the unconfined cases, both the methanol and kerosene flames display peak sound pressure levels in the 10 – 15 Hz range. In the confined cases, both flames displayed their peak amplitudes near 150 Hz. At every frequency, the sound amplitude displayed by the methanol flame is several dB smaller. This is due to the differences in premixed flame speeds and combustion volumetric expansion ratios of the two fuels. Clearly, the flame dynamics for both flames at the low-frequency end of the spectrum are governed by the same mechanism. This further indicates that, for this type of flame, equivalence in flowfield structure and thermal loading determines flame features, and is less dependent on the fuel type.

Summary

The design and fabrication of the combustion chamber with special reference to the non-intrusive acquisition of data has been carried out. Four different flames using two different fuels have been examined that characterize the role of confinement on the spray flame characteristics in terms of global flames features, droplet size and velocity, and sound spectra. The design of the combustor allows optical diagnostics to be employed in the study of swirl-stabilized flames. The global flame features produced by the single-component methanol fuel were found to be comparable with those observed in the multi-component kerosene fuel flame. Recirculation flow pattern and global features of the flow fields for the fuel sprays obtained using 2-D PIV were nearly the same for the both fuels under the conditions examined. However, under equal fuel mass flow conditions they were found to be significantly different. The shape and effect of the shear regions formed by the recirculation zones in both flames were nearly the same at equal thermal loading of the combustor. Dynamic effects, as measured via sound pressure spectra, showed similar dominant frequencies for both the fuels under confined and unconfined flame conditions when the same thermal load was used for both flames. This investigation lays the groundwork for future studies, to be carried out to simulate underwater propulsion conditions. The second downstream chamber has been designed and is currently being fabricated. This will then allow us to examine the shear layer mixing studies between exhaust plumes from the combustion chamber into a surrounding fluid of different properties under a variety of conditions at the combustor exit.

Acknowledgments

The support of this research by ONR, program manager Dr. Gabriel D. Roy, is gratefully acknowledged.

References

1. Habibzadeh, B., Mehresh, P. and Gupta A. K.: Control of Spray Flame Characteristics Using High Shear in a Double Concentric Swirl Burner, ASME International Joint Power Generation Conference (IJPGC), Phoenix, AZ, June 24-26, 2002.

2. Linck, M. and Gupta, A. K.: Effect of Swirl and Combustion on Flow Dynamics in Luminous Kerosene Spray Flames, 41st AIAA Aerospace Sciences Meeting, Reno, NV, January 6-9, 2003, Paper No. AIAA-2003-1345.
3. Linck, M., Armani M. and Gupta, A. K.: Passive Control of Unstable Combustion in a Swirl Stabilized Combustor, 42nd AIAA Aerospace Sciences Meeting, Reno, NV, January 5-8, 2004, Paper No. 2004-0810.
4. Habibzadeh, B and Gupta, A. K.: Passive Control of Kerosene Spray Flame Structure in a Swirl Burner, Proc. Intl. Conference on Advanced Energy Conference and Related Technologies, RAN 2001, Nagoya, Japan, December 15-17, 2001.
5. Gupta, A. K. and Linck, M: Passive Control of Flow and Flame Structure in Spray Combustion, Intl. Colloquium on Combustion Control, Cranfield University, Cranfield, UK, August 12-14, 2003.
6. Gupta, A. K., Lourenco, L., Linck, M., and Archer, S.: A New Method to Measure Flowfield in Luminous Spray Flames, J. Propulsion and Power, Vol. 20, No. 2, March/April 2004, pp. 1217-1220.
7. Li, J., and Acharya, S.: Velocity Measurements in a Combustor Undergoing Limit-Cycle Pressure Oscillations, Combustion Science and Technology, Vol. 162, No. 1-6, 2001, pp. 147-173.

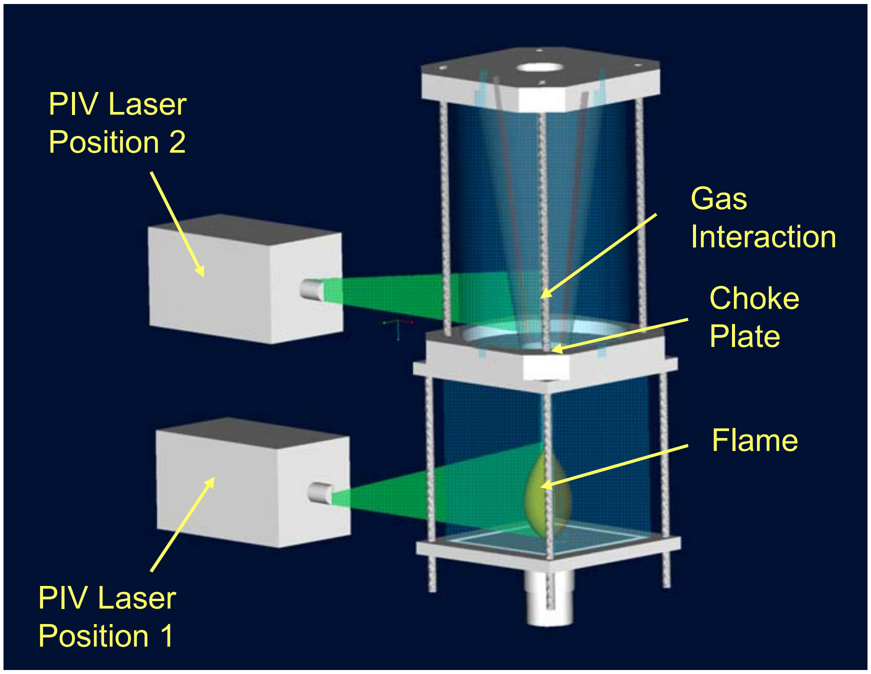

Figure 1. An overall view of the experimental facility for simulation of underwater propulsion.

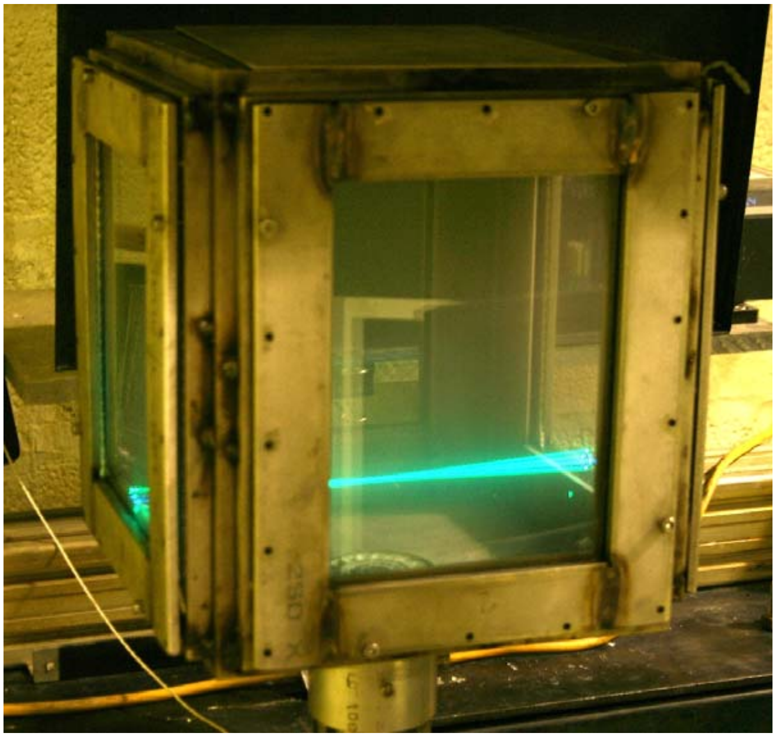
Figure 2. Completed optically-accessible combustor in the first stage with four laser beam intersecting in the control volume.

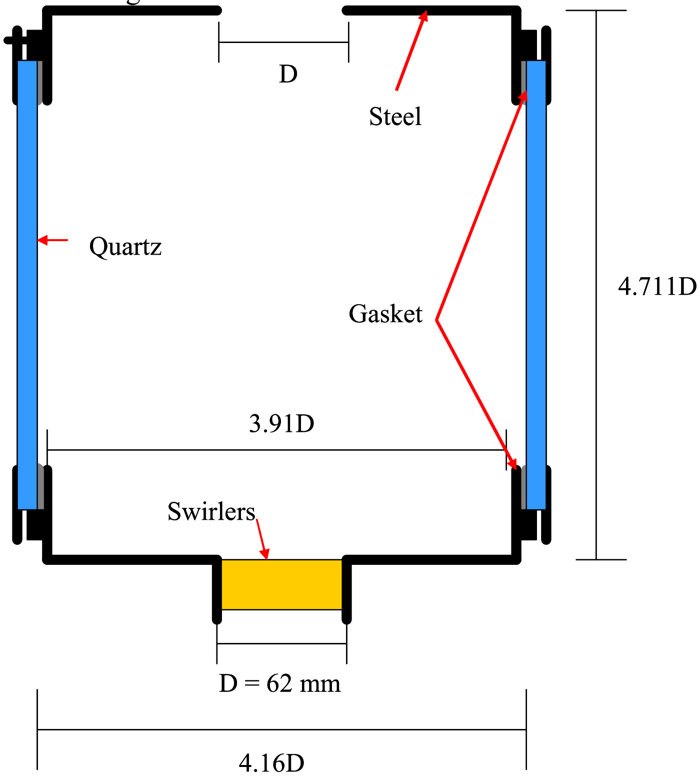

Figure 3. A schematic of the first stage combustion chamber.

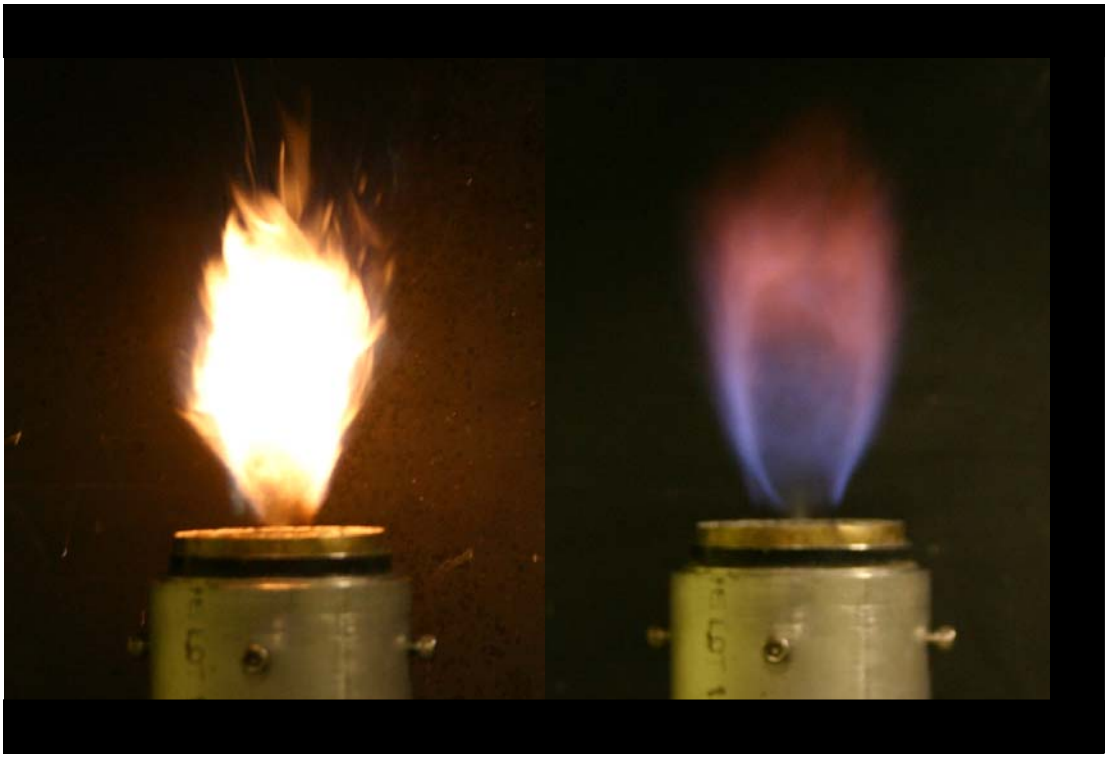

Figure 4. Unconfined kerosene flame (left) and methanol flame (right), at equal thermal loads.

Figure 5. Confined flames using kerosene (left) and methanol (right) fuel.

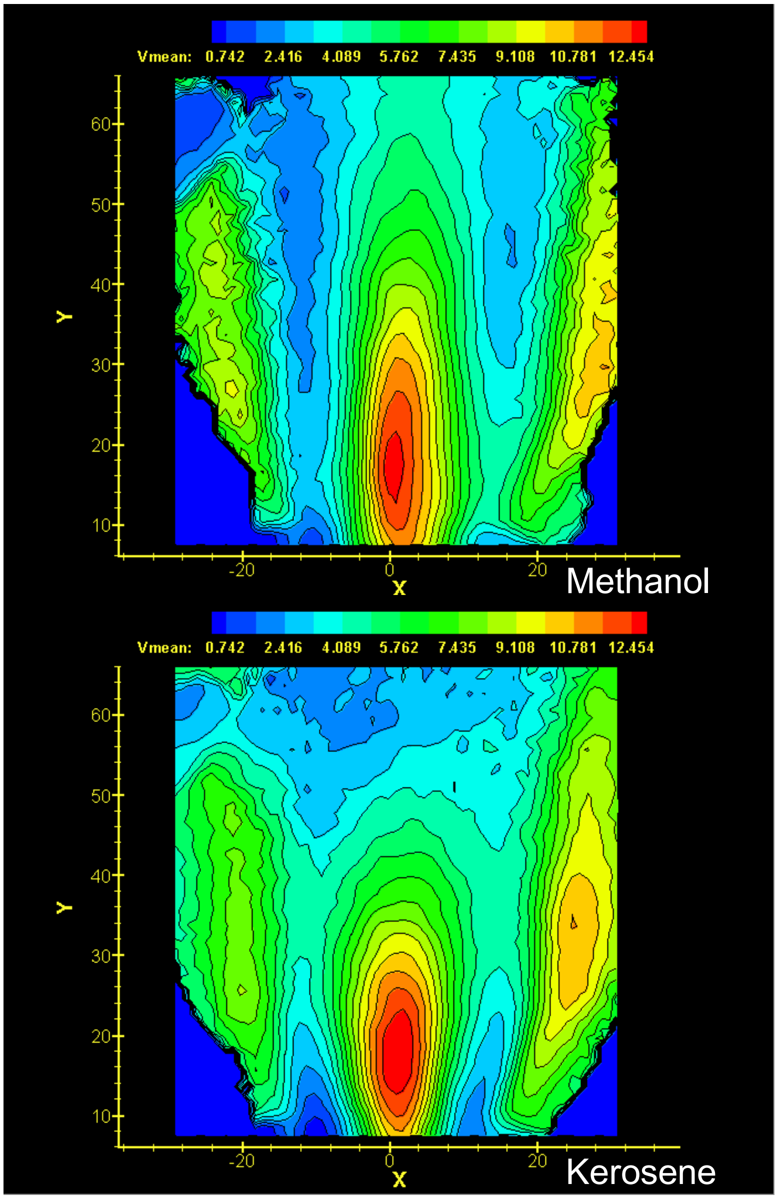

Figure 6. Axial velocity contours from 2-D PIV measurements of unenclosed fuel spray flowfields using methanol (upper), and kerosene (lower) fuel.

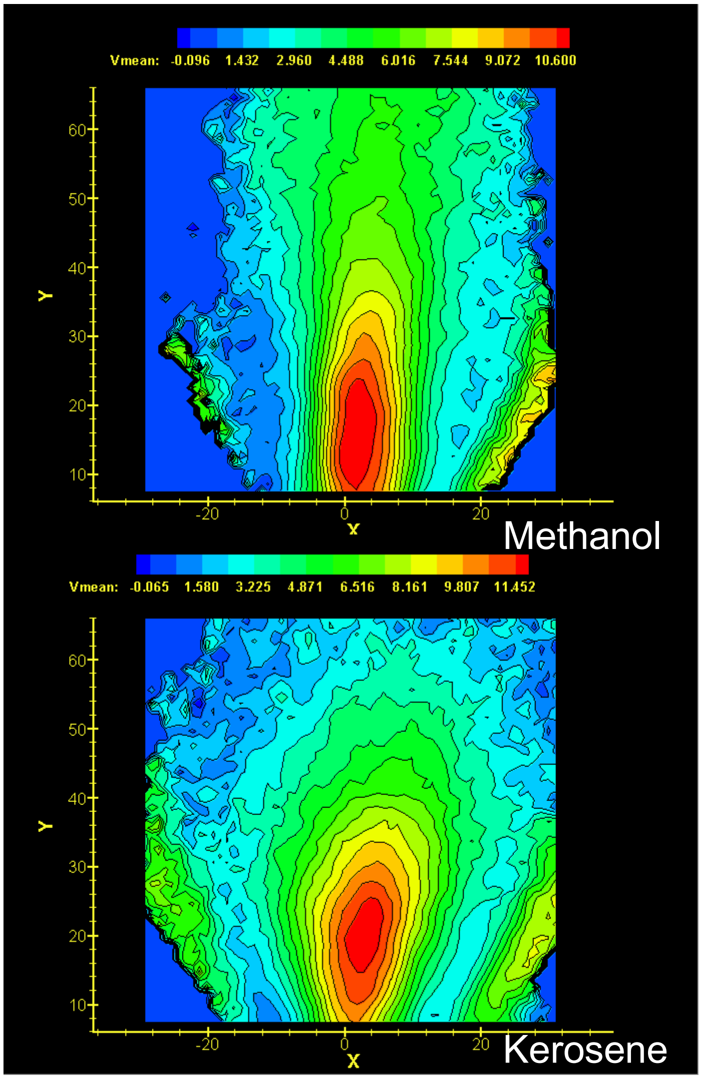

Figure 7. Axial Velocity contours from 2-D PIV measurements of enclosed fuel spray flowfields obtained inside optically accessible combustor. Upper diagram: methanol, lower diagram: kerosene.

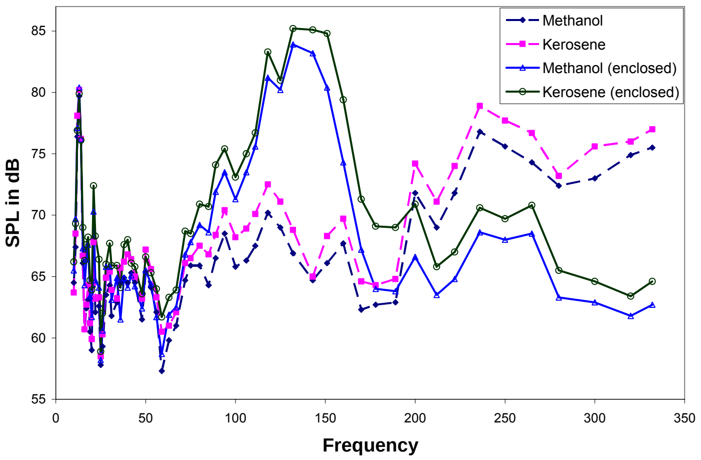

Figure 8. Frequency sound spectra in 10 to 332 Hz range.

Appendix C: Plots of Normalized Mean Velocities

This appendix presents curves of mean axial and tangential velocities, associated with the swirling flow emerging from swirlers used in the investigations described in the main text. These plots are presented in order to illustrate the point that the shapes of the curves are relatively consistent at two different swirler-inlet Reynolds numbers. In each plot, the local mean velocity components have been non-dimensionalized by the average swirler inlet velocity of the flow. The slight differences in the shapes of some of the curves created by increased flowrates account for the increase in swirl number observed at increased Reynolds number. This effect is most pronounced for the swirlers with the steepest swirl angles, and is due to changes in the thickness of boundary layers within the swirlers as the Reynolds number is increased.

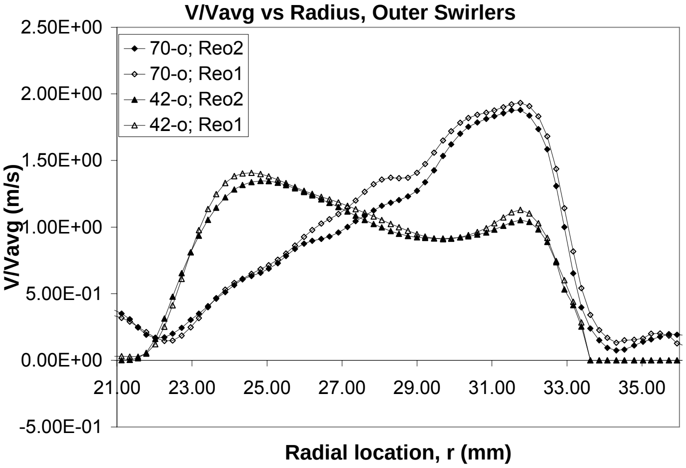

Figure C.1. Scaled curves of outer swirler mean axial velocity, normalized by the swirler inlet average velocity

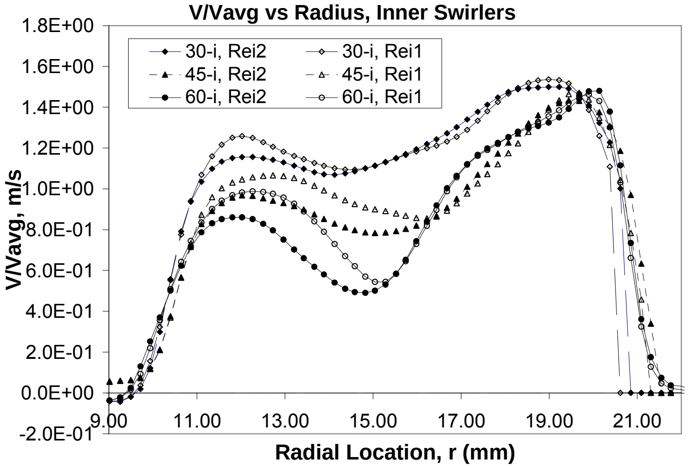

Figure C.2. Scaled curves of outer swirler mean tangential velocity, normalized by the swirler inlet average velocity

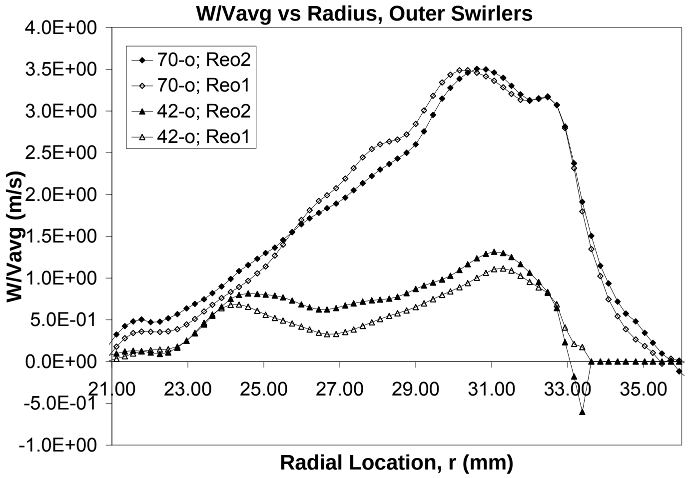

Figure C.3. Scaled curves of inner swirler mean axial velocity, normalized by the swirler inlet average velocity

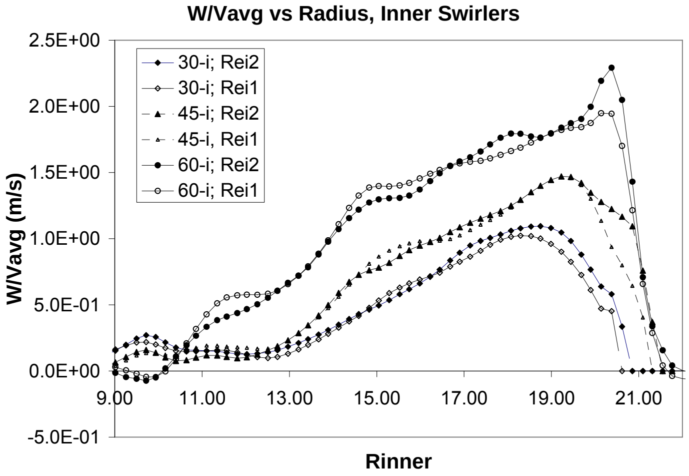

Figure C.4. Scaled curves of inner swirler mean tangential velocity, normalized by the swirler inlet average velocity

Appendix D: Calculation of Effect of Turbulence-Related Terms on Swirl Number

The effect of the inclusion of turbulence-related terms, namely the average value of v’w’ and v’v’, in the swirl number calculations, will be addressed here. A study was conducted in a representative flow, to evaluate the effect of the inclusion of these terms on the resulting swirl number. It will be shown that the omission of these terms has no significant effect on the overall swirl number obtained, and that differences in swirl number, observed as a result of changes in Reynolds number, are due to small changes in the mean velocity contours in the flow. These small changes are due to alterations in the thickness of the boundary layers within the swirler, as described in the main text and in Appendix C.

Flows at two Reynolds number conditions, (see Reynolds Condition 1 and Reynolds Condition 2, described in the main text of this work) emerging from the 60-i swirler, were examined. The mean and varying components of axial and tangential velocity were examined at two locations in each flow, at each Reynolds number.

At each location, and for each Reynolds number, 26 data sets were investigated. Thus, 104 data sets were evaluated, in order to provide statistically-significant information on the proportional relationship between the terms VW, V^2, v’w’, and v’v’, which occur in Equations (3) and (4) in the main text of this work.

Table D.1 presents evidence that the inclusion of the turbulence-related terms (the averages of v’w’ and v’v’, denoted as <v’w’> and <v’v’>) is not likely to have a significant effect on the calculated swirl number, and that the approximate expression, given by Equation (5) in the main text of this work, provides a good approximation of the swirl number. Under both Reynolds number conditions, the inclusion of the terms based on the fluctuating velocities, v’ and w’, adds only a few percent to the total values accounted for by the terms related to the mean velocities, V and W. Moreover, it can be seen from Equation (2) in the main text that the contributions of the turbulent terms will cancel to some degree, since the term <v’w’> adds to the numerator of the expression in Equation (2), and the term <v’v’> adds to the denominator. Thus, the overall effect of the inclusion of these terms in the swirl number calculation is found to be very slight; on the

Reynolds Condition 1								
	x(mm)	y(mm)	VW	V^2	<v'w'>	<v'v'>	<v'w'>/(VW)	<v'v'>/(VV)
Location 1	17.0	3.0	-33.566	24.082	-0.055	0.704	0.002	0.029
Location 2	21.0	6.0	-30.258	24.012	-0.502	1.002	0.017	0.042
Reynolds Condition 2								
	x(mm)	y(mm)	VW	V^2	<v'w'>	<v'v'>	<v'w'>/(VW)	<v'v'>/(VV)
Location 1	17.0	3.0	-111.231	74.521	-1.899	3.001	0.017	0.040
Location 2	21.0	6.0	-96.185	74.758	-2.854	4.223	0.030	0.056

Table D.1. Terms based on mean and fluctuating axial and tangential velocities at two locations

order of one to two percent. The locations chosen for the comparisons are sufficiently different to indicate that this observation will likely hold throughout the flow. Since including the turbulence-related terms complicates the swirl number calculation considerably, it is reasonable to omit them. This also ensures that swirl numbers calculated in a given study can be compared directly with those calculated by other investigators, since swirl numbers calculated by other researchers also generally do not include contributions form turbulence-related terms.

References

Aerometrics, Inc., "Real-Time Signal Analyzer, University of Maryland Systems Manual," 1995.

Alkislar, M. B., Krothapalli, A., and Lourenco, L. M., "Structure of a Screeching Rectangular Jet: A Stereoscopic PIV Study", J. Fluid Mechanics, 489, 2003, 121-154.

Anderson, J. D., "Modern Compressible Flow, 3rd Edition," McGraw Hill, Boston, MA, USA, 2003.

Bachalo, W. D., and Houser, M. J., "Phase/Doppler Spray Analyzer for Simultaneous Measurements of Drop Size and Velocity Distributions," Optical Engineering, Vol. 23, no. 5, 1984, pp. 583-590.

Bernard, P., and Wallace, J.M., "Turbulent flow: Analysis, Measurement, and Prediction," Wiley and Sons, Hoboken, NJ, USA, 2002.

Brouillette, M., "The Richtmyer-Meshkov Instability," Ann. Review of Fluid Mechanics, Vol 34, 2002, pp. 445-68.

Chigier, N. A., and Beér, J. M., J. of Basic Engineering, vol. 86, No. 4, p. 788, 1964.

Cohen, H., Rogers, C.F.C., Saravanamuttoo, H.I.H, "Gas Turbine Theory, 4th edition," Longman, Burnt Mill, Harlow, Essex, UK, 1996.

Conrad, T. J., Bibik, A., Lee, J.Y., Shcherbik, D., Lubarsky, E., and Zinn, B. T., Control of Combustion Instabilities by Fuel Spray Modification Using Smart Fuel Injector, Proceedings of the 39th AIAA/ASME/SAE/ASEE Joint Propulsion Conference and Exhibit, Huntsville, AL, July 2003, Paper AIAA 2003-4937.

Davis, N. T., and Samuelsen, G. S., "Optimization of Gas Turbine Combustor Performance Throughout the Duty Cycle," Proc. of 26th Symposium (International) on Combustion, The Combustion Institute, pp. 2819-2825, 1996.

Delavan Spray Technologies, "Delavan Spray Technologies: Industrial Spray Nozzles and Accessories," Coltec Industries, Monroe, North Carolina, USA, 1998.

Drake, R. P., "Hydrodynamic Instabilities in Astrophysics and in Laboratory High-Energy-Density Systems," Plasma Physics and Controlled Fusion, Vol. 47, 2005, pp. B419-B440.

Fleming, J. W., Sheinson, R. S., and Maranghides, A., "Water Mist Monitoring in Large-Scale Suppression Research: Fundamental Issues," Proc. of Halon Options Technical Working Conference, April 24-26, Albaquerque, NM, USA, 2001.

Gao, Z., Linck, M., Mashayek, F., and Gupta, A. K., "Experimental Results and Calculations of Two-Phase Flow in a Swirl Burner Under Isothermal Condition," 41st AIAA Aerospace Sciences Meeting, Reno, NV, January 6-9, 2003, Paper No. AIAA-2003-0336.

Gaydon, A.G., and Wolfhard, H. G., Flames, Their Structure, Radiation, and Temperature, Wiley, New York, 1979.

Gupta, A. K., Lilley, D. G., Syred, N., "Swirl Flows," Abacus Press, Tunbridge Wells, Kent, UK, 1984.

Gupta, A. K. and Linck, M., "Passive Control of Flow and Flame Structure in Spray Combustion," Intl. Colloquium on Combustion Control, Cranfield University, Cranfield, UK, August 12-14, 2003.

Gupta, A. K., Lourenco, L., Linck, M., and Archer, S., "A New Method to Measure Flowfield in Luminous Spray Flames," J. Propulsion and Power, Vol. 20, No. 2, March/April 2004, pp. 369-372.

Gupta, A. K., Habibzadeh, B., Archer, S., and Linck, M., "Control of Flame Structure in Spray Combustion," Combustion Processes in Propulsion, Roy, G. D. ed., Elsevier Butterworth Heineman, Burlington, MA, USA, pp 129-137, 2006.

Gutmark, E.J., Grinstein, F.F., "Flow Control With Noncircular Jets", Annual Review of Fluid Mechanics, Vol. 31, 1999, pp. 239-272.

Hu, H., Saga, T., Kobayashi, T., Taniguchi, N., Passive Control on Jet Mixing Flows by using Vortex Generators, 6th Triennial Symposium on Fluid Control, Sherbrooke, Canada, August 2000.

Kane, J., Drake, R. P., and Remington, B. A., "An Evaluation of the Richtmyer-Meshkov Instability in Supernova Remnant Formation," Astrophysics Journal, Vol. 511, No. 1, 1999, pp. 335-340.

Lefebvre, A. H., "Gas Turbine Combustion," Taylor and Francis, Philadelphia, PA, 1983.

Li, J., and Acharya, S., Velocity Measurements in a Combustor Undergoing Limit-Cycle Pressure Oscillations, Combustion Science and Technology, v 162, n 1-6, 2001, p 147-173.

Linck, M. and Gupta, A. K., “Effect of Swirl and Combustion on Flow Dynamics in Luminous Kerosene Spray Flames,” 41st AIAA Aerospace Sciences Meeting, Reno, NV, January 6-9, 2003, Paper No. AIAA-2003-1345.

Linck, M., Armani, M., and Gupta, A. K., “Flow Characteristic Effects on Exhaust Gas Composition in Kerosene Spray Flames,” IECEC Conference, Portsmouth, VA, August, 17-21, 2003, Paper No. AIAA-2003-5929.

Linck, M., Armani, M., and Gupta, A. K., “Passive Control of Unstable Combustion in a Swirl Stabilized Combustor,” 42nd AIAA Aerospace Sciences Meeting, Reno, NV, January 5-8, 2004, Paper No. AIAA-2004-0810.

Linck, M., Armani, M., and Gupta, A. K., “Effect of Swirl and Fuel Pulsation on Flame Dynamics, Flame Structure, and Droplet Dynamics in Swirl Stabilized Spray Flames,” ASME Power Conference, Baltimore, MD, March 30-April 1, 2004, Paper No. PWR 2004-52048.

Linck, M., Yu, K. H., Gupta, A. K., “Dynamics of Unconfined and Confined Methanol and Kerosene Spray Flames,” Proc. IECEC Conference, Providence, RI, August 16-19, 2004, Paper No. AIAA-2004-5503.

Linck, M., and Gupta, A. K., “Effect of Combustion on Exhaust Jet Characteristics in a Pressurized, Swirl-Stabilized Spray Combustor,” 43rd AIAA Aerospace Sciences Meeting, Reno, NV, January 10-13, 2005, Paper No. AIAA-2005-0956.

Linck, M., Gupta, A. K., Bourhis, G., and Yu, K., “Combustion Characteristics of Pressurized Swirling Spray Flame and Unsteady Two-Phase Exhaust Jet,” 44th AIAA Aerospace Sciences Meeting, Reno, NV, January 9-12, 2006, Paper No. AIAA-2006-0377.

Linck, M., Gupta, A. K., “Control of Forced Combustion Instability in a Swirl-Stabilized Spray Combustor via Swirl and Airflow Distribution,” Accepted for Publication, J. Propulsion and Power, 2006.

Locke, R. J., Hicks, Y. R., de Groot, W. A., “Non-Intrusive, Laser-Based Imaging of Jet-A Fuel Injection and Combustion Species in High Pressure, Subsonic Flows,” NASA Technical Memorandum, TM -211113, 2001.

Menon, S., Stone, C., Patel, N., “Multi-Scale Modeling for LES of Engineering Designs of Large-Scale Combustors,” Proc. of 42nd AIAA Aerospace Sciences Meeting, Reno, NV, January 5-8, 2004, Paper No. AIAA-2004-0157.

Mörtberg, M., “Study of gas fuel jet burning in low oxygen content and high temperature oxidizer,” Doctoral Thesis in Energy and Furnace Technology, Kungliga Tekniska Högskolan, Stockholm, Sweden, 2005.

Nasr, G.G., Yule, A.J., and Bendig, L., Industrial Sprays and Atomization: Design, Analysis and Applications, London, Springer, 2002.

Prahl, S., "Mie Scattering calculations," Website of the Oregon Medical Laser Center, http://omlc.ogi.edu/calc/mie_calc.html, 2001, Accessed Feb. 2006.

Presser, C., Gupta, A. K., Avedisian, C. T., and Semerjian, H.G., Effect of Dodecanol Content on the Combustion of Spray Flames, Atomization and Sprays, Vol. 4, No. 3, 1994, pp. 207-222.

Raffel, M., Willert., C., Kompenhans, J., "Particle Image Velocimetry: A Practical Guide," Springer-Verlag, Berlin, 1998.

Rayleigh, J.W.S., The Theory of Sound, Vol. 2, Dover Publications, New York, NY, 1945, pp. 170-235.

Schadow, K.C., and Gutmark, E., Combustion Instability Related to Vortex Shedding in Dump Combustors and their Passive Control, Progress in Energy and Combustion Science, Vol. 18, No. 2, 1992, pp. 117-131.

Sengupta, K., and Mashayek, F., "Numerical Study of Pulsed Injection for Control of Combustion," Proc. of 43rd AIAA Aerospace Sciences Meeting, Reno, NV, January 10-13, 2005, Paper No. AIAA-2005-0954.

Sivasegaram, S., and Whitelaw, J.H., Suppression of Oscillations in Confined Disk-Stabilized Flames, Journal of Propulsion, Vol. 3, No. 4, 1987, pp. 291-295.

Vincont, J.-Y., Simoens, S., Ayrault, M., and Wallace, J. M., "Passive scalar dispersion in a turbulent boundary layer from a line source at the wall and downstream of and obstacle," J. Fluid Mech, No. 424, 2000, pp. 127-167.

Wallace, J. M., Personal Communication, 2005.

Widmann, J. F., and Presser, C., "A Benchmark Experimental Database for Multiphase Combustion Model Input and Validation," Combustion and Flame, vol. 129, pp. 47–86, 2002.